UNIVERSITY OF SOUTHAMPTON

Signals for Supersymmetry in Photon Photon Scattering

by

Luke Weston

A thesis submitted for the degree of
Doctor of Philosophy

Department of Physics

February, 2001

UNIVERSITY OF SOUTHAMPTON

ABSTRACT

FACULTY OF SCIENCE
PHYSICS

Doctor of Philosophy

Signals for Supersymmetry in Photon Photon Scattering

by Luke Weston

We introduce the theoretical framework for analysing photon photon scattering due to electron positron collisions. The structure function F_2^γ is introduced along with its corresponding evolution using the DGLAP equations. The possible supersymmetric contributions to this evolution are introduced with relevance to the next generation of high energy linear colliders.

We numerically evolve virtual photon parton densities up to the SUSY threshold and higher using coupled inhomogeneous DGLAP differential equations. An effort is made to include the squark threshold effect in such a way that both the renormalization group equations are satisfied and the perturbative calculation is reproduced. The difference to F_2^γ due to SUSY dependent splitting functions is examined. Virtual SUSY corrections to this evolution procedure are then examined below and above the squark threshold.

Finally a calculation of the amount events we might expect for chargino production is carried out. The feasibility of this process as a signal for SUSY can then be assessed.

Contents

List of Figures

Preface

Chapter 1 does not contain original work and was put together using the sources referenced in that Chapter. Chapter 2 is merely an extension of the ideas in Chapter 1 and again no claim is made to originality. Chapters 3, 4 and 5 contain original work. Much of the work contained in Chapter 3 is currently published in *Eur. Phys. J.* [25].

Acknowledgements

Predominantly I must thank Douglas for guiding me during my time at Southampton. He was at all times patient and did his best to explain things simply to me. It was an honour and a privilege to be able to work closely with someone who is both so very gifted and so very colourful in character.

My family and friends have been very patient and supportive as I have swung between the usual highs and lows that accompany three years of study. A special note of thanks goes to my friend Michael without whom I could never have finished.

Southampton has a fantastic group of postgraduate students, postdocs and full time staff. In my experience nobody was ever too busy to refuse to help in whatever way they could. It is also a very social group which creates a friendly and relaxed atmosphere in which to work. I have made two very good friends, John and Alex, who often put up with my rantings in the pub when I needed encouragement.

Chapter 1

General Formalism

1.1 Introduction

The photon allows the electromagnetic interaction between charged particles. In QED it can be thought of as a massless and structureless particle. However during high energy processes it may fluctuate into charged fermion anti-fermion pairs. If during this time one of the fermions interacts via another gauge boson then the 'structure' of the photon can be said to have been revealed. This 'resolved' photon can be thought of as consisting of quarks, gluons, squarks or whatever our field theory model allows.

The main thrust of this discussion is to view the possible effects of incorporating supersymmetry (SUSY) into the theoretical framework of photon structure. We do this by looking at cross sections but mainly by discussing the structure functions of the photon. Structure functions are parameterizations of the cross section and give us a simple and consistent way of describing photon structure.

In Chapter 1 we develop the necessary theoretical framework with which to understand how what we are calculating is connected to what we can measure in an accelerator. This part of the thesis is in no way original work and reference has been made to the following sources [4], [5], [6], [7], [8] and [12]. Chapter 2 explains the possible need for the introduction of SUSY and in what way we propose to introduce it in the framework of photon structure. Chapter 3 discusses the DGLAP evolution of the photon structure function F_2^γ through the SUSY threshold and any changes to this evolution due to the possible presence of SUSY particles. Chapter 4 deals with supersymmetric virtual corrections to this evolution. Chapter 5 gives predictions for the measurement of chargino production from electron positron collisions. We finish up with a brief summary in Chapter 6. A brief discussion of the C++ implementation used for modelling the DGLAP evolution equations along with some more mathematical considerations have been relegated to Appendices.

1.2 Preliminaries

Experimental data on photon structure is mainly obtained from the LEP electron positron collider, the HERA electron proton collider and the SLD detector at the SLC collider. We are going to concentrate specifically on the electron positron collision process as a means of probing the structure of the photon.

An electron[1] can undergo deep inelastic scattering via the emission of a highly virtual photon, γ_q^*. This virtual photon acts as a probe of the other electron. This is why the process is often referred to as photon electron scattering. It is important to note that a Z^0 can be emitted instead of a photon and act as the probe. This introduces an extra contribution to the process that we neglect in this discussion. We will only be concerned with contributions due to a virtual photon probe. To leading order in QED the target electron emits a virtual photon, γ_p^*. This collision process is shown in Figure 1.1.

Thus the experimental process that gives rise to photon structure is

$$ee \to ee\gamma^*\gamma^* \to eeX$$

where X is some final state eg. $q\bar{q}$ pair.

Note that there are two other types of process that can contribute to the total cross section. These are the s-channel and t-channel bremsstrahlung processes. Figure 1.2 shows an example of these processes where the final state X is for example two quarks, $ee \to eeq\bar{q}$. These processes contribute much less than the process in Figure 1.1 [3]. In the following discussion we

---

[1] For simplicity we do not distinguish between the electron and the positron. The contribution is equivalent.

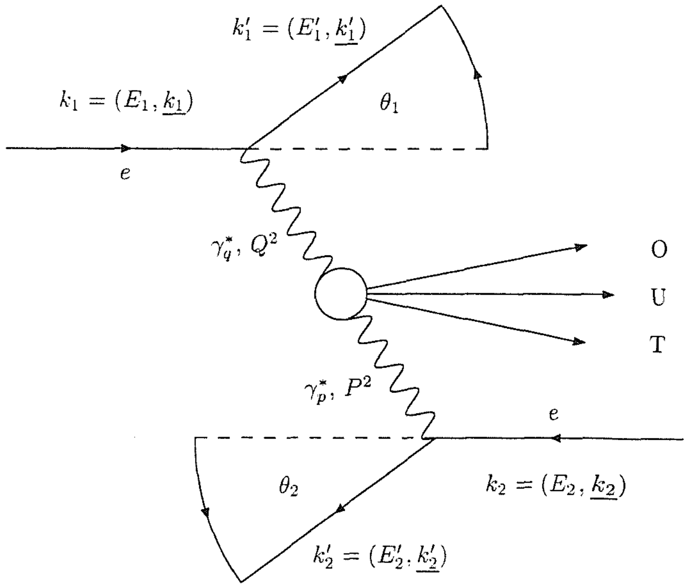

Figure 1.1: Experimental setup for virtual photon photon scattering.

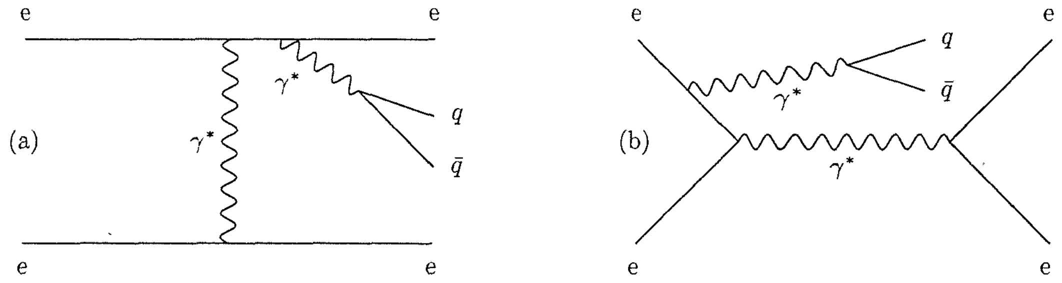

Figure 1.2: Examples of additional contributions to the total cross section. (a) t-channel bremsstrahlung and (b) s-channel bremsstrahlung.

will only be concerned with the contribution of Figure 1.1 to the structure functions and cross section.

With reference to Figure 1.1, we will use the following variables in our analysis,

The probe virtual photon momentum,

$$q = k_1' - k_1 \tag{1.1}$$

and its virtuality which is negative,

$$\begin{aligned} Q^2 &= -q^2 \\ &= 2E_1E_1'(1-\cos\theta_1) \end{aligned} \tag{1.2}$$

Similarly for the target photon,

$$p = k_2' - k_2 \tag{1.3}$$

$$P^2 = -p^2 \tag{1.4}$$

Bjorken x is given in terms of the two photon momenta q and p,

$$x = \frac{Q^2}{2p\cdot q} \tag{1.5}$$

We have an internal invariant mass squared

$$S = (q+p)^2 \tag{1.6}$$

and a total invariant mass squared

$$S_{tot} = (k_1+k_2)^2$$

For deep inelastic scattering $Q^2 \gg P^2 \approx 0$. However we derive some results for the region $P^2 \neq 0$, so we define

$$r = P^2/Q^2 \tag{1.7}$$

At this point we need to know what is in principle perturbatively calculable. This involves a discussion of point-like and hadron-like processes. The literature often refers to point-like as 'direct' and hadron-like as 'resolved'.

Referring to Figure 1.3, we can organize the contributions to the cross section into the perturbatively calculable point-like diagrams and the non-perturbative hadron-like processes. (a) shows the tree-level point-like process $ee \to eeq\bar{q}$. This is the most dominant contribution in deep inelastic photon photon scattering. (b) and (c) are examples of higher order point-like contributions which are in principle calculable using perturbative QCD. It is these point-like contributions that are absent in the equivalent analysis of nucleon structure. This fundamental difference stems from the point-like coupling of the photon to quarks. Obviously there is no such point-like coupling between say a proton and a quark. (d) shows how a photon can fluctuate into a hadronic state with the same quantum numbers as the photon. This type of contribution is termed hadron-like and cannot be directly calculated using perturbative QCD. The ability to formally separate these two types of contribution depends on P^2, the virtuality of the target photon. As $P^2 \to 0$, one can factorize out the hadronic part of the structure functions. In this limit and after factorization the structure functions of the photon can thus be divided into the perturbatively calculable point-like part and the hadron-like part. The vector meson dominance model (VMD) [9] can be successfully used

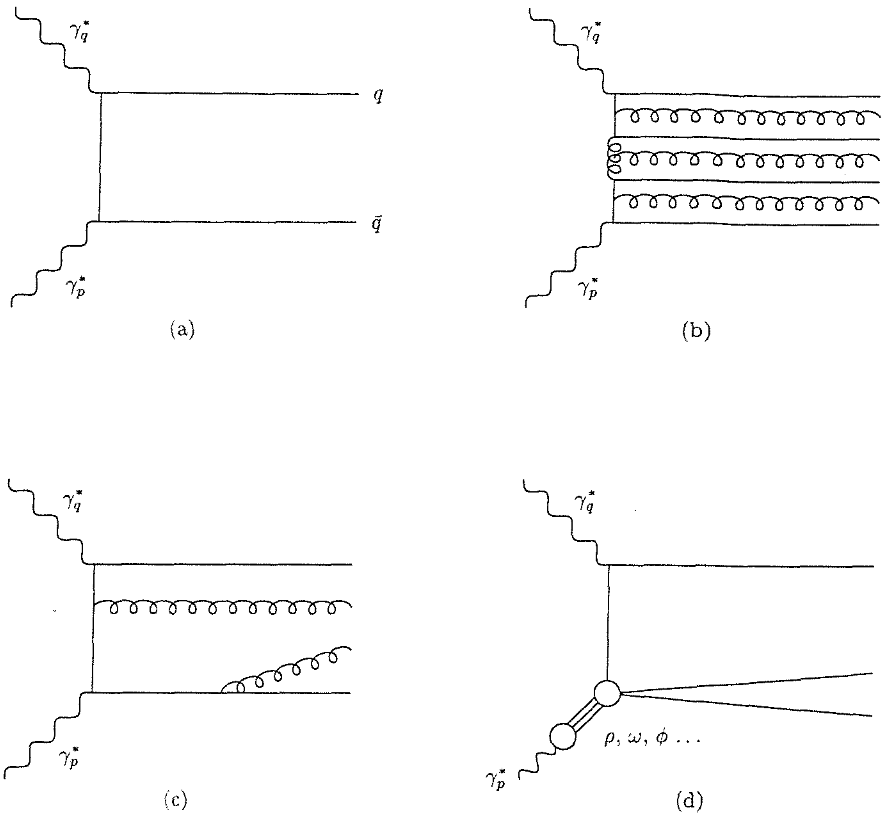

(a) (b)

(c) (d)

Figure 1.3: Examples of point-like and hadron-like contributions. (a) is the tree-level quark point-like contribution. (b) and (c) are examples of higher order point-like contributions. (d) is a hadron-like contribution.

to describe the hadron-like part of the structure function F_2^γ by considering the vector mesons ρ, ω and ϕ.

In order to forge a link with what is experimentally measured and what we discuss in the following we must show how the cross-section is related to the relevant structure functions of the photon. The differential cross section for the point-like contribution to $ee \rightarrow eeX$ is as follows [1],

$$\begin{aligned} d^6\sigma &= \frac{d^3k_1'd^3k_2'}{E_1'E_2'}\frac{\alpha^2}{16\pi^4Q^2P^2}\left[\frac{(p\cdot q)^2-Q^2P^2}{(k_1\cdot k_2)^2-m_e^2m_e^2}\right]^{1/2} \\ &\Big(4\rho_1^{++}\rho_2^{++}\sigma_{TT}+2|\rho_1^{+-}\rho_2^{+-}|\tau_{TT}\cos 2\phi+2\rho_1^{++}\rho_2^{00}\sigma_{TL} \qquad (1.8) \\ &+2\rho_1^{00}\rho_2^{++}\sigma_{LT}+\rho_1^{00}\rho_2^{00}\sigma_{LL}-8|\rho_1^{+0}\rho_2^{+0}|\tau_{TL}\cos\phi\Big) \end{aligned}$$

In the $\gamma_q^*\gamma_p^*$ centre of mass frame, ϕ is the angle subtended between the scattering planes of the electrons, the scattering plane being the plane made by the spatial vectors of an incoming and outgoing particle. It is possible to simplify this equation by removing the ϕ dependence, this being done by integrating over ϕ. σ_{TT}, σ_{TL}, σ_{LT} and σ_{LL} are total cross sections. τ_{TT} and τ_{TL} are interference terms. They correspond to helicity states of the two photons, T being transverse and L being longitudinal. The various ρ_i^{jk} are given as,

$$2\rho_1^{++} = \frac{(2k_1\cdot p-p\cdot q)^2}{(p\cdot q)^2-Q^2P^2}+1-4\frac{m_e^2}{Q^2}$$

$$2\rho_2^{++} = \frac{(2k_2\cdot p-p\cdot q)^2}{(p\cdot q)^2-Q^2P^2}+1-4\frac{m_e^2}{P^2}$$

$$\rho_1^{00} = 2\rho_1^{++}-2+4\frac{m_e^2}{Q^2}$$

$$\rho_2^{00} = 2\rho_2^{++}-2+4\frac{m_e^2}{P^2}$$

$$|\rho_i^{+-}| = \rho_i^{++} - 1$$

$$|\rho_i^{+0}| = \sqrt{(\rho_i^{00} + 1)|\rho_i^{+-}|}$$

where +, − and 0 refer to particular photon helicities.

There are three structure functions F_2^γ, F_T^γ and F_L^γ, though only two[2] of these are needed to fully parameterize the cross section. These are defined by the following relations [2].

$$\begin{aligned} 2xF_T^\gamma(x,Q^2,P^2) &= \frac{Q^2}{4\pi^2\alpha}\frac{\sqrt{(p\cdot q)^2 - Q^2P^2}}{p\cdot q} \\ &\times \left[\sigma_{TT}(x,Q^2,P^2) - \tfrac{1}{2}\sigma_{TL}(x,Q^2,P^2)\right] \end{aligned} \qquad (1.9)$$

$$\begin{aligned} F_2^\gamma(x,Q^2,P^2) &= \frac{Q^2}{4\pi^2\alpha}\frac{\sqrt{(p\cdot q)^2 - Q^2P^2}}{p\cdot q} \\ &\times \Big[\sigma_{TT}(x,Q^2,P^2) + \sigma_{LT}(x,Q^2,P^2) \\ &\quad -\tfrac{1}{2}\sigma_{LL}(x,Q^2,P^2) - \tfrac{1}{2}\sigma_{TL}(x,Q^2,P^2)\Big] \end{aligned} \qquad (1.10)$$

---

[2] As mentioned previously, the Z^0 probe contribution has been neglected. The Z^0 gives an extra structure function F_3^γ due to axial vector couplings.

$$F_L^\gamma(x,Q^2,P^2) = F_2^\gamma(x,Q^2,P^2) - 2xF_T^\gamma(x,Q^2,P^2) \tag{1.11}$$

Note that the interference terms τ_{TT} and τ_{TL} must be discarded in order to define the structure functions. The contribution due to these interference terms can be isolated experimentally and very much depends on the kinematical variables Q^2, P^2 and the invariant mass squared of what is produced, M_X^2. In some regions they produce a difference in the cross section of only a few percent while in other regions the contribution is large enough such that the use of structure functions to parameterize the cross section becomes meaningless.

We will mainly be concerned with the limit $Q^2 \gg P^2 \approx 0$. In this region the target photon is almost real and hence cannot have a longitudinal polarization. The consequences of this are that the terms σ_{TL}, σ_{LL}, and τ_{TL} vanish because of their P^2 dependence as $P^2 \to 0$. Also the coefficient of τ_{TT} vanishes. This allows a simpler expression for the cross section

$$\begin{aligned} d^6\sigma &= \frac{d^3k_1'd^3k_2'}{E_1'E_2'} \frac{\alpha^2}{16\pi^2Q^2P^2} \left[\frac{(p\cdot q)^2 - Q^2P^2}{(k_1\cdot k_2)^2 - m_e^2m_e^2}\right]^{1/2} \\ &\times \; 4\rho_1^{++}\rho_2^{++}\left[\sigma_{TT} + \frac{\rho_1^{00}}{2\rho_1^{++}}\sigma_{LT}\right] \end{aligned} \tag{1.12}$$

which can easily be seen to correspond to a probe photon of either transverse or longitudinal polarization colliding with a real target photon of transverse polarization. Obviously in an experiment the virtuality of the target photon cannot be kept exactly zero. However the contributions from the longitudinal terms and the interference terms are both of the order of a few percent and actually almost cancel each other out such that Equation (1.12) gives an accurate expression for the cross section.

In this limit the structure functions are also simplified,

$$\begin{aligned} 2xF_T^\gamma(x,Q^2) &= \frac{Q^2}{4\pi^2\alpha}\,\sigma_{TT}(x,Q^2) \\ F_2^\gamma(x,Q^2) &= \frac{Q^2}{4\pi^2\alpha}\left[\sigma_{TT}(x,Q^2)+\sigma_{LT}(x,Q^2)\right] \qquad (1.13) \\ F_L^\gamma(x,Q^2) &= \frac{Q^2}{4\pi^2\alpha}\,\sigma_{LT}(x,Q^2) \end{aligned}$$

The differential cross section can also be cast in a form where the flux of incoming target photons is explicitly seen.

Using the following variables,

$$y = \frac{p\cdot q}{k_1\cdot p}$$

$$z = \frac{E_p}{E}$$

where $p = (E_p\,,\underline{p})$ and $(E_1 = E_2 = E)$ in the centre of mass frame of the electrons in Figure 1.1. In the limit $P^2 \rightarrow 0$ the differential cross section can be written as,

$$
\begin{aligned}
\frac{d^4\sigma}{dx\,dQ^2\,dz\,dP^2} &= \frac{d^2N_\gamma^T}{dz\,dP^2}\frac{2\pi\alpha^2}{xQ^4}\left[1+(1-y)^2\right] \\
&\times \quad \left[2xF_T^\gamma(x,Q^2)+R(L/T)F_L^\gamma(x,Q^2)\right]
\end{aligned}
\tag{1.14}
$$

where $d^2N_\gamma^T/dz\,dP^2$ describes the flux of incoming transversely polarized photons and $R(L/T)$ is the ratio of the fluxes of longitudinal and transverse incoming photons, $R(L/T) = (d^2N_\gamma^L/dz\,dP^2)/(d^2N_\gamma^T/dz\,dP^2)$.

Alternatively we can express Equation (1.14) as

$$
\begin{aligned}
\frac{d^4\sigma}{dx\,dQ^2\,dz\,dP^2} &= \frac{d^2N_\gamma^T}{dz\,dP^2}\frac{2\pi\alpha^2}{xQ^4}\left[1+(1-y)^2\right] \\
&\times \quad \left[F_2^\gamma(x,Q^2)-\frac{y^2}{1+(1-y)^2}F_L^\gamma(x,Q^2)\right]
\end{aligned}
\tag{1.15}
$$

where the dependence on F_2^γ can be seen explicitly.

For the rest of the discussion we will be concerned only with the F_2^γ structure function. This is because it is easily accessible by experiment. There are large subtractive errors involved in extracting F_L^γ from experiment which renders theoretical comparison very difficult.

F_2^γ is thus a quantity that can be measured by experiment. What we mean by F_2^γ depends on whether we are tagging particular outgoing particles eg. $ee \to eeq\bar{q}$ or whether we are measuring the total cross section ie. $ee \to eeX$. What we can do is calculate certain contributions to F_2^γ. We must keep in mind though the assumptions that we have made, namely that certain formulae are only valid for $P^2 \to 0$ and that in certain kinematical regions the use of structure functions does not correspond to the cross section because the interference terms give a large contribution.

1.3 Parton Distribution Functions

After Witten [10] developed techniques using the operator product expansion in the large Q^2 limit it was hoped that the point-like part of F_2^γ could be be calculated exactly including its normalization. This could in principle lead to a direct measurement of α_s. However crucial terms have to be neglected in this approach. Also this asymptotic solution is plagued by divergences at small x that get worse at higher orders of perturbation theory. The idea of calculating F_2^γ exactly from perturbation theory thus had to be abandoned.

A less ambitious approach is to apply renormalization group methods which allows the Q^2 dependence F_2^γ to be calculated. The cost is that the predictability of the overall normalization of F_2^γ is lost. Essentially this means that given F_2^γ at some Q^2 we can calculate how it changes while moving to a different Q^2. The 'input' can come from experimental measurement or theoretical models or a mixture of both. Various parameterizations of F_2^γ exist. They are different and depend on the models and assumptions used to create them.

In terms of describing the actual Q^2 evolution of F_2^γ there are two essentially equivalent approaches. Hereafter what we will refer to as the OPE picture utilizes the operator product expansion (OPE) where the Q^2 dependence of certain coefficient functions can be calculated using renormalization group methods. F_2^γ can be reconstructed at a different Q^2 using these coefficient functions with inverse Mellin transforms. The References in [11] are an example of using the (OPE) picture to describe the Q^2 evolution of F_2^γ.

An equivalent technique that is perhaps more intuitive involves the evolution of parton distribution functions from which F_2^γ can be constructed. Hereafter will refer to this as the DGLAP picture. For the rest of our discussion we will only be concerned with this technique. The quark parton model (QPM) is well understood in relation to deep inelastic lepton nucleon scattering. As a first approximation the nucleon is viewed as being made up of partons which are identified as free quarks. Parton distribution functions (PDFs) can be defined which are probability distributions for a particular parton to have a certain fraction of the momentum of the particle of which it is a constituent. In this picture, scattering off a nucleon is pictured as the sum of incoherent scatterings off the constituent partons. Bjorken Scaling is seen to apply which means that the scattering is independent of the probe virtuality Q^2. The QCD improved parton model introduces corrections to the naive parton model. Here gluonic emissions account for the violation of Bjorken scaling. These ideas can be carried over to the analysis of photon structure where we account for deep inelastic scattering by recognizing the parton content of the photon and defining suitable PDFs accordingly. There are some major differences between the approach taken to the nucleon and the photon.

As a naive parton model of the photon we can start by taking the tree level

Bethe-Heitler result for the process $\gamma\gamma \to q\bar{q}$ in the limit $Q^2 \gg m_q^2$,

$$F_2^\gamma(x, Q^2) = \frac{N_c \alpha_{em}}{\pi} \sum_{i=1}^{f} x\, e_{q_i}^4 \left\{ [x^2 + (1-x)^2]\, ln \frac{Q^2(1-x)}{m_{q_i}^2 x} + 8x(1-x) - 1 \right\} \tag{1.16}$$

where N_c is the number of colours, f is the number of quark flavours and q_i is a quark of flavour i with mass m_{q_i}.

We can then define quark and anti-quark PDFs,

$$q_i^\gamma(x, Q^2) = \frac{N_c \alpha_{em}}{2\pi} e_{q_i}^2 \left\{ [x^2 + (1-x)^2]\, ln \frac{Q^2(1-x)}{m_{q_i}^2 x} + 8x(1-x) - 1 \right\} \tag{1.17}$$

such that,

$$F_2^\gamma(x, Q^2) = \sum_{i=1}^{2f} x\, e_{q_i}^2\, q_i^\gamma(x, Q^2) \tag{1.18}$$

where the sum to $2f$ is because a photon does not distinguish between quarks and anti-quarks, ie. $\bar{q}_i^\gamma = q_i^\gamma$.

The QCD corrections to this naive parton model are due to the fact that gluons can be emitted or absorbed by the strongly interacting quarks that form the partonic structure of the photon. Also at a higher order we must consider gluonic structure. The concept of splitting functions is introduced in order to account for the various possible QCD corrections that can take place.

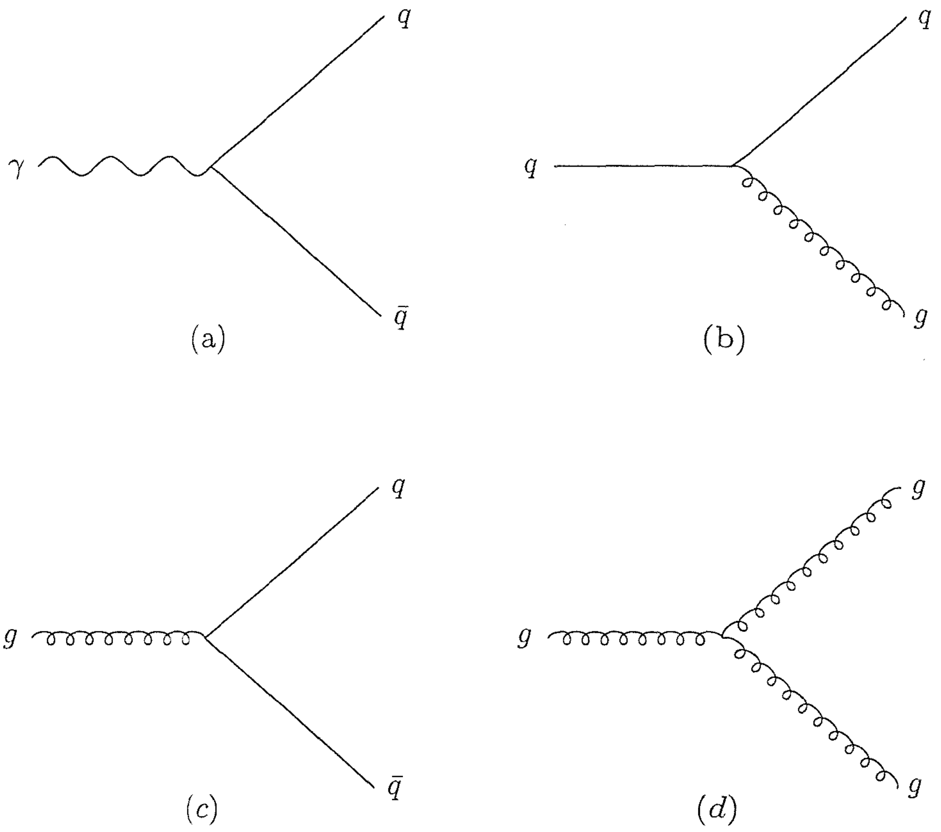

Figure 1.4: Vertices that give rise to splitting functions. (a) $P_{\gamma q}$, (b) P_{qq} or P_{qg}, (c) P_{gq} and (d) P_{gg}.

We group the contributions that can arise according to Figure 1.4. The target photon γ_p^* is viewed as consisting of partons, namely photons, quarks and gluons and PDFs give the probability of these partons having a momentum fraction x of the target photon. One can then assign a probability to the process of 'extracting' one of these partons from the target photon. Once extracted, the parton may then further split into other partons. One can calculate contributions arising from these processes using the diagrams in Figure 1.4. $P_{\gamma q}$, arising from process (a), will give rise to a splitting function. This function $P_{\gamma q}(x)$ will eventually turn out to have an intuitive interpretation in terms of the parton model. Given a photon γ that has a momentum fraction y, $P_{\gamma q}\left(x/y\right)$ is proportional to the probability of finding or extracting a quark of momentum fraction x from this photon. The same interpretation applies for (b), (c) and (d). For instance given a gluon g that has a momentum fraction y, $P_{gq}\left(x/y\right)$ is proportional to the probability of finding or extracting a quark of momentum fraction x from this gluon. This interpretation will become clearer when we introduce the full evolution equations.

In Figure 1.5 we can see the lowest order processes that correspond to the sub-processes in Figure 1.4. In (a), a photon parton being 'extracted' from the target photon is described by the photon PDF. A quark being 'extracted' from this photon parton is described by the $P_{\gamma q}$ splitting function. In (b), a quark parton being 'extracted' from the target photon is described by the quark PDF. A quark being 'extracted' from this quark parton is described by the P_{qq} splitting function. The explanation of the other diagrams follows by analogy.

In the OPE picture, each splitting function can be formally calculated as the inverse Mellin transform of the relevant anomalous dimension. Although we are not using this picture it is important to note that splitting functions are well defined calculable quantities that have a more intuitive interpretation in the DGLAP picture.

Given that we view F_2^{γ} as being described by PDFs, by imposing invariance

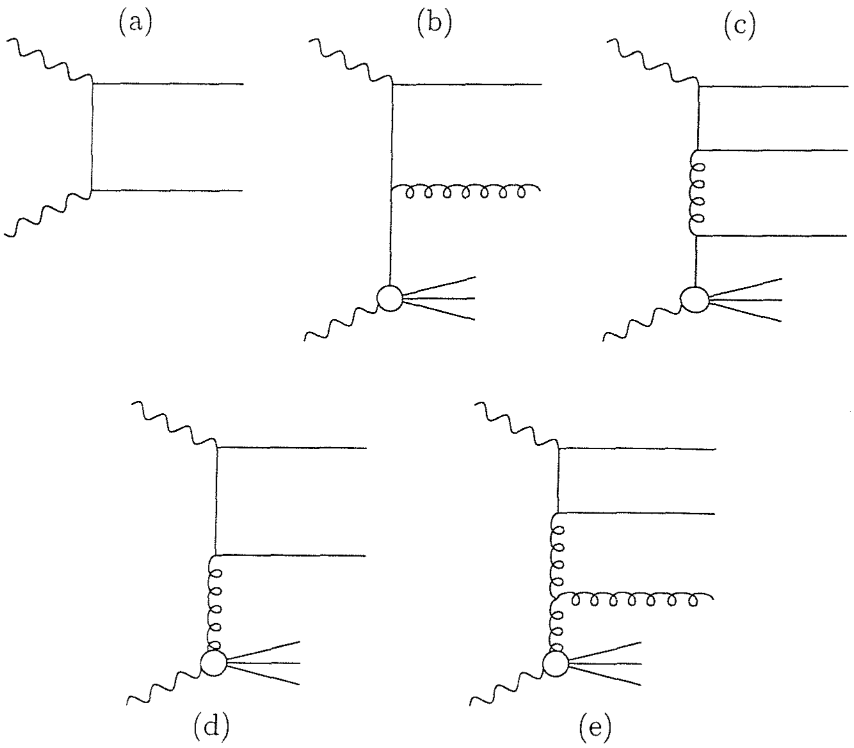

Figure 1.5: Lowest order processes that correspond to the splitting function vertices of Figure 1.4. (a) $P_{\gamma q}$, (b) P_{qq}, (c) P_{qg}, (d) P_{gq} and (e) P_{gg}.

of F_2^γ under scale transformations ie. the renormalization group, we obtain the Q^2 dependence of F_2^γ. This Q^2 dependence is given by the DGLAP equations and is actually given in terms of the Q^2 dependence of the PDFs. A complication is that the evolution is flavour dependent. Given that we have quark and anti-quark parton PDFs which are different for each flavour, a flavour singlet Σ and flavour non-singlets T_l must be defined. It must be remembered that when dealing with the photon PDFs that each quark distribution is equal to its anti-quark distribution ie. $q_i(x, Q^2) = \bar{q}_i(x, Q^2)$.

The singlet is given by

$$\Sigma(x,Q^2) \;=\; \sum_{i=1}^{f} [\, q_i(x,Q^2) + \bar{q}_i(x,Q^2) \,] \;=\; 2 \times \sum_{i=1}^{f} q_i(x,Q^2) \qquad (1.19)$$

where i runs over the number of active flavours f.

The non-singlets are given by,

$$\begin{aligned} T_3(x,Q^2) &= 2\,(u_q - d_q) \\ T_8(x,Q^2) &= 2\,(u_q + d_q - 2s_q) \\ T_{15}(x,Q^2) &= 2\,(u_q + d_q + s_q - 3c_q) \qquad (1.20) \\ T_{24}(x,Q^2) &= 2\,(u_q + d_q + s_q + c_q - 4b_q) \\ T_{35}(x,Q^2) &= 2\,(u_q + d_q + s_q + c_q + b_q - 5t_q) \end{aligned}$$

where u_q, d_q, s_q, c_q, b_q and t_q refer to the different flavour dependent quark distributions which are all functions of (x,Q^2). The factor of 2 accounts for anti-quarks. The amount of non-singlets depends on the number of active flavours. Each T_l is zero until the relevant threshold has been crossed to make the new quark flavour active. For example, only T_3, T_8 and T_{15} are relevant below the b-quark threshold.

There is also a gluon distribution $G(x, Q^2)$ which describes the gluonic parton content of the photon.

The relevant splitting functions are given by P_{ij} and K_i. These splitting functions have a perturbative expansion in the running coupling $\alpha_s(Q^2)$ such that,

$$P_{ij}(x, Q^2) = \left(\frac{\alpha_s(Q^2)}{2\pi}\right) P_{ij}^{(0)}(x) + \left(\frac{\alpha_s(Q^2)}{2\pi}\right)^2 P_{ij}^{(1)}(x) + \cdots \qquad (1.21)$$

$$K_i(x, Q^2) = \left(\frac{\alpha_{em}}{2\pi}\right) K_i^{(0)}(x) + \left(\frac{\alpha_{em}}{2\pi}\right)\left(\frac{\alpha_s(Q^2)}{2\pi}\right) K_i^{(1)}(x) + \cdots \qquad (1.22)$$

where α_{em} is practically constant as Q^2 changes.

The $P_{ij}^{(k)}$ are the standard set of quark and gluon splitting functions used in the evolution of the proton structure function F_2^p. The $K_i^{(k)}$ are the photon splitting functions. The difference between these two types of splitting function is discussed below when we give a more intuitive interpretation of the DGLAP picture.

The $P_{ij}^{(k)}$ and $K_i^{(k)}$ are not necessarily functions of just x. However, their Q^2 dependence only ever enters indirectly in terms of group theory factors. These group theory factors are a function of the active number of quarks which depends on Q^2. Henceforth when we refer to splitting functions we mean the $P_{ij}^{(k)}$ and $K_i^{(k)}$ in the expansions (1.21) and (1.22) rather than the generalised P_{ij} and K_i. The parameter k is used to refer to the order to which we are working. Using just $k = 0$ terms is called leading order (LO). Using both $k = 0$ and $k = 1$ terms is called next to leading order (NLO). We shall not go higher than (NLO) in this discussion.

The convolution $\otimes$ is defined between a splitting function and a distribution,

$$P_{ij}^{(k)} \otimes F_j \equiv \int_x^1 \frac{dy}{y} P_{ij}^{(k)}\left(\frac{x}{y}\right) F_j(y, Q^2) \tag{1.23}$$

where F_j can be either T_l, Σ or G.

The evolution of each non-singlet T_l is independent while the evolution of the singlet Σ and gluon G distributions require coupled equations.

The DGLAP equations are given by,

$$\frac{dT_l}{d\ln Q^2} = P_{TT} \otimes T_l + K_T \tag{1.24}$$

$$\begin{aligned} \frac{d\Sigma}{d\ln Q^2} &= P_{\Sigma\Sigma} \otimes \Sigma + P_{\Sigma G} \otimes G + K_\Sigma \\ \frac{dG}{d\ln Q^2} &= P_{G\Sigma} \otimes \Sigma + P_{GG} \otimes G + K_G \end{aligned} \tag{1.25}$$

Here we can now see the interpretation of the splitting function explicitly. If we drop the K_T term from Equation (1.24) for the moment and solve the resulting differential equation using an Euler single step solution in (LO) we obtain,

$$\begin{aligned} T_l(x,(ln\,Q^2)+\Delta(ln\,Q^2)) &= T_l(x,(ln\,Q^2)) \\ &+ \left[\frac{\alpha_s(Q^2)}{2\pi}\int_x^1 \frac{dy}{y}\,P_{TT}^{(0)}\left(\frac{x}{y}\right)T_l(y,Q^2)\right]\Delta(ln\,Q^2) \end{aligned} \tag{1.26}$$

This shows how partons with a momentum fraction y at Q^2 contribute to the distribution at x and at $(ln\,Q^2)+\Delta(ln\,Q^2)$. This would be seen more clearly still if T_l was split up into its constituent flavour structure. Then $(\alpha_s(Q^2)/2\pi)\,P_{TT}^{(0)}(x/y)\,\Delta(ln\,Q^2)$ corresponds to the probability change for finding a quark with momentum fraction x inside a quark with momentum fraction y. In fact if we drop all K_i terms from Equations (1.24) and (1.25) we end up with a homogeneous set of differential equations. This homogeneous set is exactly the required form of the DGLAP equations to evolve the PDFs of the proton. In this sense we can say that the homogeneous part of Equations (1.24) and (1.25) correspond to the hadron-like part of the photon structure. The K_i terms render the equations inhomogeneous and correspond to the point-like structure of the photon. This is the fundamental difference between photon and proton structure. There is no convolution involved with the K_i terms. Since the probability of extracting any other particle from a photon is of order α_{em}, the PDF for photonic structure must be proportional to $\delta(1-x)$ with order α_{em} corrections. This leaves the formal convolution, Equation (1.23), as a trivial integral and the result is just the photon parton splitting function K_i.

We take α_{em} to be constant at 1/137 for all Q^2.

The strong coupling $\alpha_s(Q^2)$ in (NLO) evolves according to

$$\frac{\alpha_s(Q^2)}{4\pi} = \frac{1}{\beta_0 \ln Q^2/\Lambda^2} - \frac{\beta_1}{\beta_0^3} \frac{\ln(\ln Q^2/\Lambda^2)}{(\ln Q^2/\Lambda^2)^2} \tag{1.27}$$

where $\beta_0 = 11 - 2f/3$ and $\beta_1 = 102 - 38f/3$. All expressions refer to the $\overline{MS}$ renormalization scheme hence we use $\Lambda_{\overline{MS}}$ which depends f. In order to evolve in (LO) we just set $\beta_1 = 0$.

Thus given a set of PDFs $q_i(x, Q_0^2)$ and $G(x, Q_0^2)$ at some Q_0^2, in principle we can evolve these to a different Q^2. In this QCD improved parton model of the photon, F_2^γ is defined in terms of PDFs.

We define the following useful quantities,

$$\langle e^k \rangle = \frac{1}{f} \sum_{i=1}^{f} e_{q_i}^k \tag{1.28}$$

$$q_{\text{NS}} = \sum_{i=1}^{f} \left(e_{q_i}^2 - \langle e^2 \rangle \right) (q_i + \bar{q}_i) \tag{1.29}$$

where f is the number of active flavours.

In (LO),

$$\frac{1}{x} F_2^\gamma(x, Q^2) = q_{\text{NS}}(x, Q^2) + \langle e^2 \rangle \Sigma(x, Q^2) \tag{1.30}$$

and in (NLO),

$$\begin{aligned}\frac{1}{x}F_2^\gamma(x,Q^2) &= q_{\rm NS}(x,Q^2) \; + \; \langle e^2\rangle\,\Sigma(x,Q^2)\\ &+ \frac{\alpha_s(Q^2)}{4\pi}\,B_q\otimes\left[q_{\rm NS}(x,Q^2)+\langle e^2\rangle\Sigma(x,Q^2)\right]\\ &+ \langle e^2\rangle\frac{\alpha_s(Q^2)}{4\pi}\,B_G\otimes G(x,Q^2)\\ &+ 3f\langle e^4\rangle\frac{\alpha_{em}}{4\pi}\,B_\gamma(x)\end{aligned} \tag{1.31}$$

The terms $B_q(x)$. $B_G(x)$ and $B_\gamma(x)$ are given in Reference [12] and account for contributions that do not have a $\ln Q^2$ dependence. They are calculated directly in the OPE picture and receive a convolution on undergoing a Mellin inversion from moment space to Bjorken x space. B_γ has no convolution by the same reasoning that the K_i terms in the DGLAP equations have no convolution associated with them.

Equation 1.31 is to some extent arbitrary. Reference [13] introduces what is called the DIS$_\gamma$ factorization scheme. This involves removing the B_γ term from F_2^γ and absorbing it into the quark distributions. This is compensated for by altering the $K_i^{(1)}$ splitting functions. We explain the relevance of this more thoroughly in Chapter 3 when we discuss the specific splitting functions that are used. However it is important to grasp that there is an interplay between the splitting functions that are used successively at each Q^2 as the distributions are evolved and the terms required to construct F_2^γ at any particular Q^2. This idea is also relevant to our treatment of the squark threshold as will also become apparent in Chapter 3.

Essentially we have defined a physically measurable quantity F_2^γ which is related to the cross section involved in electron positron scattering. There exist parameterizations of the parton distribution functions of the quarks and gluons 'inside' a virtual photon. Given the PDFs at some Q_0^2 we can evolve them to a different Q^2 using the inhomogeneous DGLAP equations. F_2^γ can then be obtained at that Q^2 from the evolved PDFs.

Our aim in the rest of the discussion is to introduce SUSY into the DGLAP picture of photon structure. This is relevant for the next generation of high energy colliders. The proposed e^+e^- linear colliders (LCs) will initially have a centre of mass energy of $500\,GeV$. Later it is hoped to extend this up to $1.5\,TeV$. This may well be above the SUSY threshold for squark and gluino production in which case there will be a supersymmetric contribution to F_2^γ. We also examine SUSY virtual corrections to the standard splitting functions which are relevant below as well as above the SUSY threshold.

Chapter 2

Introduction of SUSY

2.1 Motivation

Supersymmetry is a popular candidate for physics beyond the standard model. The simplest theory is the Minimal Supersymmetric extension of the standard model (MSSM).

Essentially SUSY is an elegant symmetry between fermions and bosons. Fermionic superpartners are introduced for the bosons present and bosonic superpartners are introduced for the fermions present. There are several reasons why people believe SUSY to exist in nature. Here we list some of the major reasons. The following material is in no way original and has been taken from [17].

Perhaps the most compelling argument for supersymmetry is the way in which it addresses the hierarchy problem. This is essentially to do with the instability of the bosonic scalar Higgs mass due to quadratically divergent radiative corrections in the standard model. In the standard model the Higgs mass, M_h, is of the order of the W mass, M_W, and is proportional to a vacuum expectation value. v. v^2 receives quadratically divergent radiative corrections which means that the natural scale for the Higgs mass is of the order of the Planck (M_P) or unification (M_{GUT}) scale. It is possible to adjust the relevant counterterms so that they cancel the quadratic divergences and maintain the required hierarchy $M_W \ll M_P$. However this requires fine tuning of the Higgs potential parameters to a ridiculously precise degree. Many consider this fine tuning to be unnatural. The bosonic quadratic divergences can be cancelled by corresponding fermionic divergences in order to keep the hierarchy $M_W \ll M_P$. By introducing supersymmetry (extra fermions for bosons and vice versa) this cancellation can be accomplished quite naturally to all orders of perturbation.

Given the three couplings of SU(3)× SU(2)× SU(1) in the standard model, we can evaluate these at M_Z and run them up to the Planck scale. If one uses the renormalization group equations of the standard model between M_Z and M_{SUSY} and those of supersymmetry between M_{SUSY} and M_P then the couplings will all meet at some M_U. This M_U is of the order of $10^{16}\, GeV$ for $M_{SUSY} \sim 1\, TeV$. If one does not introduce supersymmetry at M_{SUSY} then the couplings do not meet. There is much contention as to the significance of this unification. However for many people the fact that this unification occurs with sensible values for M_{SUSY} and M_U is deemed to be more than just coincidental.

Non-supersymmetric grand unified models predict proton decay rates that disagree with current experiment. This problem is fixed if one introduces supersymmetry into the grand unified models since the conventional proton decay modes become unobservable.

There is a significant portion of the total matter density of the universe that cannot be made up of conventional baryonic matter. The lightest supersymmetric particle is deemed to be an ideal candidate for this dark matter.

There is much current interest in superstrings which necessarily requires supersymmetry as an ingredient.

If supersymmetry is formulated as a local symmetry then a spin-2 graviton field must be introduced. This leads to SUGRA models in which gravity is unified with the other interactions. These SUGRA models reduce to general relativity in the appropriate limit.

We have only briefly alluded to a few concepts that suggest supersymmetry as a good theory to account for new physics. Given the possibility of SUSY effects being seen in the next generation of high energy colliders it is important to try to predict the measurable effects for photon structure.

In Chapters 3 and 4 we shall be concerned with introducing squarks and gluinos. Squarks are the scalar bosonic supersymmetric partners of fermionic quarks. Gluinos are the fermionic supersymmetric partners of gluons. In Chapter 5 we look at the production of charginos by explicitly calculating the relevant total cross section that arises from electron positron scattering. The charged vector bosons $W^{\pm}$ and the charged Higgs bosons $H^{\pm}$ have supersymmetric partners called winos and higgsinos respectively. Charginos actually arrange themselves into mass eigenstates which are in general superpositions of these winos and higgsinos.

2.2 DGLAP Equations with SUSY

Essentially we allow the photon to have a squark and gluino partonic content in addition to the quark and gluon content described in Chapter 1. PDFs are defined for squarks and gluinos.

Some current lower limits for squark and gluino masses are given below [26]. In the following, with the exception of $\tilde{t}$ and $\tilde{b}$, all scalar quarks are assumed to be degenerate in mass and $m_{\tilde{q}_R} = m_{\tilde{q}_L}$.

scalar quark : $\tilde{q}$ Mass m $> 250\,GeV$

scalar bottom quark : $\tilde{b}$ Mass m $40-75\,GeV$

scalar top quark : $\tilde{t}$ Mass m $> 86.4\,GeV$

gluino : $\tilde{g}$ Mass m $> 190\,GeV$

There are right and left handed squarks as well as anti-squarks for all six different flavours. For our purposes we assume that right and left handed distributions are equal and that squark and anti-squark distributions are equal. Thus for each flavour i, we define a generalised squark distribution $s_i(x, Q^2)$ such that

$$s_i(x, Q^2) \;=\; s_i^L(x, Q^2) \;=\; s_i^R(x, Q^2) \;=\; \bar{s}_i^L(x, Q^2) \;=\; \bar{s}_i^R(x, Q^2) \qquad (2.1)$$

This enables us to define flavour non-singlets S_l for the squark by analogy with Equation (1.20),

$$\begin{aligned}
S_3(x, Q^2) &= 4\,(u_s - d_s) \\
S_8(x, Q^2) &= 4\,(u_s + d_s - 2s_s) \\
S_{15}(x, Q^2) &= 4\,(u_s + d_s + s_s - 3c_s) \qquad (2.2) \\
S_{24}(x, Q^2) &= 4\,(u_s + d_s + s_s + c_s - 4b_s) \\
S_{35}(x, Q^2) &= 4\,(u_s + d_s + s_s + c_s + b_s - 5t_s)
\end{aligned}$$

where u_s, d_s, s_s, c_s, b_s and t_s refer to the different flavour dependent squark distributions which are all functions of (x, Q^2). The factor of 4 accounts for the equalities in Equation (2.1). Obviously the squarks have different masses according to their flavours. This means that each of the non-singlets is only relevant above the corresponding threshold. For example only S_3, S_8 and S_{15} are relevant below the b-squark threshold. However for simplicity in what follows we assume that all six squark flavours enter at the same energy. We will henceforth refer to this energy as the squark or SUSY threshold. This corresponds to all six flavours of squarks having the same mass which we refer to as the squark mass M_s.

The squark singlet is given by

$$\begin{aligned}\Gamma(x,Q^2) &= \sum_{i=1}^{f}[\,s_i^L(x,Q^2) \;+\; s_i^R(x,Q^2) \;+\; \bar{s}_i^L(x,Q^2) \;+\; \bar{s}_i^R(x,Q^2)\,] \\ &= 4\times\sum_{i=1}^{f} s_i(x,Q^2)\end{aligned} \tag{2.3}$$

This sum will essentially be over all six flavours of squarks since, as described before, we will be introducing all squarks simultaneously at the squark threshold corresponding to M_s.

Note that both the non-singlet distributions S_l and the singlet distribution Γ start at zero at the squark threshold.

The gluino distribution is introduced as $L(x,Q^2)$ corresponding to a gluino mass of M_g. In the analysis we take the gluino mass to be either greater than or equal to the squark mass.

The DGLAP Equations (1.24) and (1.25) are sufficient only up to the squark threshold. Immediately above the squark threshold we must include the squark contribution to the evolution of the distributions. Then when we pass through the gluino threshold both the squark and gluino contributions to the evolution must be included.

Essentially each of the quark and squark non-singlets couple together, ie. T_3 with S_3, T_8 with S_8, etc...

$$\begin{aligned}\frac{dT_l}{d\ln Q^2} &= P_{TT}\otimes T_l + P_{TS}\otimes S_l + K_T \\ \frac{dS_l}{d\ln Q^2} &= P_{ST}\otimes T_l + P_{SS}\otimes S_l + K_S\end{aligned} \qquad (2.4)$$

In the singlet sector the quark Σ, squark Γ, gluon G and gluino L distributions are coupled. Given that in general the gluino mass M_g is greater than the squark mass M_s the singlet sector evolution below the gluino threshold is given by,

$$\begin{aligned}\frac{d\Sigma}{d\,lnQ^2} &= P_{\Sigma\Sigma}\otimes\Sigma + P_{\Sigma G}\otimes G + P_{\Sigma\Gamma}\otimes\Gamma + K_\Sigma \\ \frac{dG}{d\,lnQ^2} &= P_{G\Sigma}\otimes\Sigma + P_{GG}\otimes G + P_{G\Gamma}\otimes\Gamma + K_G \\ \frac{d\Gamma}{d\,lnQ^2} &= P_{\Gamma\Sigma}\otimes\Sigma + P_{\Gamma G}\otimes G + P_{\Gamma\Gamma}\otimes\Gamma + K_\Gamma\end{aligned} \qquad (2.5)$$

and above the gluino threshold by,

$$
\begin{aligned}
\frac{d\Sigma}{d\,lnQ^2} &= P_{\Sigma\Sigma}\otimes\Sigma + P_{\Sigma G}\otimes G + P_{\Sigma\Gamma}\otimes\Gamma + P_{\Sigma L}\otimes L + K_\Sigma \\
\frac{dG}{d\,lnQ^2} &= P_{G\Sigma}\otimes\Sigma + P_{GG}\otimes G + P_{G\Gamma}\otimes\Gamma + P_{GL}\otimes L + K_G \\
\frac{d\Gamma}{d\,lnQ^2} &= P_{\Gamma\Sigma}\otimes\Sigma + P_{\Gamma G}\otimes G + P_{\Gamma\Gamma}\otimes\Gamma + P_{\Gamma L}\otimes L + K_\Gamma \\
\frac{dL}{d\,lnQ^2} &= P_{L\Sigma}\otimes\Sigma + P_{LG}\otimes G + P_{L\Gamma}\otimes\Gamma + P_{LL}\otimes L + K_L
\end{aligned}
\qquad (2.6)
$$

Obviously if we take the squark and gluino masses to be equal ie. $M_s = M_g$ then Equation (2.5) is not needed and we only use Equations (2.4) and (2.6) above the common squark gluino threshold.

The presence of SUSY particles affects the running of the strong coupling. In (LO) the general Q^2 dependence of the coupling is the same as in Equation (1.27). However the change from the pure QCD beta function to the supersymmetric beta function means that $\beta_0^{SUSY} = 11 - 2f_q/3 - 2 - f_s/3$, where f_q and f_s are the number of active flavours of quarks and squarks respectively. The new Λ_{SUSY} may be fixed by imposing continuity of the strong coupling across the squark threshold at $Q^2 = 4M_s^2$,

$$
\begin{aligned}
\alpha_s(Q^2 \to 4M_s^2) &= \left.\frac{4\pi}{\beta_0^{QCD}\ln\left(Q^2/\Lambda_{QCD}\right)}\right|_{Q^2=4M_s^2} \\
&= \left.\frac{4\pi}{\beta_0^{SUSY}\ln\left(Q^2/\Lambda_{SUSY}\right)}\right|_{Q^2=4M_s^2}
\end{aligned}
\qquad (2.7)
$$

For our purposes this simply means that the coupling is continuous at $Q^2 = 4M_s^2$ and β_0 changes from 7 to 3 at this point. This means that although still 'small', the coupling decreases less quickly above the SUSY threshold.

The splitting functions P_{ij} and K_i are now different above the squark threshold. We have quark (P_{Tj}, $P_{\Sigma j}$), squark (P_{Sj}, $P_{\Gamma j}$), gluon (P_{Gj}), gluino (P_{Lj}) and photon (K_i) splitting functions. There are small differences between these splitting functions and the non-SUSY splitting functions for quarks and gluons due to self-energy contributions from loops of squarks and gluinos, these having been calculated in [16] and [18]. The new splitting functions have a perturbative expansion as in Equations (1.21) and (1.22), however we only work to (LO) in the SUSY regime. An (NLO) analysis of photon structure above the SUSY threshold is beyond the scope of this discussion. Essentially by the time we reach the SUSY threshold α_s is sufficiently small that the (NLO) corrections are unimportant.

Again these splitting functions have an intuitive interpretation in the DGLAP picture. For example, given that a quark has been 'extracted' from the target photon with a fraction of momentum y and that the quark PDF describes the probability of this happening, $P_{TS}(x/y)$ describes the probability of then extracting a squark of momentum fraction x from this quark. Likewise, given that a photon has been 'extracted' from the target photon (or equivalently that the photon remains a photon) and that the photon PDF of unity with order α_{em} corrections describes the probability of this happening, $K_L(x)$ describes the probability of then extracting a gluino of momentum fraction x from this photon.

We will talk more explicitly about the choice of these SUSY splitting functions and especially how the squark threshold behaviour is treated in Chapter 3. However the framework for the evolution of the parton distributions is essentially the same above the SUSY threshold as below, being described by sets of inhomogeneous DGLAP differential equations. We can take parameterizations of quark and gluon distributions at some low energy Q_0^2 and evolve them through the SUSY threshold by including squark and gluon distributions that initially start at zero. Then at some Q^2 we can obtain F_2^γ from the following expression by analogy with Equations (1.30) and (1.31),

$$\begin{aligned} \frac{1}{x}\, F_2^\gamma(x,Q^2) &= q_{\mathrm{NS}}(x,Q^2) \;+\; \langle e^2\rangle\, \Sigma(x,Q^2) \\ &+\; s_{\mathrm{NS}}(x,Q^2) \;+\; \langle e^2\rangle\, \Gamma(x,Q^2) \\ &+\; 2\times 3f\langle e^4\rangle\, \frac{\alpha_{em}}{4\pi}\, B_\gamma^{sq} \end{aligned} \tag{2.8}$$

where,

$$s_{\mathrm{NS}} = \sum_{i=1}^{f} \left(e_{s_i}^2 - \langle e^2\rangle\right)\left(s_i^L + s_i^R + \bar{s}_i^L + \bar{s}_i^L\right) \tag{2.9}$$

and $\langle e^k\rangle$ has already been given in Equation (1.28).

The B_γ^{sq} term is not an (NLO) term so much as a different way in which we have treated the squark threshold. We discuss this term fully in Chapter 3. We only include Equation (2.8) at this point in order to make clear the strategy involved in calculating F_2^γ with and without SUSY contributions.

However Equations (1.30), (1.31) and (2.8) are essentially our master equations. We can now do two things. Firstly, we can ignore any SUSY contributions and evolve the distributions using Equations (1.24) and (1.25). Then by using Equation (1.30) or (1.31) we can predict values for F_2^γ at some Q^2 above the SUSY threshold. Secondly, we can fully include SUSY contributions and evolve the relevant distributions using Equations (2.4), (2.5) and (2.6). Then by using Equation (2.8) we can predict values for F_2^γ at the same Q^2 above the SUSY threshold. This will allow us to asses the significance of SUSY contributions to F_2^γ and allow us to say whether such contributions will be measurable in the next generation of high energy colliders.

Chapter 3

DGLAP Evolution through the SUSY Threshold

3.1 Theory and Formalism

We now have the DGLAP framework with which to examine the photon structure function F_2^γ at different energies. The energy Q^2, is the virtuality of the 'probe' photon in deep inelastic electron positron scattering from Equation (1.2). The DGLAP equations are differential equations describing the evolution of the relevant parton distribution functions in terms of the differential variable $\ln Q^2$. To utilize this framework the vast majority of the work was numerical. The key procedures are the convolution given in Equation (1.23) and the 'stepped' numerical solution of differential equations. The most important aspects of implementing these procedures numerically are relegated to Appendix A. This Chapter introduces the specific theory needed and the consequent results.

What we actually did was to take PDFs at the c-quark threshold and evolve them upwards through the b-quark, t-quark and SUSY thresholds. We could then compare F_2^γ at various energies with and without SUSY contributions.

We assumed the following quark masses,

$$\begin{aligned} M(c) &= 1.5\,GeV \\ M(b) &= 4.5\,GeV \\ M(t) &= 174\,GeV. \end{aligned}$$

In evolving the PDFs to the SUSY threshold we assume that the condition to excite quarks of flavour i is given by,

$$Q^2 \geq 4M_{q_i}^2 \tag{3.1}$$

This corresponds to simplistic thresholds of $3\,GeV$, $9\,GeV$ and $348\,GeV$ for the c, b and t quarks respectively. We did not invoke the full theoretical framework for dealing with heavy flavour quark contributions to the structure function as described in [20] and [21] for example. This is primarily because we were concerned with whether supersymmetry exhibits a measurable effect on the structure function rather than exact numerical predictions in threshold regions.

The parameterizations [14] that we used were functions of Q^2, P^2 and Bjorken x, given in Equations (1.2), (1.4) and (1.5) respectively. The Q^2 evolution of the various distributions given by the DGLAP equations is independent of P^2. Since only u, d and s quark distributions are provided by [14] we had to start evolving at the c-quark threshold, where the c-quark distribution is zero. We could not find reliable parameterizations which included for instance c-quark or b-quark distributions that were also dependent on P^2. Essentially this is why we had to start evolving at such a 'low' Q^2 compared to the SUSY threshold. The validity of the parameterizations that we used were constrained by the relation $Q^2 > 5P^2$. This limited P^2 to a maximum of $1.8\,GeV^2$ at the c-quark threshold which only gives a small ratio $r = P^2/Q^2 \simeq 10^{-6}$ at high Q^2 above the SUSY threshold. However even with such a small value for r some limited P^2 dependence was to be observed. In referring to the distributions we often only show the (x, Q^2) dependence since the P^2 dependence has nothing to do with the machinery of the evolution. P^2 is fixed once at the beginning of the evolution at the c-quark threshold. However we wanted to monitor the P^2 dependence of the evolution which is really just using slightly different input parameterizations at low Q^2.

Up to the SUSY threshold we used the standard QCD splitting functions in order to evolve the distributions. We evolve in (NLO) up to the t-quark threshold. We are going to take different values for the squark mass M_s and also we can only evolve in (LO) above the SUSY threshold. In order for us to be able to compare F_2^γ at high Q^2 for different values of M_s we must evolve to the same order when in the same energy range. Basically this means that we must evolve the distributions in (LO) above the t-quark threshold.

The P_{ij} type splitting functions are well known and used in the corresponding evolution equations for the proton, these were obtained from [15]. The K_i type inhomogeneous splitting functions are also well known and were obtained from [12] and [13]. In order to make sense of them, the 'plus' prescription must be defined. Wherever $(1-x)_+$ appears in a $P_{ij}^{(k)}$ splitting function its effect is understood by the following integral.

$$\int_0^1 dx \, \frac{f(x)}{(1-x)_+} = \int_0^1 dx \, \frac{f(x)-f(1)}{1-x} \tag{3.2}$$

This integral will always be present when the 'plus' prescription is required because each $P_{ij}^{(k)}$ always appears in an integral defined by the convolution in Equation (1.23).

The colour SU(3) QCD group theory factors are

$$\begin{aligned} C_F &= \frac{4}{3} \\ C_A &= 3 \\ T_R &= \frac{1}{2} \\ T_f &= T_R \times f \end{aligned} \tag{3.3}$$

The (LO) splitting functions are,

$$P_{TT}^{(0)}(x) = P_{\Sigma\Sigma}^{(0)}(x) = C_F \left[\frac{1+x^2}{(1-x)_+} + \frac{3}{2}\,\delta(1-x) \right] \tag{3.4}$$

$$P^{(0)}_{\Sigma G}(x) \;=\; 2fT_R\left[x^2+(1-x)^2\right] \tag{3.5}$$

$$P^{(0)}_{G\Sigma}(x) \;=\; C_F\left[\frac{1+(1-x)^2}{x}\right] \tag{3.6}$$

$$\begin{aligned} P^{(0)}_{GG}(x) \;&=\; 2C_A\left[\frac{x}{(1-x)_+}+\frac{1-x}{x}+x(1-x)\right] \\ &\quad +\delta(1-x)\frac{11C_A-4fT_R}{6} \end{aligned} \tag{3.7}$$

$$K^{(0)}_T(x) \;=\; 3f\left(\langle e^4\rangle-\langle e^2\rangle^2\right)2\left[x^2+(1-x)^2\right] \tag{3.8}$$

$$K^{(0)}_\Sigma(x) \;=\; 3f\langle e^2\rangle 2\left[x^2+(1-x)^2\right] \tag{3.9}$$

$$K^{(0)}_G(x) \;=\; 0^1 \tag{3.10}$$

The corresponding (NLO) formulae are very much longer and can be found in Appendix B.

Up to the t-quark threshold the evolution was carried out in (NLO) using the DIS$_\gamma$ prescription as described in [13]. This is slightly different from the straight $\overline{MS}$ scheme. The B_γ term in Equation (1.31) contains negative

---

[1] The point-like gluonic contribution only enters in (NLO)

divergences as $x \to 1$. The point of the DIS_γ prescription is that it eradicates these negative divergences that can push F_2^γ to unacceptable negative values. By a slight redefinition of the $K_i^{(1)}$ terms, the B_γ term becomes zero and is not used at all. In some sense there is a problem with consistency here since we evolve in (NLO) below the t-quark threshold and in (LO) above. If one is evolving in (NLO) then one should include the (NLO) convolutions that appear in Equation (1.31) when constructing F_2^γ from the distributions. However above the t-quark threshold and especially at high Q^2 above the SUSY threshold. α_s is sufficiently small that (NLO) contributions are less important. Given the choice to evolve in (LO) or (NLO) below the t-quark threshold, we chose to evolve in (NLO) where the coupling is larger and (NLO) effects are more pronounced. Given the choice to use the DIS_γ prescription or not, we chose to use it, primarily because it factors out the B_γ term which we would not be using anyway since above the SUSY threshold we would be only ever be constructing F_2^γ from the distributions in (LO). One further point is that we are most interested in whether supersymmetry exhibits a measurable effect on the structure function, so in a sense we just want to evolve the distributions in the most accurate way possible to the SUSY threshold which is where supersymmetric contributions will take effect.

So given $u_q(x, Q^2, P^2)$, $d_q(x, Q^2, P^2)$, $s_q(x, Q^2, P^2)$ and $G(x, Q^2, P^2)$ at $\sqrt{Q^2} = 3\,GeV$ (the c-quark threshold) from the parameterizations we can construct T_3, T_8, T_{15} and Σ from Equations (1.20) and (1.19) respectively. T_3, T_8, T_{15}, Σ and G are then numerically evolved from $3\,GeV$ to $9\,GeV$ (the b-quark threshold). In this region $\Lambda^4_{\mathrm{HO}} = 200\,MeV$ in Equation (1.27).

At $9\,GeV$, $b_q(x, Q^2, P^2)$ is introduced at zero. This enables us to construct T_{24}, which is actually equal to Σ at the b-quark threshold. T_3, T_8, T_{15}, T_{24}, Σ and G are then numerically evolved from $9\,GeV$ to $348\,GeV$ (the t-quark threshold). In this region $\Lambda^5_{\mathrm{HO}} = 131\,MeV$ in Equation (1.27).

At $348\,GeV$, $t_q(x, Q^2, P^2)$ is introduced at zero. T_{35} is constructed, which again is equal to Σ at the t-quark threshold. We are evolving the distributions to the SUSY threshold, corresponding to M_s. T_3, T_8, T_{15}, T_{24}, T_{35}, Σ and G are then numerically evolved in (LO) to $2M_s\,GeV$ (the squark threshold). In this region $\Lambda^6_{\mathrm{LO}} = 82\,MeV$ and β_1 is set to zero in Equation (1.27).

We took the squark mass in the range $175\,GeV \leq M_s \leq 300\,GeV$. At the squark threshold we can calculate F_2^γ using Equation (1.30). This will serve as a base reference so that we can compare how much F_2^γ changes with and without SUSY contributions above the SUSY threshold.

Above this energy we treat the squark threshold in a slightly different way. For squark production we are going to use the full threshold condition that squarks cannot be produced unless,

$$Q^2 \geq \left(\frac{x}{1 - x - xr}\right) 4M_s^2 \tag{3.11}$$

where r = P^2/Q^2. Importantly, this full threshold condition is dependent on both x and Q^2 whereas the condition $Q^2 \geq 4M_s^2$ is wholly dependent on Q^2. We attempt to apply this condition above $Q^2 = 4M_s^2$. At a particular Q^2, there will be a value of x,

$$x_s(Q^2) = \frac{1}{(4M_s^2/Q^2)+1+r} \tag{3.12}$$

above which squarks cannot be produced due to this condition. Similarly, at a particular 'low' value of Q^2 there will always be a sufficiently low value of $x \leq x_s(Q^2)$ such that squarks can always be produced.

There exist a set of SUSY splitting functions that are valid in the squark region given by Equation (3.11) and indeed apply in general when considering squarks and gluinos. It is possible to incorporate the squark threshold condition (Equation (3.11)) into each convolution (Equation (1.23)). Any particular convolution evaluated at x and Q^2 is an integral in a dummy variable y in the region $y \geq x$. Since all convolutions are done numerically, SUSY splitting functions can be used for $y < x_s(Q^2)$, where squarks can be produced and standard splitting functions can be used for $y > x_s(Q^2)$, where squarks cannot be produced. This will ensure that there is no contribution to the quark and gluon distributions due to squark or gluino effects below the true SUSY threshold given in Equation (3.11). Likewise it will ensure that there is no contribution to the squark and gluino distributions at all in any region of x and Q^2 where squarks cannot be produced. This means that for any $Q^2 \geq 4M_s^2$, F_2^γ with SUSY contributions will coincide with F_2^γ without SUSY contributions for $x > x_s(Q^2)$. F_2^γ is unaltered by SUSY contributions in the region $x \geq x_s(Q^2)$, as would be expected. As mentioned previously, the running of the strong coupling is affected by the presence of SUSY particles and we use the condition in Equation (3.11) to decide whether to use the SUSY altered coupling to calculate the change in each distribution at a particular x and Q^2. This will ensure that the evolution is governed by the correct coupling in any particular region of x and Q^2.

Applying Equation (3.11) in this way to the splitting functions and the coupling is not an ideal strategy for incorporating the squark threshold since for $Q^2 < 4M_s^2$ there will always be an $x < x_s(Q^2)$ such that squarks can be produced and one might say that the technique should have been applied for $Q^2 < 4M_s^2$. However it is an improvement on just using $Q^2 \geq 4M_s^2$ as a squark threshold condition.

In principle this type of procedure could have been applied throughout the whole evolution from the c-quark threshold. This would have meant starting the evolution with all distributions present and continually applying a set of threshold criteria like Equation (3.11) for all massive particles present. This would essentially have been a programming exercise of immense difficulty and perhaps intractable. This is another example of where we have been content to refrain from invoking every sophisticated method for treating heavy flavour contributions to the structure function. We allude to some of the programming techniques and difficulties in Appendix A.

The SUSY set of homogeneous (LO) splitting functions is taken from References [16] and [18]. They are used in Equations (2.4), (2.5) and (2.6).

$$P_{TT}^{(0)}(x) \;=\; P_{\Sigma\Sigma}^{(0)}(x) \;=\; C_F \left\{ \left[\frac{1+x^2}{(1-x)_+} \right] + \delta(1-x) \right\} \qquad (3.13)$$

$$P^{(0)}_{SS}(x) \;=\; P^{(0)}_{\Gamma\Gamma}(x) \;=\; C_F\left\{\left[\frac{1+x^2}{(1-x)_+}-(1-x)\right]+\delta(1-x)\right\} \tag{3.14}$$

$$P^{(0)}_{TS}(x) \;=\; P^{(0)}_{\Sigma\Gamma}(x) \;=\; C_F\,[1] \tag{3.15}$$

$$P^{(0)}_{ST}(x) \;=\; P^{(0)}_{\Gamma\Sigma} \;=\; C_F\,[x] \tag{3.16}$$

$$P^{(0)}_{\Sigma G}(x) \;=\; 2T_f\left[x^2+(1-x)^2\right] \tag{3.17}$$

$$P^{(0)}_{\Sigma L}(x) \;=\; 2T_f\;\;[1-x] \tag{3.18}$$

$$P^{(0)}_{G\Sigma}(x) \;=\; C_F\left[\frac{1+(1-x)^2}{x}\right] \tag{3.19}$$

$$\begin{aligned} P^{(0)}_{GG}(x) \;=\;& C_A\left[\frac{1+x^2}{(1-x)_+}+\frac{1+(1-x)^2}{x}-\left(x^2+(1-x)^2\right)\right] \\ &+\;[3C_A-2T_f]\;\delta(1-x) \end{aligned} \tag{3.20}$$

$$P^{(0)}_{G\Gamma}(x) \;=\; C_F\left[\frac{1+(1-x)^2}{x}-x\right] \tag{3.21}$$

$$P^{(0)}_{GL}(x) = C_A\left[\frac{1+(1-x)^2}{x}\right] \tag{3.22}$$

$$P^{(0)}_{\Gamma G}(x) = 2T_R\left[1-\left(x^2+(1-x)^2\right)\right] \tag{3.23}$$

$$P^{(0)}_{\Gamma L}(x) = 2T_R\,[x] \tag{3.24}$$

$$P^{(0)}_{L\Sigma}(x) = C_F\,[1-x] \tag{3.25}$$

$$P^{(0)}_{LG}(x) = C_A\left[x^2+(1-x)^2\right] \tag{3.26}$$

$$P^{(0)}_{L\Gamma}(x) = C_F\,[1] \tag{3.27}$$

$$P^{(0)}_{LL}(x) = C_A\left[\frac{1+x^2}{(1-x)_+}\right] + [3C_A - 2T_R]\,\delta(1-x) \tag{3.28}$$

The quark and gluon inhomogeneous terms $K^{(0)}_T(x)$, $K^{(0)}_\Sigma(x)$ and $K^{(0)}_G(x)$ are the same as before and given in Equations (3.8), (3.9) and (3.10). As with the gluon term, the photon to gluino splitting function is zero in (LO),

$$K^{(0)}_L(x) = 0 \tag{3.29}$$

The tree level squark contribution to F_2^γ is important in determining the photon to squark splitting function. K_S and K_Γ have the same functional x dependence in (LO) and are obtained from the tree level contribution to F_2^γ for squark production. This contribution for a left or right handed squark in deep inelastic scattering on a photon is calculated using ordinary perturbation theory [19],

$$\begin{aligned} F_{2,sq}^\gamma &= 3\, e_{sq}^4 \frac{\alpha_{em}}{\pi} x \Bigg\{ \; [1 - 8x(1-x) + \tau x(1-x)]\, v \\ &\quad + \left[2x(1-x) + \tau x(3x-1) + \frac{1}{2}\tau^2 x^2\right] \ln\left(\frac{1+v}{1-v}\right) \Bigg\} \end{aligned} \tag{3.30}$$

where,

$$\begin{aligned} \tau &= 4M_s^2/Q^2 \\ v &= [1 - \tau x/(1-x)]^{1/2} \end{aligned} \tag{3.31}$$

Neglecting squark masses we obtain K_S and K_Γ in the same way that the photon to quark splitting functions are obtained from the tree level contribution to F_2^γ for quark production,

$$K_S^{(0)}(x) = 2 \times 3f \left(\langle e^4\rangle - \langle e^2\rangle^2\right) 2\,[2x(1-x)] \tag{3.32}$$

$$K_\Gamma^{(0)}(x) = 2 \times 3f \,\langle e^2\rangle\, 2\,[2x(1-x)] \tag{3.33}$$

The factor of 2× accounts for left and right handed squarks. The other coefficients are standard. The $[2x(1-x)]$ is the most dominant term proportional to $\ln(Q^2/4M_s^2)$ in Equation (3.30) and accounts for the linear $\ln Q^2$ evolution of the distributions in (LO). In a sense we can imagine expanding Equation (3.30) in powers of $\ln(Q^2/4M_s^2)$ and comparing this with naively integrating the DGLAP equations in the variable $\ln Q^2$. On comparison we would find that we had correctly accounted for the $\ln Q^2$ evolution of F_2^γ up to order $(\ln(Q^2/4M_s^2))^2$. Any other contribution to F_2^γ that is not linear in $\ln(Q^2/4M_s^2)$ we will incorporate when we actually construct F_2^γ from the distributions at a particular Q^2 which we discuss a little later in this section.

All the squark $f_s(x, Q^2, P^2)$ are taken to be zero at the squark threshold. The distributions T_l, S_l, Σ, G and Γ can then be evolved to the gluino threshold at $2M_g\,GeV$ using Equations (2.4) and (2.5). As explained previously, above $Q^2 = 4M_s^2$ we impose the full squark threshold condition given in Equation (3.11). In regions of x and Q^2 where squarks cannot be produced we continue to run the strong coupling with the same Λ_{QCD} and β_0^{QCD} parameters used above the t-quark threshold. In regions of x and Q^2 where squarks can be produced the strong coupling is determined by the continuity condition in Equation (2.7). Λ_{SUSY} is not fixed in the sense that it depends on M_s for which we take a range of values. At the gluino threshold, $L(x, Q^2, P^2)$ is taken to be zero. The distributions T_l, S_l, Σ, G, Γ and L can then be evolved to any desired Q^2 using Equations (2.4) and (2.6). Alternatively, none of the SUSY splitting functions can be introduced and the original T_l, Σ and G distributions can be evolved from the squark threshold to the same Q^2 using Equations (1.24) and (1.25).

We can then obtain $F_2^\gamma(x, Q^2, P^2)$ in (LO), without SUSY contributions using

Equation (1.30),

$$\frac{1}{x} F_2^\gamma(x, Q^2) \;=\; q_{\rm NS}(x, Q^2) \;+\; \langle e^2 \rangle \, \Sigma(x, Q^2)$$

or with SUSY contributions using Equation (2.8),

$$\begin{aligned}\frac{1}{x} F_2^\gamma(x, Q^2) \;&=\; q_{\rm NS}(x, Q^2) \;+\; \langle e^2 \rangle \, \Sigma(x, Q^2) \\ &+\; s_{\rm NS}(x, Q^2) \;+\; \langle e^2 \rangle \, \Gamma(x, Q^2) \\ &+\; 2 \times 3f \langle e^4 \rangle \, \frac{\alpha_{em}}{4\pi} \, B_\gamma^{sq}\end{aligned}$$

All that remains is to explain the origin of the B_γ^{sq} term above. This is a slightly different way of treating the threshold behaviour than is in the literature.

We calculated the squark contribution to F_2^γ but for the case $P^2 \neq 0$, where $r = P^2/Q^2$, using the diagrams in Figure 3.1. The diagrams are squared and may be paramterized by invariance arguments so that F_2^γ or F_L^γ may be projected out after the calculation. There are no Dirac matrices over which to take a trace since squarks are scalar particles. The various scalar products that occur between the photon and squark momenta may be substituted for the standard centre of mass kinematics that assume $P^2 \neq 0$ and massive squarks. One can then integrate out the phase space of the squarks and project out the required quantity F_2^γ.

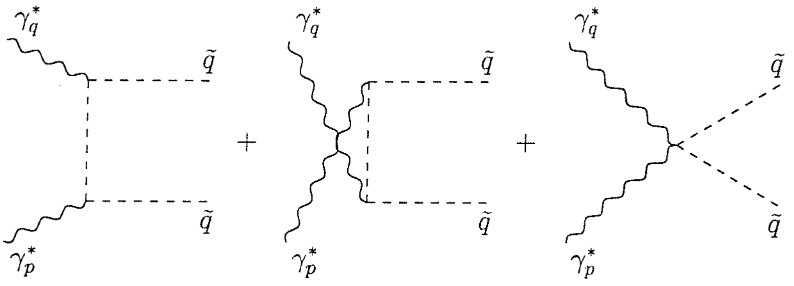

Figure 3.1: Diagrams contributing to $F^{\gamma}_{2,sq}$ in (LO). The $\tilde{q}$ are squarks.

$$F^{\gamma}_{2,sq} = 3\,e^4_{sq}\,\frac{\alpha}{\pi}\,x\left\{B\left(\frac{M_s^2}{Q^2}\right)^2\left(\frac{1}{FG}\right)\left(16x^2\right)\right.$$

$$+\;B\left(\frac{M_s^2}{Q^2}\right)\left(\frac{1}{FG}\right)\left(-48x^4r^2+48x^3r+4x^2r-8x^2\right)$$

$$+\;B\left(\frac{1}{FG}\right)\left(-12x^4r^3+12x^3r^2-2x^2r\right)$$

$$+\;B\left(1-6x^2r+6x^2-6x\right)$$

$$+\;\ln\left(\frac{F}{G}\right)\left(\frac{M_s^2}{Q^2}\right)^2\left(\frac{B}{\eta}\right)\left(8x^2/b\right)$$

$$+\;\ln\left(\frac{F}{G}\right)\left(\frac{M_s^2}{Q^2}\right)\left(\frac{B}{\eta}\right)\left(24x^4r^2/b+2x^2r/b+12x^2-2x/b-2x\right)$$

$$+ \ln\left(\frac{F}{G}\right)\left(\frac{B}{\eta}\right)\left(\frac{1}{2} + 6x^4r^3/b + 12x^4r^2/b - 12x^3r^2/b\right.$$

$$- 12x^3r/b + 11x^2r/b - 3x^2r + 4x^2/b - 6x^2 + \frac{1}{2}xr/b$$

$$\left. -\frac{1}{2}xr - 3x/b + 5x - \frac{1}{2b}\right)\Bigg\} \qquad (3.34)$$

where,

$$\begin{aligned} b &= 1 - 2xr \\ F &= 1 + \eta(1 - 2xr) \\ G &= 1 - \eta(1 - 2xr) \\ B &= \sqrt{1 - \frac{4M_s^2x}{Q^2(1 - x - xr)}} \\ \eta &= \left(\frac{B}{b}\right)\sqrt{1 - 4x^2r} \end{aligned}$$

In the above, Equation (3.30) is recovered for $r \to 0$.

In order to approximate the correct squark threshold behaviour we try to isolate that part of Equation (3.30) or (3.34) that is not used in the squark splitting functions and introduce this contribution as B_γ^{sq}. Essentially what we do is to take the squark contribution to F_2^γ and subtract off the $[2x(1-x)]$ part that accounted for the $\ln Q^2$ dependence in $K_S^{(0)}$ and $K_\Gamma^{(0)}$. Given that the coefficient of B_γ^{sq} is $(2 \times 3f\langle e^4\rangle\, \alpha_{em}/4\pi)$ in Equation (2.8),

$$B_\gamma^{sq} = 4\left\{\left(\frac{1}{3\, e_{sq}^4\, \frac{\alpha_{em}}{\pi}\, x}\right) \times F_{2,sq}^{\gamma} - 2x(1-x)\ln\left(\frac{Q^2}{4M_s^2}\right)\right\} \qquad (3.35)$$

where $F_{2,sq}^{\gamma}$ is given in Equation (3.30) or (3.34), will give the correct contribution. We also apply the squark threshold condition in Equation (3.11) to the B_γ^{sq} term so that in regions of x and Q^2 where squarks cannot be produced $B_\gamma^{sq} = 0$. The $2\times$ factor in the coefficient of B_γ^{sq} accounts for left and right handed squarks. We note that the difference between using Equation (3.30) and Equation (3.34) is negligible in our case because we are limited to $P^2 < 1.8\, GeV^2$ at the c-quark threshold, giving an $r \simeq 10^{-6}$ above the SUSY threshold.

However this is a different way of treating the threshold behaviour from that in [12]. At $Q^2 \gg 4M_s^2$ it satisfies the Renormalization Group equations since the dominant part is in the inhomogeneous term. In the region $Q^2 \simeq 4M_s^2$ this approach will reproduce the perturbative calculation with the correct threshold behaviour up to $(\ln(Q^2/4M_s^2))^2$. There should of course be a small mismatch at large Q^2 and large x. However we have eradicated this by incorporating the threshold condition from Equation (3.11) into both the splitting functions and the B_γ^{sq} term as explained above. Obviously Equation (3.30) exhibits a functional dependence on Q^2 that is more complicated than just $\ln Q^2$. This means that our choice of inhomogeneous squark terms do not fully describe the Q^2 evolution of F_2^γ and that our B_γ^{sq} term is also therefore an approximation. This can result in a discontinuity in the region $x_s(Q^2)$ which is definitely not the result of a physical effect. We will show this effect in our results in the next section.

It should be noted how quickly F_2^γ changes away from the threshold with decreasing x. In Equation (3.30), the term

$$v = [1 - 4M_s^2 x/Q^2(1-x)]^{1/2}$$

moves rapidly away from zero in decreasing x, meaning that the coefficients of

$$\ln\left(\frac{1+v}{1-v}\right) \quad \text{and} \quad v$$

in Equation (3.30) give rise to a real threshold contained in the B_γ^{sq} term.

To briefly summarize the strategy, we take parameterizations of quark and gluon distributions inside a virtual photon at the c-quark threshold. Using DGLAP inhomogeneous differential equations we evolve the relevant non-singlet, singlet and gluon distributions up to the SUSY threshold. From here we run the distributions separately, including or not, the effects of squarks and gluinos. At some $\sqrt{Q^2}$ we form F_2^γ for the virtual photon in such a way as to take account of the SUSY threshold condition.

3.2 Results

The variable parameters of the evolution are the P^2 (target virtuality), M_s (squark mass), M_g (gluino mass), Q^2 (incident virtuality) and Bjorken x. We took these in the ranges,

$$0 \leq \sqrt{P^2} \leq 1300\,MeV$$

$$175\,GeV \leq M_s \leq 300\,GeV$$

$$175\,GeV \leq M_g \leq 300\,GeV$$

$$500\,GeV \leq \sqrt{Q^2} \leq 1500\,GeV$$

and in all cases F_2^γ/α_{em} is actually plotted.

Figure 3.2 shows a generalised evolution to $1000\,GeV$. The bottom graph corresponds to F_2^γ evaluated at the SUSY threshold $\sqrt{Q^2} = 2M_s = 350\,GeV$. This serves as a base reference since it is at this point that the SUSY effects are included in the evolution. There is a considerable difference to F_2^γ when including supersymmetric effects. We agree with the general conclusions made in [19] that F_2^γ with SUSY contributions is flatter and strongly increases for decreasing values of x. Note that allowing the gluino mass to be greater than the squark mass produces a negligible effect. Note also that the graphs coincide above the squark threshold $x_s(Q^2)$ given in Equation (3.12), this being due to it being incorporated into the splitting functions and the B_γ^{sq} term, as described in the previous section.

From here on we plot $M_g = M_s$ since we have shown the $M_g > M_s$ difference to be negligible.

Figure 3.3 shows the Q^2 evolution of F_2^γ from $\sqrt{Q^2} = 500\,GeV$ up to $1250\,GeV$. As expected the structure function increases with increasing Q^2. The main point to note here is the appearance of discontinuities due to our approximate treatment of the squark threshold. For lower Q^2, closer to the squark threshold $2M_s = 350\,GeV$, the B_γ^{sq} term forces F_2^γ below its true value close to the squark production condition $x_s(Q^2)$ given in Equation (3.12). For higher Q^2, F_2^γ is no longer forced below its true value rather than forced to drop suddenly. These discontinuities are made clearer in Figure 3.4. Here at a fixed $\sqrt{Q^2} = 1000\,GeV$, we isolate the contributions due to the DGLAP evolution and due to the B_γ^{sq} term. The two 'dashed' graphs added together give the full SUSY F_2^γ. We can see that the SUSY graph without the B_γ^{sq} term is higher than the other graphs at $x_s(Q^2) = 0.89$. This is to be expected because the K_S and K_Γ terms that we obtained from the squark contribution to F_2^γ in Equation (3.30) are positive definite and cause F_2^γ to increase. It is by adding the rest of the squark contribution as B_γ^{sq} that the proper squark threshold behaviour is obtained. In a sense B_γ^{sq} is an over-compensation in low Q^2 and an under-compensation in high Q^2.

Figure 3.5 shows P^2 dependence up to $1300\,MeV$. We are limited by our parameterizations in that they are restricted in P^2 at the c-quark threshold. However non-negligible differences can be noted in low x even at $\sqrt{P^2} = 1300\,MeV$.

Figure 3.6 shows M_s dependence between $175\,GeV$ and $300\,GeV$. The lowest graph is without the SUSY contributions. As the squark mass M_s increases, F_2^γ approaches the non-SUSY limit as if the non-SUSY graph corresponds to exciting squarks of infinite mass. Also the thresholds move to lower x as the threshold condition Equation (3.11) requires higher Q^2 to produce squarks of higher mass. We can see that for $M_s = 300\,GeV$ there is a discontinuity around $x_s = 0.74$. This is due to the fact that our treatment of the squark threshold using the B_γ^{sq} term in Equation (2.8) is only approximate as discussed in the previous section. The discontinuity is more apparent for $M_s = 300\,GeV$ than for $M_s = 175\,GeV$ since the error increases as the ratio $4M_s^2/Q^2$ approaches unity.

Figures 3.7 and 3.8 show how F_2^γ varies with $\sqrt{Q^2}$ at two fixed values of x. Both graphs show how the distributions must approach the non-SUSY distribution for high M_s. However for $x = 0.66$ we can see the gradual approach to a threshold in increasing M_s. For $M_s = 275\,GeV$ it is evident that for low Q^2 squarks cannot be produced and the distribution coincides with the non-SUSY distribution. Then apart from the discontinuity mentioned previously the distribution rises in higher Q^2.

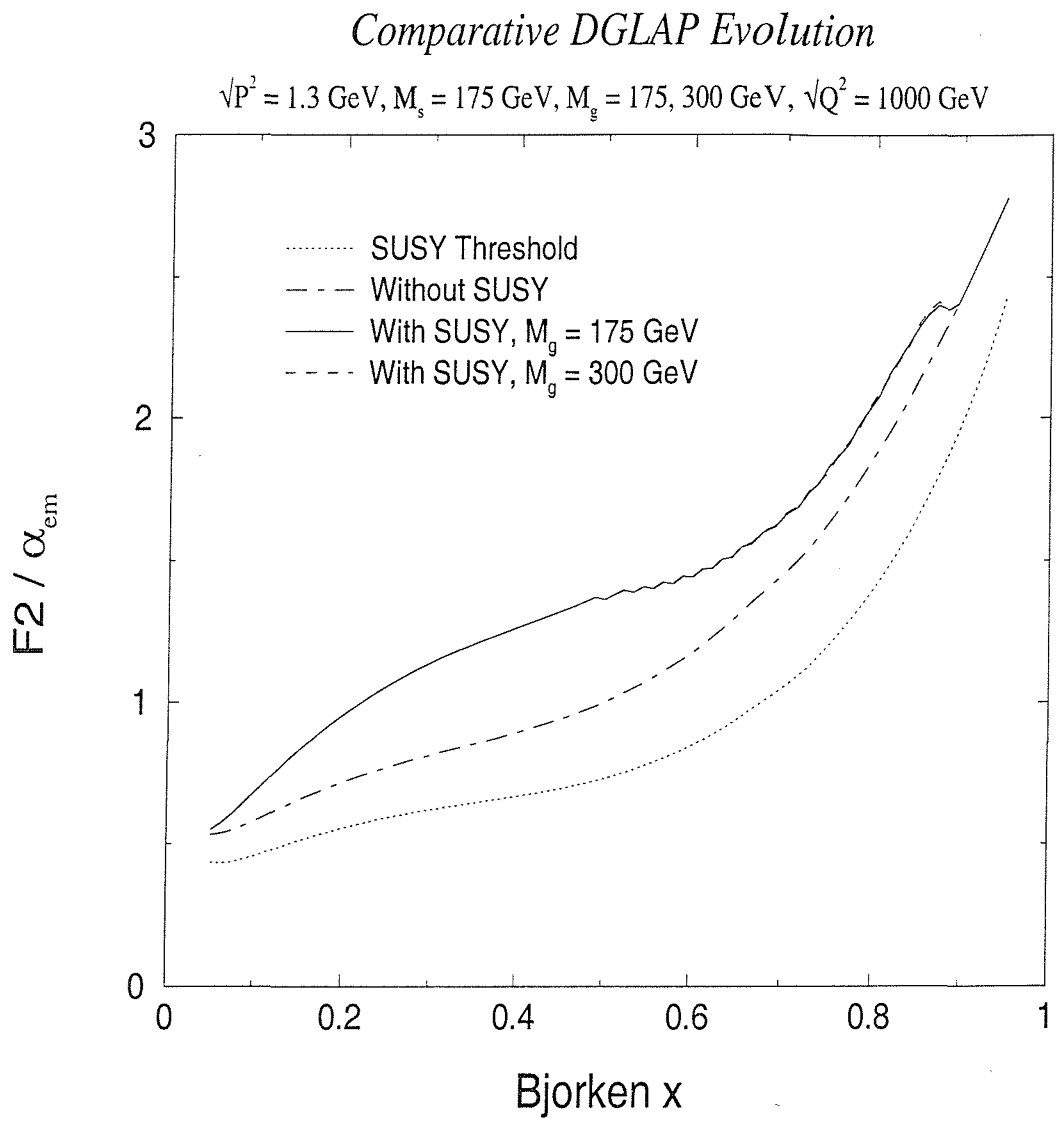

Figure 3.2: Comparative Evolution of Structure Function with and without SUSY splitting functions. Difference due to a higher gluino mass M_g is negligible.

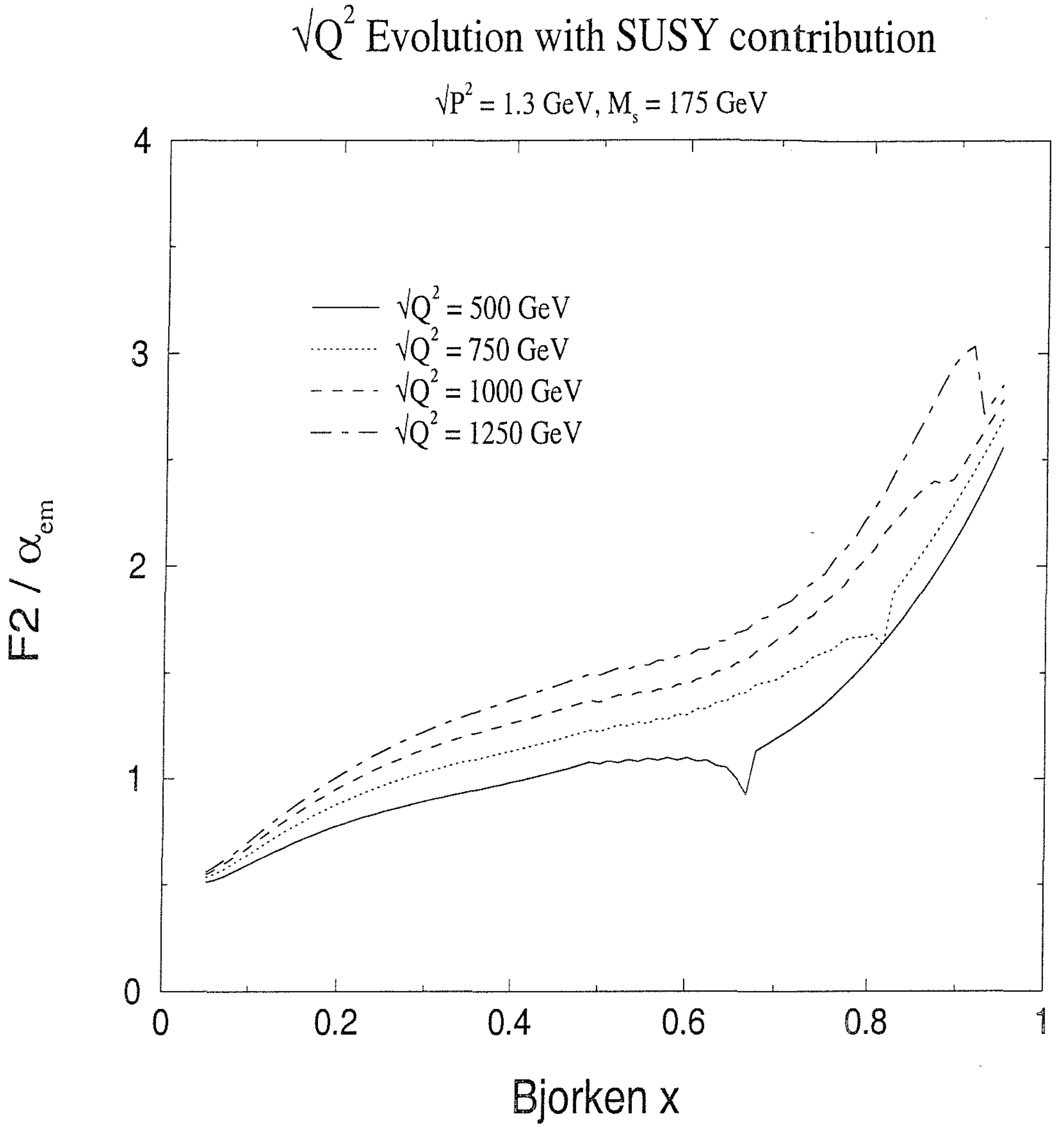

Figure 3.3: $\sqrt{Q^2}$ evolution of F_2^γ with SUSY contribution showing discontinuities for lower Q^2.

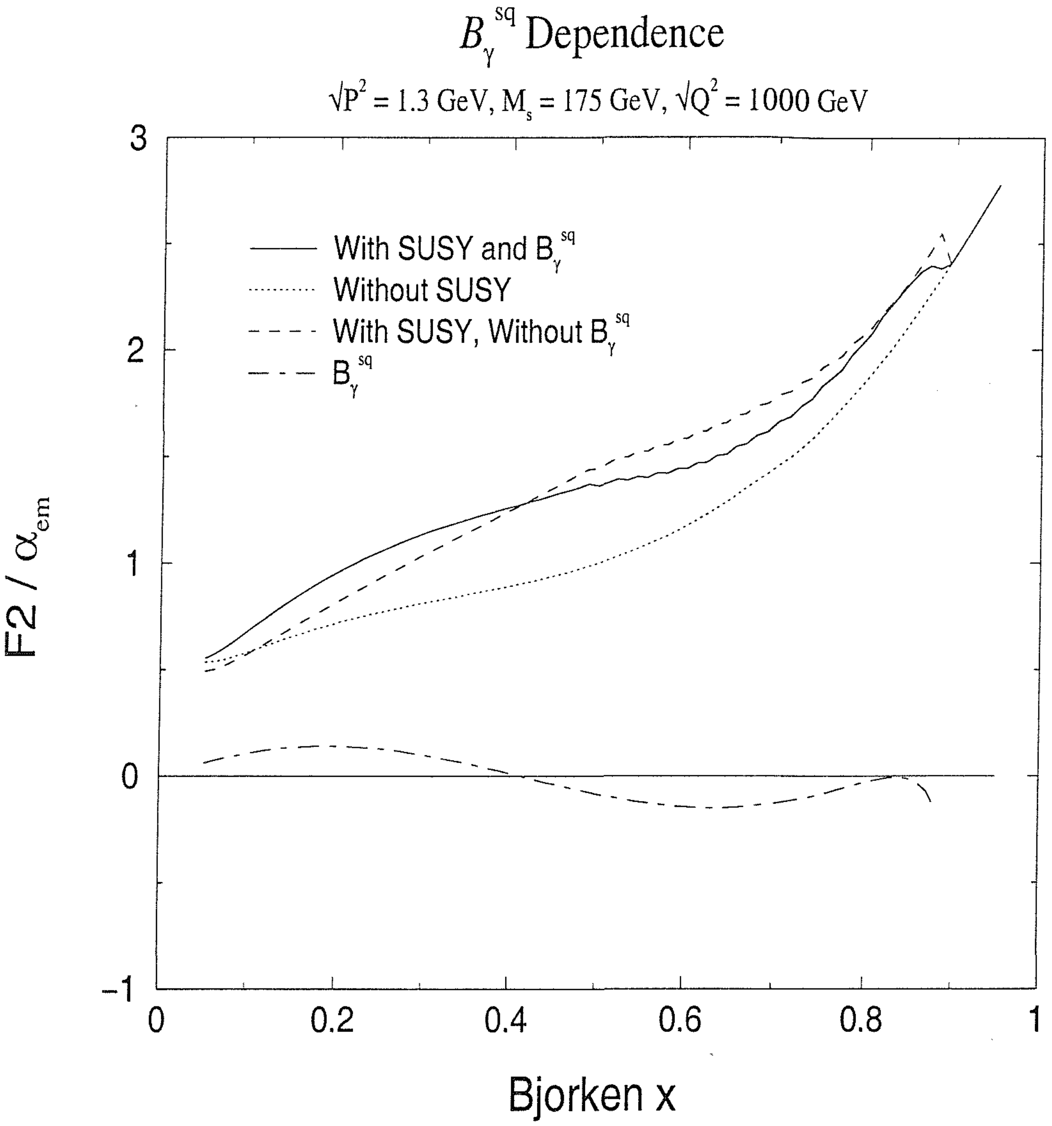

Figure 3.4: Graphs showing the effect of B_γ^{sq}.

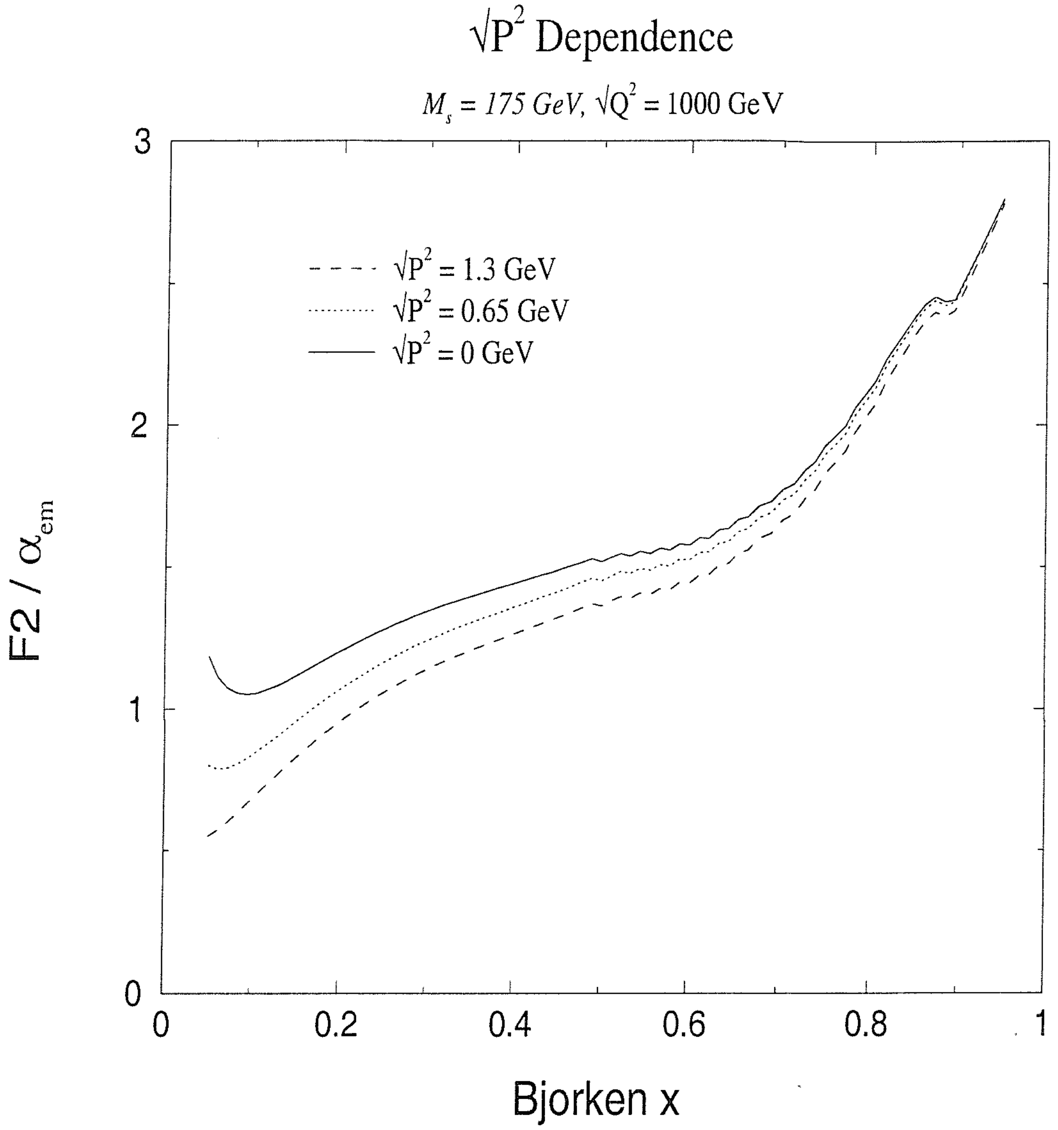

Figure 3.5: $\sqrt{P^2}$ dependence of structure function for fixed squark mass M_s at a fixed probe virtuality $\sqrt{Q^2}$.

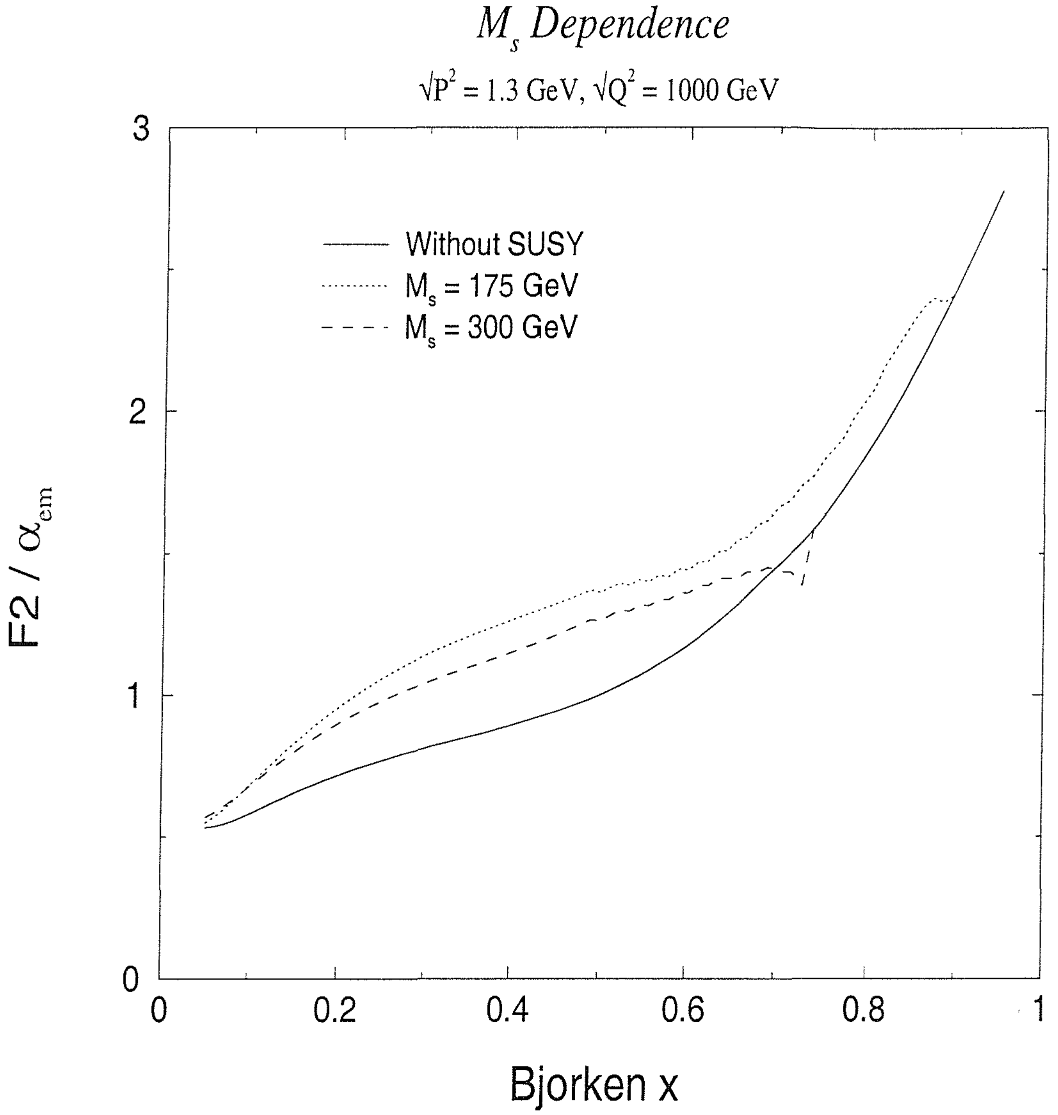

Figure 3.6: Dependence of structure function on squark mass M_s at a fixed target virtuality $\sqrt{P^2}$ and probe virtuality $\sqrt{Q^2}$.

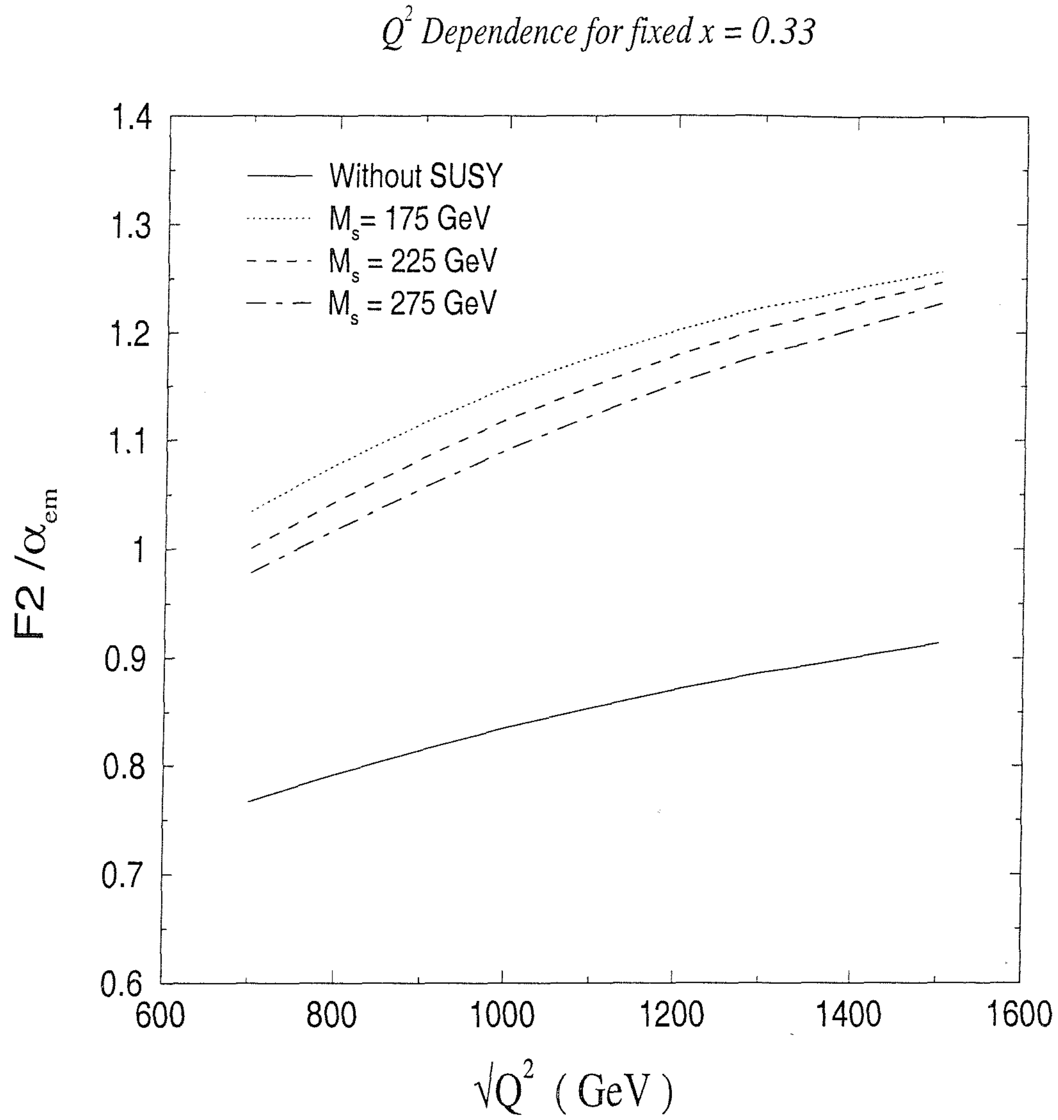

Figure 3.7: $x = 0.33$

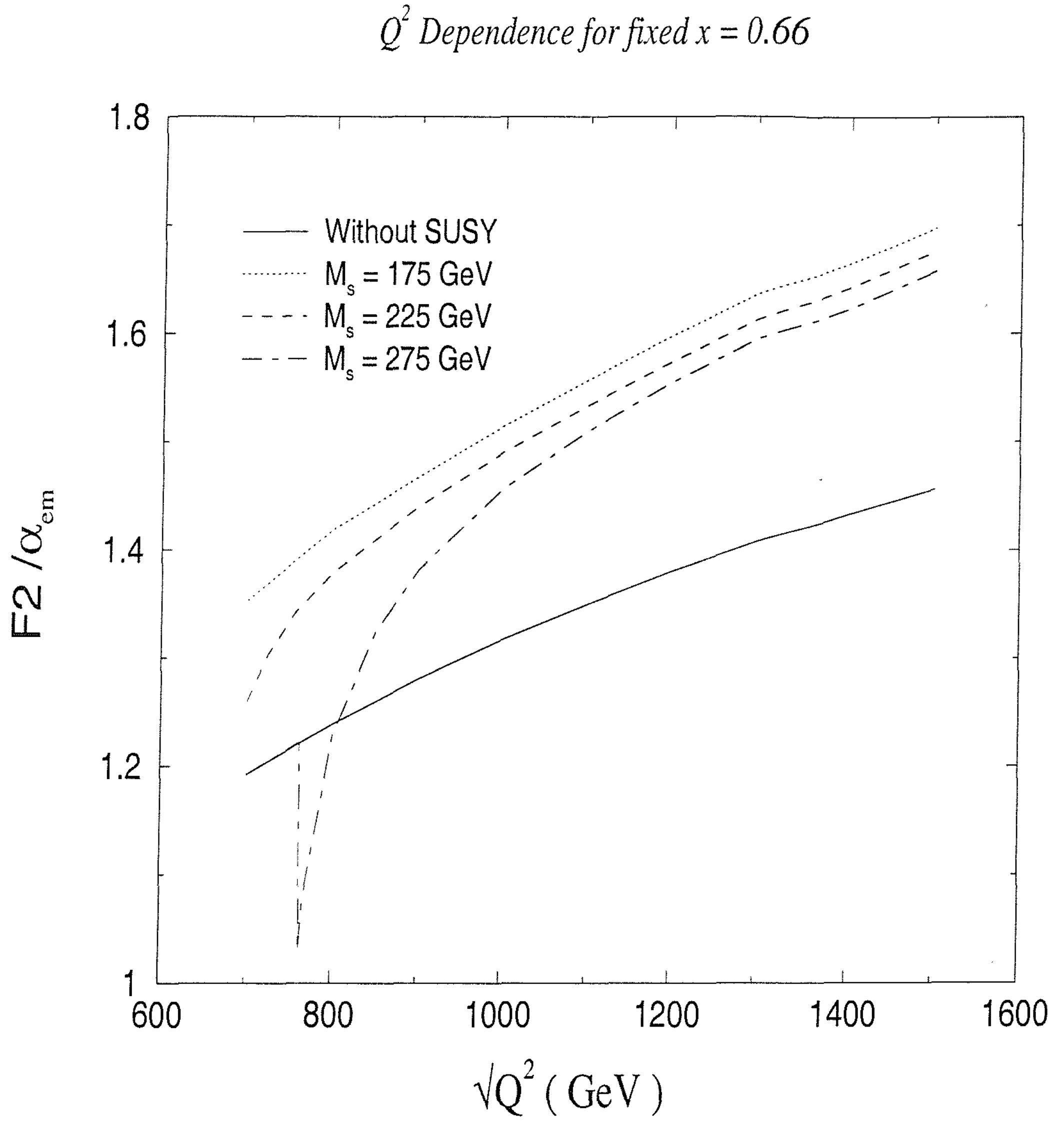

Figure 3.8: $x = 0.66$

3.3 Conclusions

We see from Figures 3.2 - 3.8 that if one can build a machine for which values of Q^2 approach 1 TeV^2 (about twice the squark production threshold) there is a substantial increase in the value of F_2^γ for the photon. Indeed, the evolution between the SUSY threshold and 1 TeV is more than doubled if SUSY particles, taken to have a mass of 175 GeV, are present. The difference between the structure functions with and without SUSY in the middle range of Bjorken-x is over 30%.

The effect at $Q^2 = 1$ TeV^2 is, of course, diminished if the SUSY threshold is increased. However, we note that taking the squark masses to 300 GeV only has a small effect on F_2^γ. Conversely, if the squark masses turn out to be substantially lighter than 175 GeV, (which is not currently ruled out), there would be a significant effect on the structure functions at values of Q^2 significantly below 1 TeV^2.

The effect also diminishes if the target photon is off-shell, as will usually be the case. However, we see from Figure 3.5 that this effect is modest.

The results are fairly insensitive to the mass of the gluino. This is not surprising as the gluino contributes very indirectly in that it can only be produced by a secondary emission from the target photon and then only probed through a further interaction with squarks. Taking the mass of the gluino below that of the squark, would have had a negligible effect as it is clear that it is the squark threshold and not the gluino threshold that must be crossed before there is any effect on the photon structure function.

There are two types of future experiments that would be relevant to probing the structure of the photon and measuring F_2^γ. Firstly a future e^+e^- linear collider would allow larger photon virtualities and larger photon photon centre of mass energies. Secondly there is the possibility of producing an $e\gamma$ collider. In principle an existing e^+e^- collider could be used with a high intensity laser beam. The photons from the laser undergo Compton backscattering with a beam of electrons already in the collider. The photons are scattered into a small cone around the initial electron direction and receive a large fraction of the electron energy. The benefits of this design are that the energy of the photons produced can be known fairly precisely and also high photon photon centre of mass energies can be produced for scattering from the available electron energies. It must be remembered that experimentally in all cases it is hard to get a sufficient rate for photon photon scattering. This is because the centre of mass energy is limited by realistic experimental considerations and thus Q^2 is also limited by experiment.

Chapter 4

Virtual corrections to inhomogeneous terms

4.1 Theory and Formalism

In this section we consider supersymmetric virtual corrections to F_2^γ. These will stem from loops made up of squarks and gluinos. We are not considering actual squark or gluino production but supersymmetric virtual contributions to possible quark or gluon production. This means that these virtual loops will contribute below the actual SUSY threshold as well as above it.

These contributions will be suppressed by the order of α_s compared to the tree level contributions. For example the diagrams in Figure 4.1 would give the tree level contribution to F_2^γ for quark production. This contribution corresponds to (LO). If we take any virtual loops due to squarks and gluinos then we obtain supersymmetric contributions suppressed by the order of α_s. These contributions correspond to (NLO) and are relevant below and above the SUSY threshold since they are virtual corrections. Now although these corrections are suppressed by α_s it is often the case [22] that (NLO) corrections are enhanced close to the threshold of the relevant particles. This means that the virtual squark and gluino loops could provide a signal for supersymmetric particles just below and at the SUSY threshold.

There are two groups of diagrams that give the virtual supersymmetric contributions to F_2^γ. The first set occur due to the production of quarks. Figure 4.1 shows the tree level diagrams for quark production in photon photon scattering. These must be used with the diagrams containing virtual supersymmetric corrections in Figure 4.2. This will give contributions of order $\alpha_{em}^2\alpha_s$, which corresponds to contributions of the same order as $K_i^{(1)}$ in the DGLAP picture discussed in the previous Chapters, see Equation (1.22). The diagrams can also have the incoming photon lines crossed. Diagram (h) is an example of Diagram (a) with crossed photon lines.

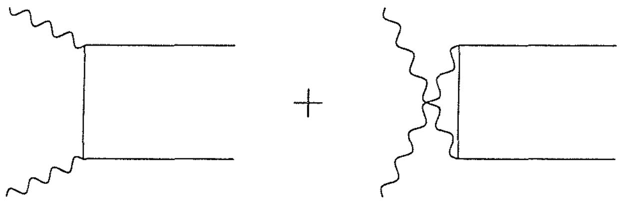

Figure 4.1: Tree level quark production diagrams to be used in conjunction with the diagrams in Figure 4.2.

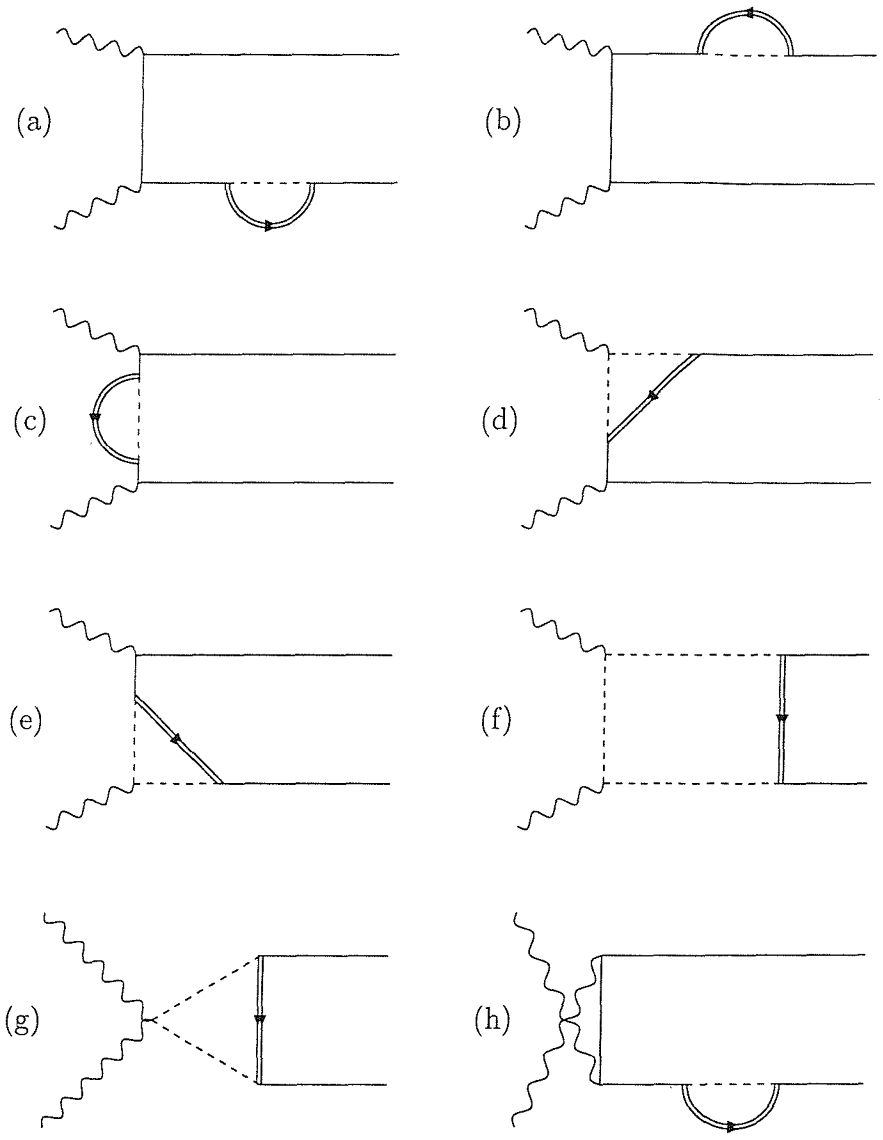

Figure 4.2: $(a) \rightarrow (g)$ are Supersymmetric Virtual diagrams that contribute to F_2^γ due to quark production. Diagrams with 'crossed' photons must be included, for example (h) is the 'crossed' photon diagram for (a).

The diagrams shown in Figure 4.3 occur due to the production of gluons in photon photon scattering. There are no tree level diagrams that form a product with these to produce contributions of the same order as $K_i^{(1)}$. In fact these diagrams must be squared and give a contribution of order $\alpha_{em}^2\alpha_s^2$ which is higher than (NLO) and beyond the order that we are considering. Thus we ignore this gluon contribution to F_2^γ.

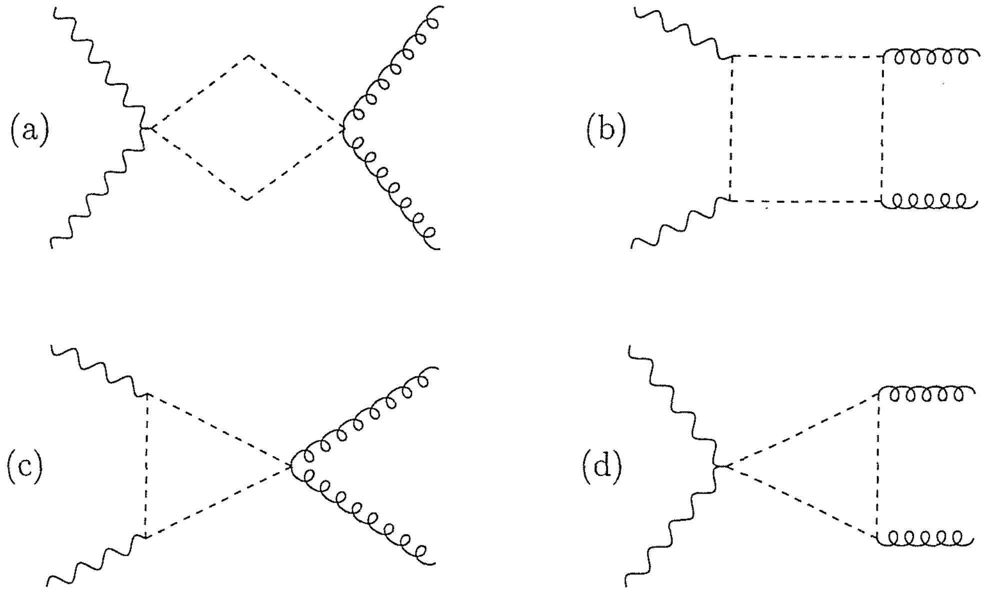

Figure 4.3: $(a) \rightarrow (d)$ are Supersymmetric Virtual diagrams that contribute to F_2^γ due to gluon production.

If we designate the diagrams in Figure 4.1 by M and the diagrams in Figure 4.2 by N, then the contribution that we are interested in follows from,

$$|M+N|^2$$

the actual contribution given by

$$M^*N + N^*M \;=\; 2\,\mathrm{Real}\,[M^*N]$$

The diagrams (a) to (f) in Figure 4.2 may be further simplified by using the fact that d*Lips* (Lorentz invariant phase space) is invariant under the interchange of the external quark momenta. If the external quark momenta are interchanged then each of the diagrams (a) to (f) is equivalent to another of the diagrams (a) to (f) with the incoming photon lines crossed. For example diagram (b) is equivalent to diagram (h) after this interchange. In fact it will turn out that the contribution from diagram (g) is zero, so we may write the required contribution as

$$4\,\mathit{Real}\,[M^*N]_{12\ \mathrm{diagrams}} \tag{4.1}$$

where '12 diagrams' refers to the six diagrams (a) to (f) of Figure 4.2 allowing for both left and right handed squarks.

The incoming photons carry Lorentz indices for actual calculative purposes. The 'probe' photon γ_q carries indices $\mu\,(\nu)$ and the 'target' photon γ_p carries indices $\rho\,(\sigma)$, where the bracketed indices refer to taking the complex conjugate of a particular diagram. We may write two useful quantities as,

$$F_{gg} \;=\; g_{\mu\nu}\left(-\frac{1}{2}\,g^{\rho\sigma}\right)\left\{4\,\mathit{Real}\left[(M^{\mu}_{\rho})^*(N^{\nu}_{\sigma})\right]_{12\ \mathrm{diagrams}}\right\}\,\mathrm{d}\mathit{Lips} \tag{4.2}$$

$$F_{pg} \;=\; \frac{p_\mu p_\nu}{(p\cdot q)}\left(-\frac{1}{2}\,g^{\rho\sigma}\right)\left\{4\,\mathit{Real}\left[(M^{\mu}_{\rho})^*(N^{\nu}_{\sigma})\right]_{12\ \mathrm{diagrams}}\right\}\,\mathrm{d}\mathit{Lips} \tag{4.3}$$

Since we carry out all the Dirac algebra and substitutions using the algebraic manipulation program FORM, the above contractions make the calculation more manageable since we then deal with scalar rather than vector quantities. These contractions are arbitrary in the sense that we could have used other equivalent pairs of contractions.

In order to regularize the divergencies that come up we work in $4-2\epsilon$ dimensions. The standard 4 dimensional $\mathrm{d}Lips$ for two quarks of momenta k and k' reduces as follows,

$$\begin{aligned}
\mathrm{d}Lips &= \frac{\mathrm{d}^4k}{(2\pi)^3}\,\delta(k^2-m^2)\frac{\mathrm{d}^4k'}{(2\pi)^3}\,\delta(k'^2-m^2)(2\pi)^4\,\delta(q+p-k-k') \\
&\to \frac{1}{8\pi}\left[\frac{4\pi x}{(1-x)\,Q^2/\mu^2}\right]^{\epsilon}\frac{1}{\Gamma(1-\epsilon)}\,(z)^{-\epsilon}\,(1-z)^{-\epsilon}\,\mathrm{d}z
\end{aligned} \tag{4.4}$$

where $z=(1-\cos\theta)/2$ and θ is the centre of mass scattering angle of the quark. We also take the quark mass m to zero.

In order to actually calculate F_2^γ we must average over the target polarization of photon γ_p. This averaging corresponds to the $\left(-\frac{1}{2}\,g^{\rho\sigma}\right)$ factors in Equations (4.2) and (4.3). We also take the target photon to be on-shell, i.e. $P^2=0$. Given the actual definition of F_2^γ and our particular choice of contractions in Equations (4.2) and (4.3), the contribution to F_2^γ for each flavour of quark i is given by,

$$F^{\gamma}_{2,Virtual} = \left(\frac{x\,\alpha_{em}}{e^4}\right)\left[6x\left(1+\frac{\epsilon}{3}\right)F_{pg} - (1+\epsilon)F_{gg}\right] \qquad (4.5)$$

where e is the charge on an electron and F_{pg} and F_{gg} are given in Equations (4.2) and (4.3) above. The colour and flavour dependent quantities such as $N_c = 3$ colours in SU(3) and E_{q_i} the fractional charge on each quark of flavour i are hidden in F_{pg} and F_{gg}.

We wish to calculate numerical quantities that can be utilized in the DGLAP analysis given in Chapter 3. We made use of Veltman-Passarino functions [23] in order to calculate the internal loops that come about in the diagrams from Figure 4.2. We used a C++ conversion of the Fortran subroutines in [24] in order to actually obtain numbers for these Veltman-Passarino functions. Since these loops are ultraviolet divergent we had to subtract off the pole parts in a consistent manner. We used on-shell renormalization in order subtract off the primitive divergences given in Figure 4.4.

One must be careful to extract the correct part of this calculation in order to use it in the DGLAP picture discussed in the previous Chapters. Equation (4.5) is a contribution to F_2^{γ} due to quark production and is the lowest order contribution due to virtual supersymmetric loops. From this expression we want to extract the inhomogeneous K_i part that can be used to calculate the virtual supersymmetric contribution to the $\ln Q^2$ evolution of F_2^{γ}. If we expand Equation (4.4) in ϵ there will be a term,

$$-\epsilon\,\ln Q^2/\mu^2$$

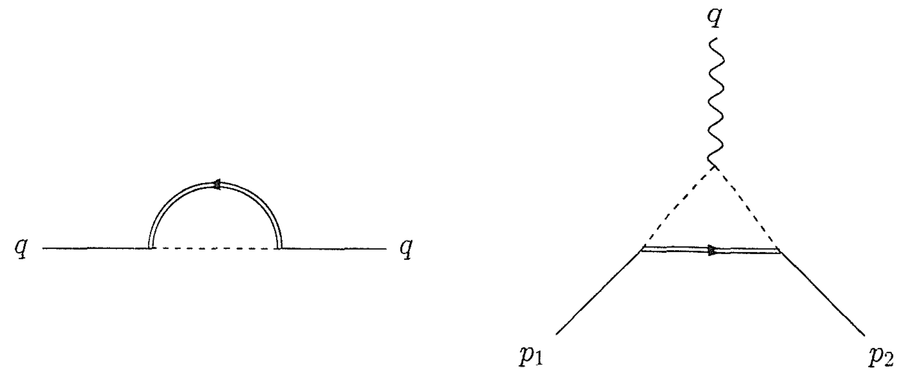

for $q^2 = 0$

(a)

for $q^2 = p_1^2 = p_2^2 = 0$

(b)

Figure 4.4: Primitive Divergences that are subtracted on-shell, (a) self-energy and (b) vertex.

and in calculating F_{gg} and F_{pg} from Equations (4.2) and (4.3) there will be terms proportional to $1/\epsilon$. If we multiply these terms together, the ϵ cancels out and we are left with terms proportional to $\ln Q^2/\mu^2$. These are the very same coefficients that we used in Chapter 3 in order to calculate the $K_i^{(0)}$ squark terms. The net result of this is that we only require the terms from F_{gg} and F_{pg} that are proportional to $1/\epsilon$. Apart from getting the correct coefficients, this then gives us a $K_{quark}^{(1)}$ term that we can use in the evolution of the DGLAP equations below and above the SUSY threshold. The main point of doing this is to see whether there are possible signals for supersymmetry due to virtual corrections below the actual SUSY threshold.

4.2 The Calculation

Each of the diagrams (*a*) to (*g*) in Figure 4.2 had to multiplied with the pair of tree level diagrams in Figure 4.1. Also allowances had to be made for left and right handed squarks and also crossed photon lines as in (*h*) of Figure 4.2.

The various internal loops involved correspond to integrals in the internal loop momenta. For example, in calculating diagram (c) of Figure 4.2, the following integral crops up due to the loop that is present,

$$\int \frac{\mathrm{d}^4 l}{(2\pi)^4} \frac{\not{t} + \not{l} - m}{(l^2 - m^2)((l+t)^2 - m^2)}$$

where l is the internal loop momentum and t is the difference between the incoming photon momentum q and the external quark momentum k. Now this integral may be written as

$$\frac{i}{16\pi^2} \left[(\not{t} - m) B_0(t^2, m^2, m^2) + \not{t} B_1(t^2, m^2, m^2) \right]$$

where B_0 and B_1 are the relevant Veltman-Passarino functions from [23] and [24]. However these B_i functions contain divergences corresponding to the the self-energy diagram given in (a) of Figure 4.3. We must subtract off the divergent value for these functions using the on-shell scheme. This means that the actual value we use for the above integral is,

$$\frac{i}{16\pi^2}\left[(\not{t}-m)\left\{B_0(t^2,m^2,m^2)-B_0(m^2,m^2,m^2)\right\} \right.$$

$$\left. +\ \not{t}\left\{B_1(t^2,m^2,m^2)-B_0(m^2,m^2,m^2)\right\}\right]$$

such that the divergent pole parts of B_0 and B_1 have been subtracted off along with a finite part defined by taking the external legs of the primitive divergence diagram to be on-shell. Here the on-shell momentum for t^2 is m^2, where m is the mass of an on-shell quark. As mentioned previously, we take quark masses to be zero. In order to extract numbers from the Veltman-Passarino function routines this means having $m^2 = 0$ or taking m^2 very small compared to the other momenta present.

The contributions due to (a) and (b) in Figure 4.2 are zero. This is because of the renormalization scheme. Since the external quarks are already on-shell, when we subtract off the divergent parts for these diagrams, we subtract the whole diagram leaving zero.

The contributions due to (c), (d) and (e) in Figure 4.2 are obtained by using B_i and C_{ij} Veltman-Passarino functions from [23] and [24]. Basically the B_i functions correspond to loop integrals with two quadratic denominators which stem from two propagators in the loop, for example the self energy diagram (a) in Figure 4.3. The C_{ij} functions correspond to loop integrals with three quadratic denominators which stem from three propagators in the loop, for example the vertex diagram (b) in Figure 4.3.

As mentioned previously the contribution due to (g) in Figure 4.2 evaluates to give zero. The most difficult contribution to calculate is that due to (f), the 'box' diagram. There are four propagators giving four quadratic terms in the denominator of the loop integral. We did not have routines for the corresponding Veltman-Passarino D functions and had to calculate them directly. By using a series of kinematic substitutions we cancelled out as many numerator and denominator terms as was possible. This left us with one scalar integral with four denominators, D_0 say, along with many B_i and C_{ij} type integrals. There was a check that could be applied here since the box integral is not divergent by power counting. In applying these kinematic substitutions we had introduced many extra divergences which were contained in the B_i and C_{ij} functions that were introduced. These divergences did indeed cancel out. A brief description of the scalar box calculation of D_0 is relegated to Appendix C.

In essence this allows us to calculate $F^{\gamma}_{2,Virtual}$ from Equation (4.5) in a semi-analytic manner. The relevant Feynman diagrams from Figure 4.2 are added together and multiplied with the tree level diagrams from Figure 4.1. The tensor algebra can be manipulated with FORM. The result is then contracted using the relations in Equations (4.2) and (4.3) in order to produce F_{gg} and F_{pg}. At this point any integrals due to loops present may be substituted for the relevant Veltman-Passarino functions remembering that the divergences must be subtracted off in a consistent manner as described above. The phase space of the outgoing quarks may also be integrated over. Everything must be multiplied by $-\epsilon$ with ϵ then subsequently being set to zero. As explained previously, this enables us to extract the lowest order contribution due to the virtual supersymmetric loops that is proportional to the required logarithmic term. Finally Equation (4.5) can be used in order to combine F_{gg} and F_{pg} into $F^{\gamma}_{2,Virtual}$. The resulting expression for $F^{\gamma}_{2,Virtual}$ is lengthy and is given in Appendix D but as $F^{\gamma}_{2,VS}$ which is defined in Equation (4.6). It appears as being analytic since the Veltman-Passarino functions appear as functions of Q^2, Bjorken x and the squark mass M_s. However it must be remembered that these are calls to routines that numerically evaluate these loop integrals. However once we have $F^{\gamma}_{2,Virtual}$ in this form it can be evaluated for any Q^2, Bjorken x and M_s. It can then be used directly to produce the relevant inhomogeneous K_i terms needed in the DGLAP evolution equations as explained below. Since the DGLAP evolution is carried out numerically we can utilize this semi-analytic form of $F^{\gamma}_{2,Virtual}$ directly.

In Chapter 3 we constructed the inhomogeneous $K_i^{(0)}$ squark terms in Equations (3.32) and (3.33) from the squark contribution to F_2^{γ}. They were obtained by taking the coefficient of the $\ln(1+v)/(1-v)$ in Equation (3.30). By analogy we have directly calculated the coefficient of the same logarithmic term but to a higher order and for the case of virtual supersymmetric corrections to F_2^{γ} for quark rather than squark production. We can do two things now.

Firstly, there is a term in the tree level Bethe-Heitler result for quark production, Equation (1.16), that is the coefficient of $\ln Q^2(1-x)/m^2x$ from which $K_i^{(0)}$ is obtained for the quark. This is

$$[x^2 + (1-x)^2]$$

We can compare this term and the one that we have calculated in order to get some idea of the relative magnitude of the effect of these virtual supersymmetric corrections. To compare these two properly we must make sure that they have the same coefficients. The correct expression is obtained by dividing out some factors from $F^{\gamma}_{2,Virtual}$ in Equation (4.5) to obtain $F^{\gamma}_{2,VS}$,

$$F^{\gamma}_{2,VS} = \left[1/\left(\frac{N_c E^4_{q_i} \alpha_{em}}{\pi} x\right)\right] F^{\gamma}_{2,Virtual} \tag{4.6}$$

As mentioned previously $F^{\gamma}_{2,VS}$ is given in Appendix D.

Secondly, we can obtain a $K^{(1)}_i$ that accounts for the contribution of these virtual supersymmetric corrections to the $\ln Q^2$ evolution of the DGLAP equations with the correct coefficients and use it directly in the equations above and below the SUSY threshold. In this case we need to remove a factor of $(\alpha_s/2\pi)$ since this will be included in our calculation but has been removed from the $K^{(0)}_i$ terms in the expansion definition given in Equation (1.22). The correct quantities are,

$$K^{(1)}_{T,VS}(x) = 3f\left(\langle e^4\rangle - \langle e^2\rangle^2\right) 2\,\frac{1}{(\alpha_s/2\pi)}\, F^{\gamma}_{2,VS} \tag{4.7}$$

$$K^{(1)}_{\Sigma,VS}(x) = 3f\,\langle e^2\rangle\, 2\,\frac{1}{(\alpha_s/2\pi)}\, F^{\gamma}_{2,VS} \tag{4.8}$$

4.3 Results

The Figures in this section show the properties of the contribution that we have calculated. We have plotted

$$R_{F_2^\gamma} = \frac{F_{2,VS}^\gamma}{[x^2 + (1-x)^2]} \times 100\% \tag{4.9}$$

which as mentioned in the previous section offers a direct comparison between the virtual contribution that we have calculated and the tree level result for quark production. At all times we have taken the squark mass M_s to be $300\,GeV$.

Figure 4.5 shows $R_{F_2^\gamma}$ plotted at Bjorken $x = 0.5$ for $\sqrt{Q^2}$ between $200\,GeV$ and $800\,GeV$. $R_{F_2^\gamma}$ is smooth and small in magnitude, less than 0.25% for $x = 0.5$. The full squark threshold production condition, Equation (3.11), reduces to

$$Q^2 = \left(\frac{x}{1-x}\right) 4M_s^2 \tag{4.10}$$

where there is no dependence on P^2 since it is assumed that $P^2 = 0$ in this calculation. As mentioned previously, we might have expected some structure as $\sqrt{Q^2}$ approached this condition. Section D.2 in Appendix D shows how individual terms in the solution can exhibit structure but that the sum of all contributions gives a smooth curve. In this particular case the condition coincides with $\sqrt{Q^2} = 600\,GeV$ where there is only the smooth main curve with no structure.

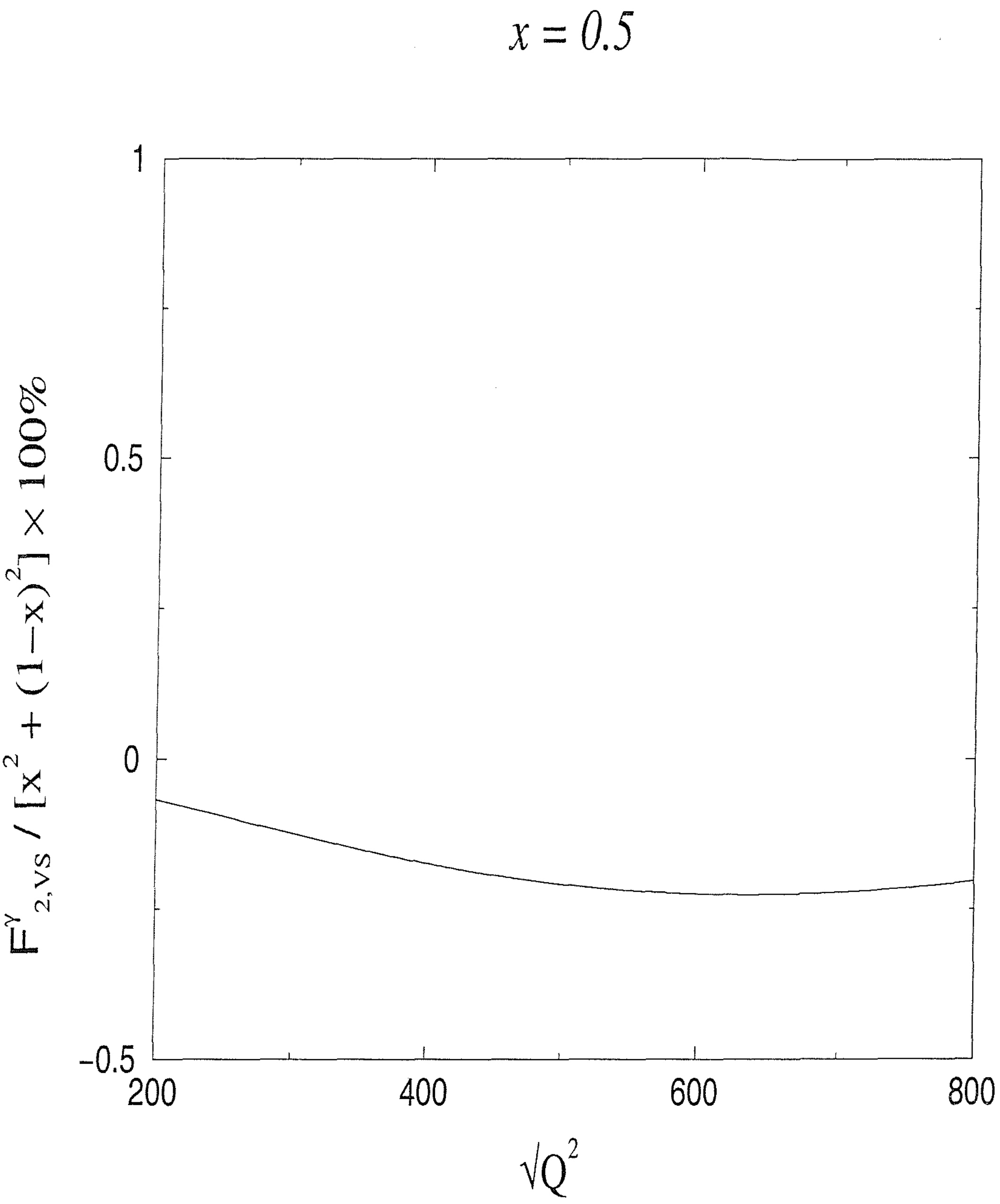

Figure 4.5: $F^{\gamma}_{2,VS}/[x^2+(1-x)^2] \times 100\%$ for $x = 0.5$ and Squark mass $M_s = 300\,GeV$.

Figures 4.6 - 4.9 show $R_{F_2^\gamma}$ plotted at $\sqrt{Q^2} = 300$, 600, 800 and 1200 GeV respectively for all Bjorken x. These are useful plots because it is easy to visualise what is happening during the actual evolution of the DGLAP equations. As the PDFs are evolved in $\ln Q^2$, at each discrete step the inhomogeneous terms are added with no convolution, see section A.3.

The contribution due to the continuous main curve is basically negligible being never more than 1% until after $\sqrt{Q^2} = 1\,TeV$ is reached. There is central negative portion which becomes narrower and eventually positive as higher $\sqrt{Q^2}$ is reached. At low x the curve is initially negative for very low $\sqrt{Q^2}$ but becomes positive and increases in intensity with increasing $\sqrt{Q^2}$. At high x the curve is positive and becomes increasingly more so with increasing $\sqrt{Q^2}$.

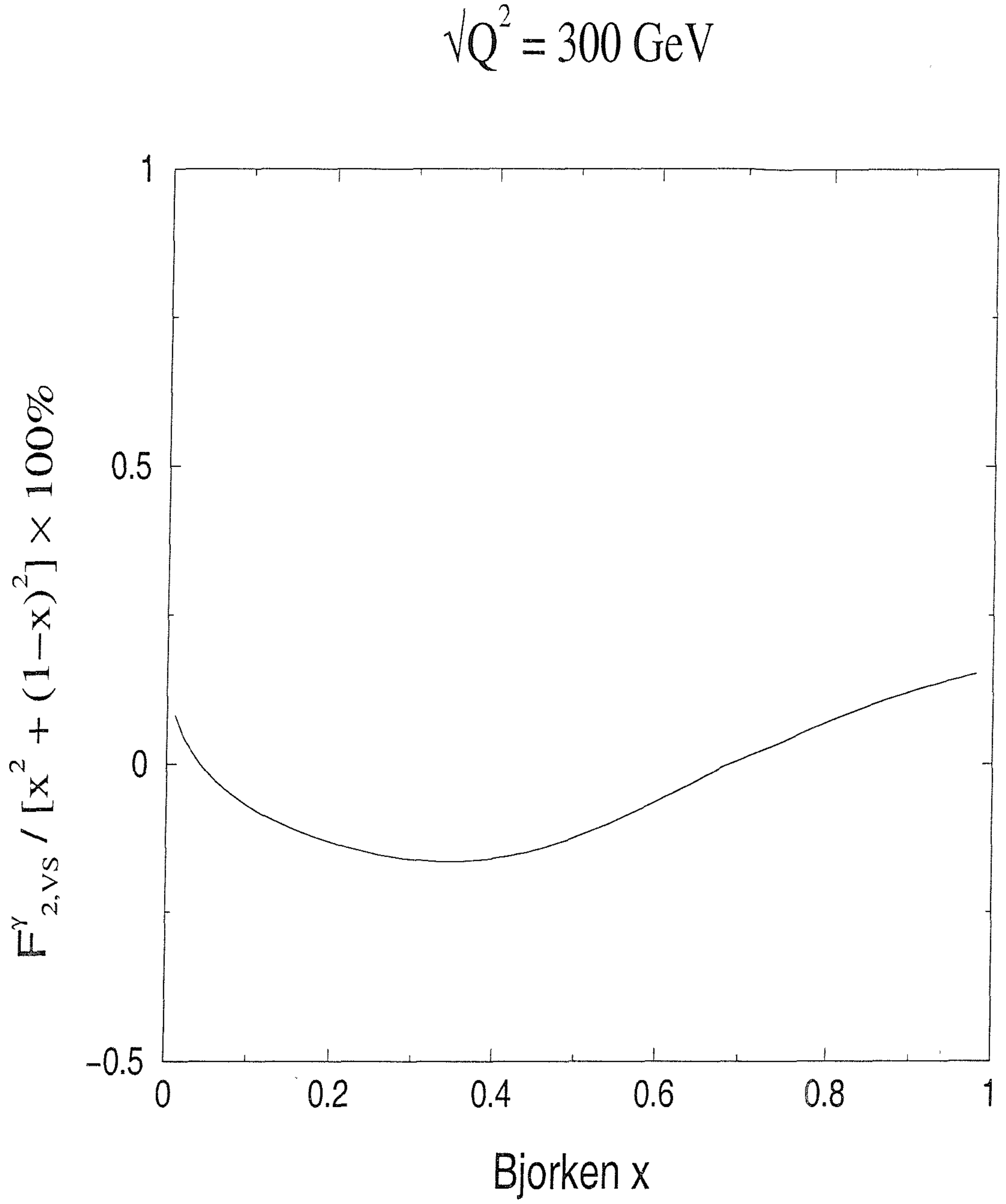

Figure 4.6: $F^{\gamma}_{2,VS}/[x^2 + (1-x)^2] \times 100\%$ for $\sqrt{Q^2} = 300\,GeV$ and Squark mass $M_s = 300\,GeV$.

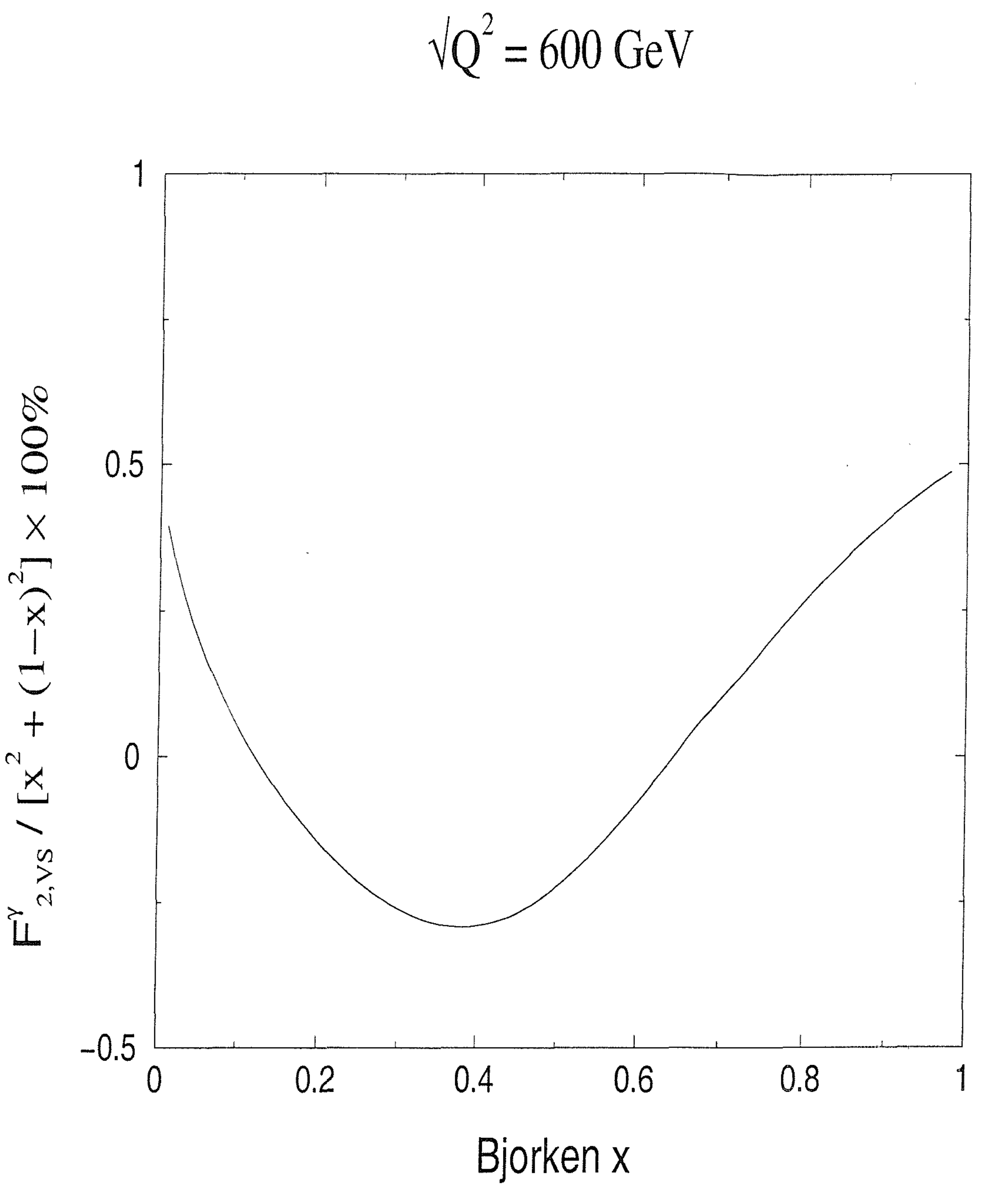

Figure 4.7: $F^{\gamma}_{2,VS}/[x^2 + (1-x)^2] \times 100\%$ for $\sqrt{Q^2} = 600\,GeV$ and Squark mass $M_s = 300\,GeV$.

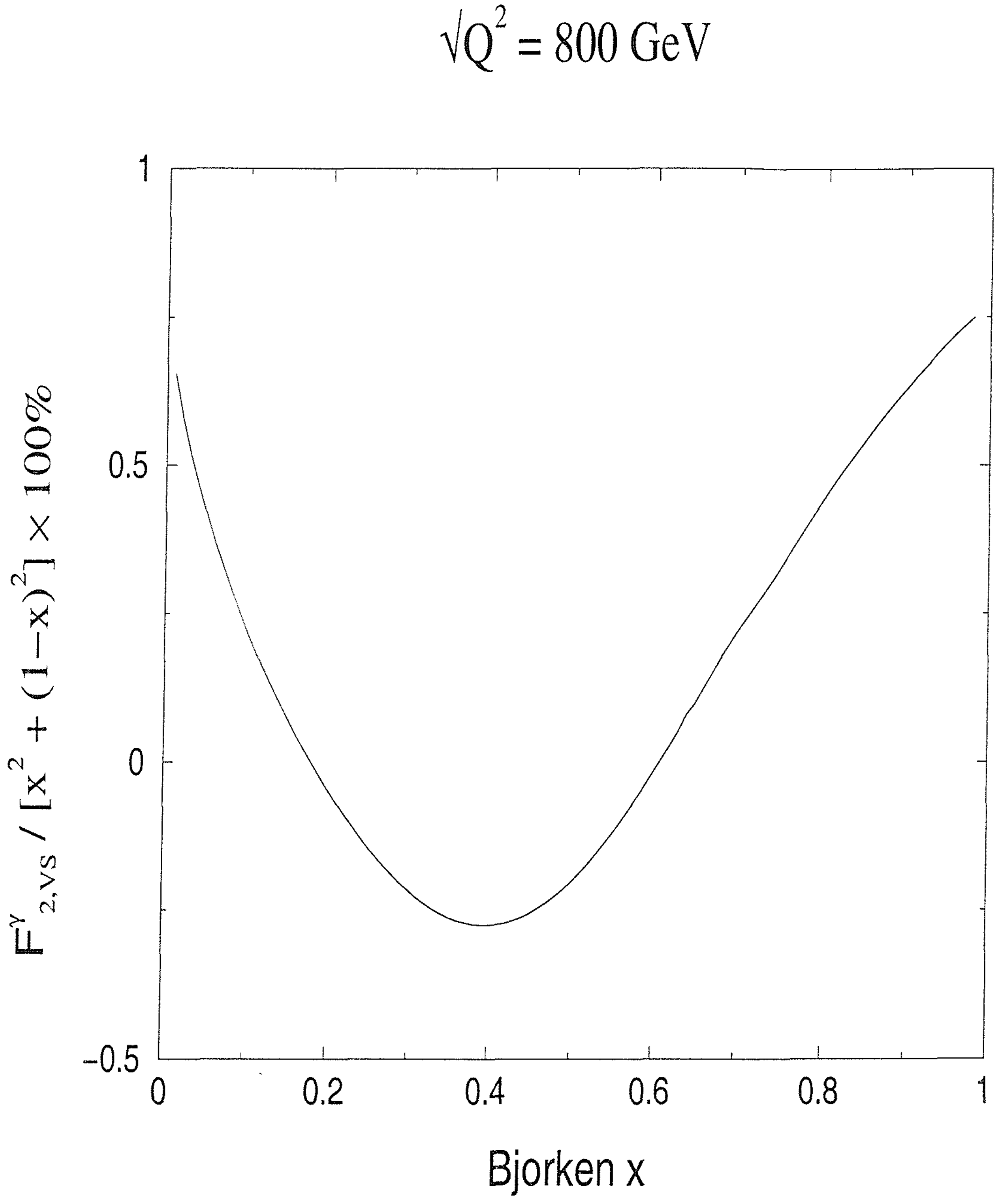

Figure 4.8: $F^{\gamma}_{2,VS}/[x^2+(1-x)^2]\times 100\%$ for $\sqrt{Q^2}=800\,GeV$ and Squark mass $M_s=300\,GeV$.

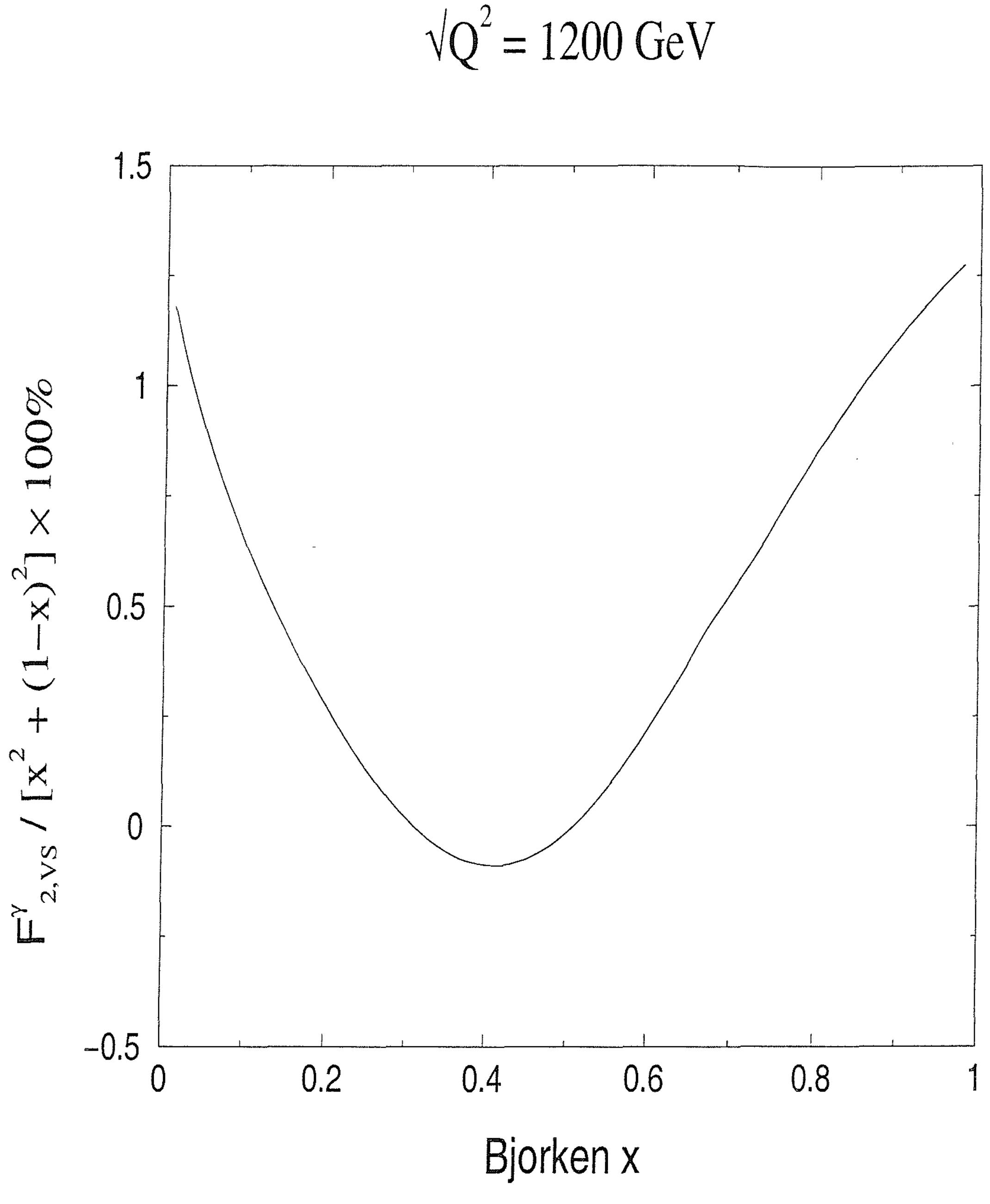

Figure 4.9: $F^{\gamma}_{2,VS}/[x^2+(1-x)^2] \times 100\%$ for $\sqrt{Q^2} = 1200\,GeV$ and Squark mass $M_s = 300\,GeV$.

Figure 4.10 shows the result of a DGLAP evolution of F_2^γ to $800\,GeV$ with a squark mass M_s of $300\,GeV$. The quantity

$$\frac{(F_2^\gamma)_{WITH} - (F_2^\gamma)_{WITHOUT}}{(F_2^\gamma)_{WITHOUT}} \times 100\%$$

has been plotted for all Bjorken x. $WITH$ and $WITHOUT$ refer to evolution with and without the virtual supersymmetric corrections. This gives a measure of the percentage change that we might expect to any evolution by including the virtual corrections. We have used the same machinery as in Chapter 3 however we have only used (LO) QCD splitting functions and no SUSY splitting functions at all. This means that the only (NLO) components in this evolution are $K^{(1)}_{T,VS}$ and $K^{(1)}_{\Sigma,VS}$ from Equations (4.7) and (4.8). This is so we can make clear any contribution due to the virtual supersymmetric corrections. The difference is less than 0.05% for any Bjorken x and is entirely negligible. The reasons for this are twofold. Firstly, as we have demonstrated above, the contributions in general are very small. Secondly, over the range of an evolution, up to about $\sqrt{Q^2} = 1\,TeV$, there will be a superposition of positive and negative contributions which will tend to cancel out. For very high $\sqrt{Q^2}$ the contribution will become positive and more significant however in this energy range there will be a much larger contribution due to tree level supersymmetric effects as we have shown in the previous Chapter.

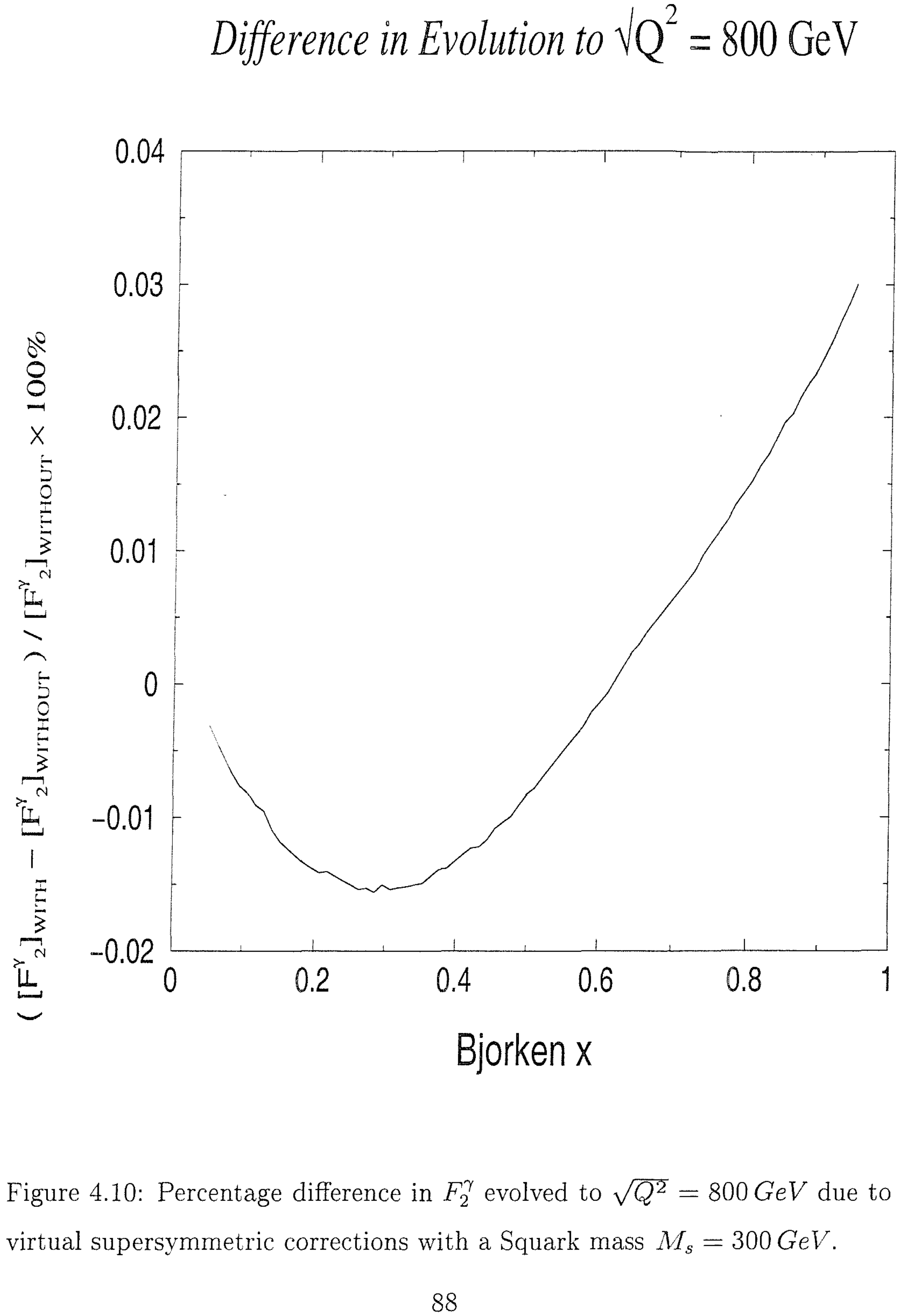

Figure 4.10: Percentage difference in F_2^γ evolved to $\sqrt{Q^2} = 800\,GeV$ due to virtual supersymmetric corrections with a Squark mass $M_s = 300\,GeV$.

In conclusion we can say that the supersymmetric virtual corrections offer a negligible contribution to the $\ln Q^2$ evolution of F_2^γ. Basically there is no noticeable resonant structure due to the virtual corrections as the squark threshold is approached. The contribution is negligible because it does not effect the evolution of F_2^γ in any appreciable way. In this respect the supersymmetric virtual corrections do not offer a measurable signal for supersymmetry below or in the region of the squark threshold.

Chapter 5

Chargino Production

5.1 Motivation

The main thrust of this dissertation is to investigate processes that could be measured in order to verify the existence of supersymmetry in nature. The previous two chapters have dealt with 'measuring' supersymmetry indirectly by evaluating its possible effects via the structure function of the photon. In this chapter we concentrate on the production of actual supersymmetric particles that could be detected in an accelerator.

Specifically we calculate the total cross section for chargino production in electron positron collisions. As mentioned previously, charginos are actually mass eigenstates corresponding to superpositions of the supersymmetric winos and higgsinos. Two distinct mass eigenstates corresponding to $\chi_1^\pm$ and

$\chi_2^{\pm}$ can occur. In principle mixing can occur between the charginos of different mass. However we assume that the centre of mass energy is sufficiently above the relevant mass thresholds so that we can treat the charginos as charged particles of a given mass. Again we are also only looking at photon photon interactions to produce the charginos. The coupling of the Z^0 to charginos is very much more complicated.

The specific interaction we are looking at is

$$e^+e^- \rightarrow e^+e^-\gamma^*\gamma^* \rightarrow e^+e^-\chi^+\chi^-$$

and the experimental setup for this interaction showing the relevant kinematic variables is shown in Figure 5.1.

A current lower limit on the chargino mass is [26]

$$\text{lightest chargino : } \chi_1^{\pm} \qquad \text{Mass m } > 67.7\, GeV$$

The point of the calculation is to see if the actual number of events corresponding to this interaction would be enough to merit looking for charginos in this experimental setup in order to verify the existence of supersymmetry.

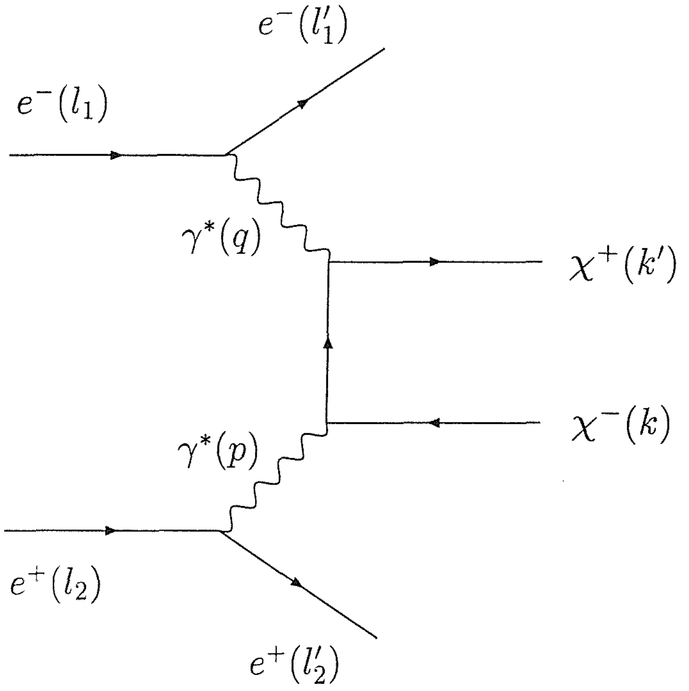

Figure 5.1: Experimental setup for the production of $\chi^+\chi^-$ in electron positron scattering showing the relevant kinematic variables.

5.2 The Calculation

The basic definition of the cross section arising from the interaction in Figure 5.1 in terms of conventional factors is

$$\mathrm{d}\sigma = \frac{1}{flux}\frac{e^4}{Q^4P^4}\frac{\mathrm{d}^4l_1'}{(2\pi)^3}\,\delta(l_1'^2)\frac{\mathrm{d}^4l_2'}{(2\pi)^3}\,\delta(l_2'^2)\,L_{\mu\nu}^{(1)}\,L^{\rho\sigma(2)}\,F_{\rho\sigma}^{\mu\nu} \tag{5.1}$$

Here we take the mass of the leptons to zero. We have factored out the kinematic contribution due to the electron and positron giving rise to the standard lepton tensors

$$\begin{aligned} L^{\mu\nu(1)} &= 2\, l_1^{\mu}\, l_1'^{\,\nu} + 2\, l_1'^{\,\mu}\, l_1^{\nu} - Q^2\, g^{\mu\nu} \\ L^{\rho\sigma(2)} &= 2\, l_2^{\rho}\, l_2'^{\,\sigma} + 2\, l_2'^{\,\rho}\, l_2^{\sigma} - P^2\, g^{\rho\sigma} \end{aligned} \tag{5.2}$$

Q^2 and P^2 are defined in Equations (1.2) and (1.4). $F^{\mu\nu}_{\rho\sigma}$ contains the internal calculation for $\gamma^*\gamma^* \to \chi^+\chi^-$.

$F^{\mu\nu}_{\rho\sigma}$ must be parameterized into four structure functions. Four rather than two since for this calculation we assume that $P^2 \neq 0$. The four structure functions F_1^1, F_1^2. F_2^1 and F_2^2 are defined as follows,

$$\begin{aligned} F^{\mu\nu}_{\rho\sigma} &= \left(g^{\mu\nu} + \frac{q^\mu q^\nu}{Q^2}\right)\left(g_{\rho\sigma} + \frac{p_\rho p_\sigma}{P^2}\right) F_1^1 \\ &- \left(g^{\mu\nu} + \frac{q^\mu q^\nu}{Q^2}\right)\left(q_\rho + \frac{p\cdot q}{P^2} p_\rho\right)\left(q_\sigma + \frac{p\cdot q}{P^2} p_\sigma\right) \frac{F_1^2}{(p\cdot q)} \\ &- \left(p^\mu + \frac{p\cdot q}{Q^2} q^\mu\right)\left(p^\nu + \frac{p\cdot q}{Q^2} q^\nu\right)\left(g_{\rho\sigma} + \frac{p_\rho p_\sigma}{P^2}\right) \frac{F_2^1}{(p\cdot q)} \\ &- \left(p^\mu + \frac{p\cdot q}{Q^2} q^\mu\right)\left(p^\nu + \frac{p\cdot q}{Q^2} q^\nu\right)\left(q_\rho + \frac{p\cdot q}{P^2} p_\rho\right)\left(q_\sigma + \frac{p\cdot q}{P^2} p_\rho\right) \frac{F_2^2}{(p\cdot q)^2} \end{aligned} \tag{5.3}$$

These structure functions are scalar functions of the kinematic variables Q^2, P^2 and Bjorken x. We need to be able to project them out from $F^{\mu\nu}_{\rho\sigma}$. Four projectors $P^{\rho\sigma}_{\mu\nu}\binom{i}{j}$ are defined such that

$$P^{\rho\sigma}_{\mu\nu}\binom{i}{j}\, F^{\mu\nu}_{\rho\sigma} \;=\; F^i_j$$

the projectors being

$$\begin{aligned} P^{\rho\sigma}_{\mu\nu}\binom{1}{1} \;&=\; \left[\frac{-g_{\mu\nu}}{2} + \frac{2rx^2}{(1-4rx^2)}\frac{p_\mu p_\nu}{P^2}\right] \\ &\times\; \left[\frac{-g^{\rho\sigma}}{2} - \frac{2rx^2}{(1-4rx^2)}\frac{q^\rho q^\sigma}{Q^2}\right] \end{aligned} \qquad (5.4)$$

$$\begin{aligned} P^{\rho\sigma}_{\mu\nu}\binom{2}{1} \;&=\; \left[\frac{-g_{\mu\nu}}{2} + \frac{2rx^2}{(1-4rx^2)}\frac{p_\mu p_\nu}{P^2}\right] \\ &\times\; \left[\frac{-rx}{(1-4rx^2)}g^{\rho\sigma} + \frac{12rx^3}{(1-4rx^2)}\frac{q^\rho q^\sigma}{Q^2}\right] \end{aligned} \qquad (5.5)$$

$$\begin{aligned} P^{\rho\sigma}_{\mu\nu}\binom{1}{2} \;&=\; \left[\frac{-x}{(1-4rx^2)}g_{\mu\nu} + \frac{12rx^3}{(1-4rx^2)}\frac{p_\mu p_\nu}{P^2}\right] \\ &\times\; \left[\frac{-g^{\rho\sigma}}{2} + \frac{2rx^2}{(1-4rx^2)}\frac{q^\rho q^\sigma}{Q^2}\right] \end{aligned} \qquad (5.6)$$

$$\begin{aligned} P^{\rho\sigma}_{\mu\nu}\binom{2}{2} \;&=\; \left[\frac{-rx}{(1-4rx^2)}g_{\mu\nu} + \frac{12r^2x^3}{(1-4rx^2)}\frac{p_\mu p_\nu}{P^2}\right] \\ &\times\; \left[\frac{-x}{(1-4rx^2)}g^{\rho\sigma} + \frac{12rx^3}{(1-4rx^2)}\frac{q^\rho q^\sigma}{Q^2}\right] \end{aligned} \qquad (5.7)$$

This means that we can do the following. Firstly, we can calculate $F^{\mu\nu}_{\rho\sigma}$, which entails using the tree level Feynman diagrams for the process $\gamma^*\gamma^* \to \chi^+\chi^-$ and integrating out the d*Lips* for this internal process. This will result in a tensor from which we can project out the structure functions F^i_j using Equations (5.4), (5.5), (5.6) and (5.7). We then have a definition of $F^{\mu\nu}_{\rho\sigma}$ in terms of the F^i_j as given by Equation (5.3) which we can contract with the lepton tensors in Equation (5.2). This contraction is required for the main cross section in Equation (5.1). It then remains to integrate out the phase space of the electron and the positron in the variables l_1' and l_2'. We shall carry out this integration using numerical Monte-Carlo techniques.

The tree level matrix elements that must be squared in order to calculate $F^{\mu\nu}_{\rho\sigma}$ are given in Figure 5.2 along with the chargino-photon vertex Feynman rule that is required.

$F^{\mu\nu}_{\rho\sigma}$ is given by,

$$F^{\mu\nu}_{\rho\sigma} = \left(\frac{B}{8\pi\eta}\int_{(1-\eta)/2}^{(1+\eta)/2} \mathrm{d}z\right)\left\{[M_1]^{\mu}_{\rho} + [M_2]^{\mu}_{\rho}\right\}^{*}\left\{[M_1]^{\nu}_{\sigma} + [M_2]^{\nu}_{\sigma}\right\} \qquad (5.8)$$

where a trace of the Dirac matrices present must be made. The first factor is the d*Lips* for massive charginos where $P^2 \neq 0$. The remaining variables are defined as

$$B = \sqrt{1 - 4m^2/S}$$

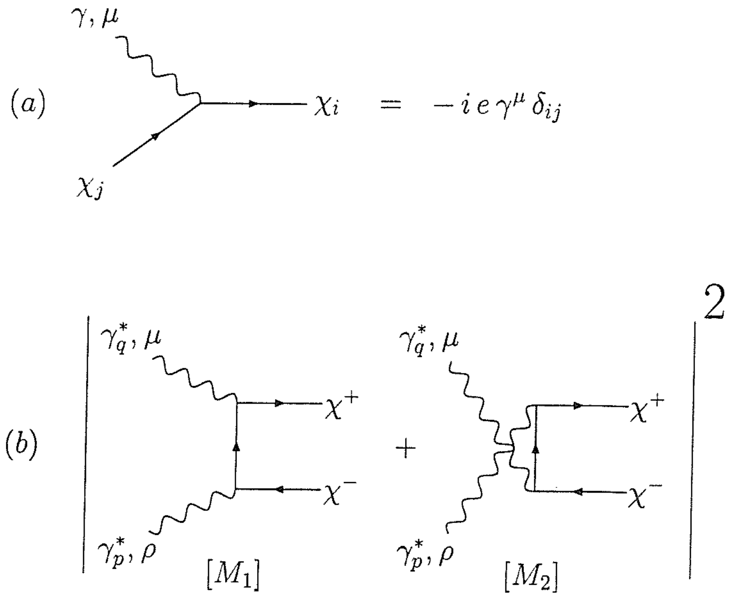

Figure 5.2: (*a*) Chargino-Photon vertex Feynman rule. (*b*) Squared matrix elements needed for tree level $\gamma^*\gamma^* \to \chi^+\chi^-$ process. We refer to these as $[M_1]$ and $[M_2]$ respectively.

$$\eta = \frac{B}{(1-2rx)}\sqrt{1-4rx^2}$$

$$S = Q^2(1-x-rx)/x$$

$$r = P^2/Q^2$$

$$z = (1-\eta\cos\theta)/2$$

where θ is the centre of mass scattering angle for the charginos.

We used the algebraic manipulation program FORM to handle the Dirac algebra and substitutions. We work in the centre of mass frame of the incoming photons. The various four-vector scalar products that appear may be substituted out for the variables Q^2, P^2, Bjorken x and the d*Lips* integration variable z. These kinematic substitutions again assume massive charginos and $P^2 \neq 0$. Having carried out the d*Lips* integrations, the projectors from Equations (5.4), (5.5), (5.6) and (5.7) are used to obtain the structure functions F_j^i as defined in Equation (5.3). By using the lepton tensors in Equation (5.2) and the parametrization of $F_{\rho\sigma}^{\mu\nu}$ in Equation (5.3) we can obtain the tensor contraction needed for the cross section.

$$\begin{aligned} L_{\mu\nu}^{(1)}\, L^{\rho\sigma(2)}\, F_{\rho\sigma}^{\mu\nu} &= 4\, P^2 Q^2 F_1^1 \\ &+ \frac{2Q^2}{(p\cdot q)} \left\{4\,(l_2\cdot q)\,(l_2'\cdot q) + P^2Q^2\right\} F_1^2 \\ &+ \frac{2P^2}{(p\cdot q)} \left\{4\,(l_1\cdot p)\,(l_1'\cdot p) + P^2Q^2\right\} F_2^1 \\ &+ \frac{1}{(p\cdot q)^2} \left\{4\,(l_1\cdot p)\,(l_1'\cdot p) + P^2Q^2\right\} \left\{4\,(l_2\cdot q)\,(l_2'\cdot q) + P^2Q^2\right\} F_2^2 \end{aligned} \tag{5.9}$$

The analytic expressions for the various F_j^i are quite lengthy and are given in Appendix E.

This contracted quantity in Equation (5.9) is now a scalar function of the kinematic variables Q^2, P^2 and Bjorken x and also of various vector products between the vectors l_1, l'_1, l_2, l'_2, q and p. Henceforth we shall refer to this as $[LLF]$ with the understanding that it is a function of these various variables. This means that the cross section in Equation (5.1) can be written as,

$$\mathrm{d}\sigma \;=\; \frac{1}{flux}\,\frac{e^4}{Q^4P^4}\,\frac{\mathrm{d}^4 l'_1}{(2\pi)^3}\,\delta({l'_1}^2)\,\frac{\mathrm{d}^4 l'_2}{(2\pi)^3}\,\delta({l'_2}^2)\,[LLF] \qquad (5.10)$$

In order to obtain the amount of actual events we might expect in an accelerator we must integrate out the phase space of the leptons in the variables l'_1 and l'_2. We make the following parameterizations of the vectors q and p.

$$q^\mu \;=\; \alpha_1\, l_1^\mu - \frac{Q^2}{S}\, l_2^\mu + \sqrt{Q^2(1-\alpha_1)}\;\underline{\hat{n}_1}^\mu \qquad (5.11)$$

$$q^\mu \;=\; -\frac{P^2}{S}\, l_1^\mu + \beta_2\, l_2^\mu + \sqrt{P^2(1-\beta_2)}\;\underline{\hat{n}_2}^\mu \qquad (5.12)$$

The quantities $\underline{\hat{n}_2}$ and $\underline{\hat{n}_2}$ are unit space vectors which 'swivel' around the centre of mass axis defined by the incoming lepton momenta l_1 and l_2. A pictorial representation of these units vectors is given in Figure 5.3. $\underline{\hat{n}_1}$ and $\underline{\hat{n}_2}$ define the angles ϕ_1 and ϕ_2 around the centre of mass axis.

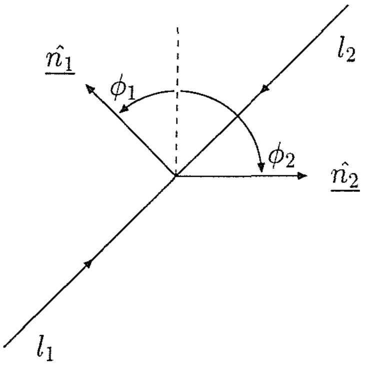

Figure 5.3: Pictorial representation of the unit space vectors n_1 and n_2.

This enables us to write the lepton phase space as

$$\frac{\mathrm{d}^4 l_1'}{(2\pi)^3}\,\delta({l_1'}^2)\frac{\mathrm{d}^4 l_2'}{(2\pi)^3}\,\delta({l_2'}^2) \;=\; \left\{\frac{1}{32\pi^3}\,\mathrm{d}\alpha_1\,\mathrm{d}Q^2\,\mathrm{d}\phi_1\right\}\left\{\frac{1}{32\pi^3}\,\mathrm{d}\beta_2\,\mathrm{d}P^2\,\mathrm{d}\phi_2\right\} \tag{5.13}$$

We may also take the sum and difference of ϕ_1 and ϕ_2

$$\phi_+ \;=\; \phi_1 + \phi_2 \;, \qquad \phi_- \;=\; \phi_1 - \phi_2$$

and integrate out ϕ_+ since none of the required scalar products between the vectors depend on ϕ_+.

The kinematic limits on these integration variables are given in terms of the total invariant centre of mass squared, $S_{tot} = (l_1 + l_2)^2$.

$$
\begin{aligned}
\frac{Q^2}{S_{tot}} \;\leq\; &\alpha_1 \;\leq\; 1 \\
\frac{P^2}{S_{tot}} \;\leq\; &\beta_2 \;\leq\; 1 \\
0 \;\leq\; &Q^2 \;\leq\; S_{tot} \\
0 \;\leq\; &P^2 \;\leq\; S_{tot} \\
0 \;\leq\; &\phi_- \;\leq\; 2\pi
\end{aligned}
\tag{5.14}
$$

The *flux* is given by $2S_{tot}$. This leaves us with a quantity for the cross section that we can work with,

$$
\mathrm{d}\sigma \;=\; \frac{1}{2S_{tot}}\,\frac{e^4}{Q^4P^4}\,[LLF]\,\frac{1}{(512\pi^5)}\,\mathrm{d}\alpha_1\,\mathrm{d}\beta_2\,\mathrm{d}Q^2\,\mathrm{d}P^2\,\mathrm{d}\phi_- \tag{5.15}
$$

5.3 The Monte-Carlo Integration

The required integral, Equation (5.15), that we have to perform is too complicated to be done analytically. We choose to perform a Monte-Carlo type integration in the five variables over the ranges given in Equation (5.14). Hereafter whenever we write S we are referring to S_{tot} given in the previous section.

$$\int_0^S \mathrm{d}Q^2 \int_0^S \mathrm{d}P^2 \int_{Q^2/S}^1 \mathrm{d}\alpha_1 \int_{P^2/S}^1 \mathrm{d}\beta_2 \int_0^{2\pi} \mathrm{d}\phi_-$$

We have an analytic expression for the integrand given in Equation (5.15). The procedure is to sample the integrand N times. For each sample we obtain five random numbers in the range $0 \leq x_i \leq 1$. From these x_i we obtain a set of randomly generated integration variables within the required range. We can also define set of r_i for each set of x_i in order to make the algebra more manageable. The relationship between the x_i, the r_i and the set of randomly generated integration variables is given as

$$\begin{array}{rclcl} \phi_- & = & 2\pi x_1 & = & 2\pi r_1 \\ Q^2 & = & S x_2 & = & S r_2 \\ P^2 & = & S x_3 & = & S r_3 \\ \alpha_1 & = & Q^2/S + (1 - Q^2/S)\, x_4 & = & r_2 + (1 - r_2)\, r_4 \\ \beta_2 & = & P^2/S + (1 - P^2/S)\, x_5 & = & r_3 + (1 - r_3)\, r_5 \end{array} \tag{5.16}$$

Now in the centre of mass frame of the leptons we can show that

$$l_1 \cdot l_1' = \frac{S}{2}\left(1 - \alpha_1 + \frac{Q^2}{S}\right)\frac{(1 - \cos\theta_1)}{2} = \frac{Q^2}{2} \tag{5.17}$$

$$l_2 \cdot l_2' = \frac{S}{2}\left(1 - \beta_2 + \frac{P^2}{S}\right)\frac{(1 - \cos\theta_2)}{2} = \frac{P^2}{2} \tag{5.18}$$

where θ_1 and θ_2 are the scattering angles of lepton l_1 and lepton l_2 respectively. Thus given a random set of integration variables from Equation (5.16) we can calculate the two scattering angles that this set belongs to. These angles are given by

$$\theta_1 = \cos^{-1}\left\{1 - \frac{2Q^2}{S(1-\alpha_1+Q^2/S)}\right\} \tag{5.19}$$

$$\theta_2 = \cos^{-1}\left\{1 - \frac{2P^2}{S(1-\beta_2+P^2/S)}\right\} \tag{5.20}$$

We can therefore divide each of θ_1 and θ_2 into a number of bins into which the cross section can fall. Into each bin we add the value

$$\frac{1}{2S}\frac{1}{(512\pi^5)}\frac{e^4}{Q^4P^4}[LLF]\frac{[2\pi\times S\times S\times(1-Q^2/S)\times(1-P^2/S)]}{N}$$

and keep a separate cumulative total of these values which will give the total cross section. The factor $[2\pi\times S\times S\times(1-Q^2/S)\times(1-P^2/S)]$ comes from the standard Jacobian transformation required to enable Monte-Carlo sampling. The factor of N is required because we are using N samples.

It is possible to further simplify the quantity that goes into each bin by factoring out certain dimensional quantities. Also it is more convenient to have a dimensionless quantity within the mechanics of the computer program used to carry out the integration. Given this simplification procedure we obtain the following quantity

$$d\sigma = \frac{e^8}{128\pi^5 S}\left\{\frac{(1-r_2)(1-r_3)}{r_2^2\,r_3^2}\right\}\frac{1}{N}\left[\frac{[LLF]}{4\,S^2(e^4/\pi)}\right] \tag{5.21}$$

There are two constraints that we must build into the integration. Firstly there must be enough energy to create particles. The internal photon photon invariant centre of mass squared $(q+p)^2$ must be sufficiently large to produce charginos of mass M_χ. This constraint

$$(q+p)^2 \; \geq \; 4\, M_\chi^2$$

translated into the variables that we have defined is

$$\alpha_1 \beta_2 + \sqrt{4 r_2 r_3 (1-\alpha_1)(1-\beta_2)} \; \geq \; r_2 + r_3 + 4 M_\chi^2 / S \qquad (5.22)$$

If this constraint is not met then we can't have an event and zero is entered into the relevant Monte-Carlo bin.

Secondly we must take account of the inherent singularities produced by either of the photons becoming on-shell. Equations (5.1), (5.15) and (5.21) all show that the differential cross section is proportional to $1/(Q^4 P^4)$ or equivalently $1/(r_2^2 r_3^2)$. This means that if either Q^2 or P^2 become very small there is a singularity. $Q^2 = 0$ or $P^2 = 0$ corresponds to either photon becoming on-shell or real. In actual fact the singularity is only proportional to $1/(Q^2 P^2)$. This is because the quantity $[LLF]$ goes to zero like $Q^2 P^2$, hence we have an overall divergence proportional to $1/(Q^2 P^2)$ or $1/(r_2 r_3)$. We can also see from Equations (5.19) and (5.20) that $Q^2 \rightarrow 0$ or $P^2 \rightarrow 0$ will produce leptons in the forward direction, i.e. $\theta_1 \rightarrow 0$ or $\theta_2 \rightarrow 0$. This is a real singularity and is present in the equations. However it is impossible to detect particles directly down the beam axis in an accelerator. In essence one would have to tag one of the leptons after it had been scattered down the beam axis with $\theta \to 0$. Since this type of detection is impossible and it leads to singularities anyway we introduce an angular cut-off. This is a 'small' angle away from the beam axis that produces a cone around the beam axis. If for any particular sample, either of the variables θ_1 or θ_2 given by Equations (5.19) and (5.20), is less than this angular cut-off then the event is discounted and not added to the cross section. In practise these angular cut-offs tend to be of the order of milliradians up to about 100 milliradians.

We need to convert cross section quantities into actual numbers of events. Equation (5.21) is dimensionless apart from the $1/S$ factor. Since we are envisaging the next generation of high energy linear electron positron colliders, it is not unreasonable to assume a centre of mass energy corresponding to $S = 1\,TeV^2$. The factor that we need to multiply by corresponds to

$$(\sigma \to \text{Events}) \;=\; [\text{Luminosity}] \times \frac{(hc/2\pi)^2}{(TeV)^2 e^2} \frac{1}{(pb\,per\,m^2)}$$

[Luminosity] refers to the Integrated Luminosity measured in inverse picobarns (pb^{-1}). This is a function of the flux of the experimental beam and also the period of time over which measurements are made using the beam. We might reasonably expect a luminosity of $5000pb^{-1}$. $(hc/2\pi)^2$ accounts for the practise in Quantum Field Theory of naturalising these quantities to unity for simplicity. $1/TeV^2$ allows for our choice of the TeV as our unit of energy. $1/e^2$ converts from electron-volts to Joules. $1/(pb\,per\,m^2)$ allows for the fact that theorists measure cross sections in m^{-2} and we require this to be in picobarns since experimental luminosities are given in inverse picobarns.

Taking all these factors into account we obtain a cross section to events multiplier of

$$\begin{aligned}(\sigma \to \text{Events}) &= [5000] \times \frac{(3.1616 \times 10^{-26})^2}{(10^{12})^2(1.6021 \times 10^{-19})^2} \frac{1}{(10^{-40})} \\ &= 5000 \times 389.39\end{aligned} \tag{5.23}$$

5.4 Results

The final equation that we use in order to calculate the amount of events we might expect for chargino production in an electron positron collider is

$$5000 \times 389.39 \times \frac{e^8}{128\pi^5 S}\left\{\frac{(1-r_2)(1-r_3)}{r_2^2\, r_3^2}\right\}\frac{1}{N}\left[\frac{[LLF](r_1, r_2, r_3, r_4, r_5, M_\chi)}{4\, S^2(e^4/\pi)}\right] \tag{5.24}$$

As explained in the previous section this quantity is evaluated N times with the set of random variables given in Equation (5.16). In practise we took 10^9 Monte-Carlo samples. There was a check that we used to ensure confidence in the results that were produced. As we ran through the N samples we calculated the total amount of events as well as the amount that went into each bin. Finally we compared the total amount events with the sum of the events in each bin. If N was taken too high then these quantities would disagree. This was expected and is due to rounding errors in the internal workings of the computer processor. At $N = 10^9$ the agreement was to four significant figures. Since the calculation was a Monte-Carlo one, we did not produce the same answer with each run. The variance in results was greater if the value for N was lower. The maximum variance in the total amount of events was about 10% with $N = 10^9$. Without going into exhaustive Monte-Carlo error analysis we took $N = 10^9$ as being a satisfactory number of samples to produce a reasonable answer. The reasoning behind this is that if N is smaller a wider variance in events is produced and if N is larger then rounding errors start to effect the result.

Figures 5.4 and 5.5 show the results for chargino masses of $100\,GeV$ and $65\,GeV$ respectively. These two masses correspond to currently accepted probable higher and lower limits for the chargino mass. We took 18 equal bins in which to divide up the 180^o into which the incoming electron and positron can scatter. This corresponds to tagging the leptons in 10^o segments away from the beam axis. Having calculated the amount of events expected in each of the bins we used two ways of analysing the results.

Firstly we calculated the total amount of events. As discussed in the last section, events within the angular cut-off, 10 milliradians or 0.6^o, are discounted since the scattered leptons cannot be tagged. As would be expected there are more events for the lower chargino mass of $65\,GeV$. Less energy is required to produce charginos of lower mass. This means that given the same centre of mass beam energy more kinematic configurations correspond to the production condition in Equation (5.22). There are 55.82 events in total for a chargino of mass $M_\chi = 65\,GeV$ against 16.41 for a chargino of mass $M_\chi = 100\,GeV$. We conclude that there are roughly 250% more events in total for the lighter chargino mass.

Secondly we concentrated on the angular dependence of the results. Figures 5.4 and 5.5 show two measures of this angular dependence.

As a first measure of angular dependence we take a value of θ away from the beam axis in order to construct a cone around the beam axis. A certain amount of bins will fall into this cone. We take two such cones with the same value of θ but pointing in opposite directions, one for the electron and one for the positron. We can say how many events will fall inside this 'double cone'. The quantity 'Events in Double Cone' gives the percentage of total events that fall inside these two cones for 10^o, 20^o, 30^o etc... For example, referring to Figure 5.4, we can say that 85.42% of events fall within the 40^o 'double cone' for production of charginos with mass $M_\chi = 100\,GeV$. This means that 85.42% of events will occur for configurations where both the electron and the positron are tagged within 40^o of the beam axis. It is clear that the vast majority of events fall in the forward direction, i.e. where both the electron and the positron are only scattered through a small angle relative to the beam axis. Despite the difference in the total number of events, the percentages for both chargino masses are very similar. A consistent trend that came out of all samples is that the $M_\chi = 65\,GeV$ charginos are very slightly more packed into the more forward bins than the $M_\chi = 100\,GeV$ charginos. For example we can see that 83.88% of the $M_\chi = 65\,GeV$ charginos are packed into the first 30^o against 77.53% of the $M_\chi = 100\,GeV$ charginos. This difference is even more marked in just the first bin where there is almost a 10% difference.

As a second measure of angular dependence we have concentrated on just one of the leptons. In Figures 5.4 and 5.5, 'Percentage of Events in θ_1 Bin' gives the percentage of the total number of events that fall into each of the 10^o bins for just one of the leptons. The calculation is symmetric between the incoming electron and the incoming positron, so it makes no difference that we have picked θ_1 rather than θ_2. For example, the second quantity of 17% in Figure 5.4 between 10^o and 20^o refers to the percentage of the total amount of events that correspond to one of the leptons being tagged in the second bin. The other lepton may be tagged at any angle although this will be more likely to be in the forward direction also. Again it is apparent that the vast majority of events fall in the forward direction with over 60% of events falling in the first bin for either chargino mass, i.e. under 10^o from the beam axis. Again we can see that the $M_\chi = 65\,GeV$ charginos are very slightly more packed in the first three bins. The sum of the first three bars for the lighter chargino is 93.5% against 90.5% for the heavier chargino. Indeed there is a 7.5% difference if we just take the first bin. This again was a consistent result over many different samplings. We have only given results for the first ten bins up to 100^o since thereafter the values are negligible at under 1%.

We carried out simulations for a higher centre of mass energy $S = 1.5\,TeV^2$, which is inside the possible higher energy limit for the next generation of linear colliders. One would expect some increase in the amount of events, however our results showed no appreciable difference from $S = 1\,TeV^2$, so we have omitted them.

The reason that most of the events fall in the forward direction has been alluded to in the previous section while discussing the need for an angular cut-off. As was explained, the cross section given in Equation (5.1) has an overall divergence proportional to $1/(Q^2P^2)$. This means that the greatest contribution to the cross section will occur when $Q^2 \rightarrow 0$ and $P^2 \rightarrow 0$. However from equations (5.19) and (5.20), this case corresponds to $\theta_1 \rightarrow 0$ and $\theta_2 \rightarrow 0$.

In conclusion we may say that given an accelerator with a centre of mass energy $S \simeq 1\,TeV^2$, it would be definitely feasible to look for chargino production in electron positron collisions. It is clear from our results that increasing the beam energy above $1\,TeV^2$ will not make an appreciable difference. However what is far more important is the amount of events that can be tagged close to the beam axis. We used an angular cut-off of 10 milliradians or 0.6^o. If however this cut-off had to be experimentally increased to 175 milliradians or 10^o then the amount of events that could be measured would be reduced drastically. From Figures 5.4 and 5.5 we can see that between 40% and 50% of the total amount of events would be lost, more in the case of a lighter chargino since the events are packed slightly closer to the beam axis as discussed above. So in effect the precision of being able to measure close to the beam axis is as important as reaching a high centre of mass energy. Very much also depends on what the actual mass of the chargino is. The amount of events is reduced by around 71% if the chargino mass increases from $65\,GeV$ to $100\,GeV$. It must be bourne in mind that the actual efficiency of detection of charginos in the accelerator would be less than 100% due to backgrounds.

The chargino has a few characteristic decay modes that would actually be seen in the accelerator,

$$\chi^{\pm} \to \chi^0 \, W^{\pm} \to \chi^0 \, l^{\pm} \, \nu$$

$$\chi^{\pm} \to \chi^0 \, W^{\pm} \to \chi^0 \, q \, \bar{q}$$

$$\chi^{\pm} \to \nu \, \tilde{l}^{\pm} \to \nu \, l^{\pm} \, \chi^0$$

$$\chi^{\pm} \to \bar{q} \, \tilde{q} \to \bar{q} \, q \, \chi^0$$

$$\chi^{\pm} \to \bar{q} \, \tilde{q} \to \bar{q} \, q \, \tilde{g}$$

where χ^0 is any neutralino, l is a lepton, $\tilde{q}$ is a squark and $\tilde{g}$ is a gluino. The relative rates of these decay modes depend on supersymmetric masses in general and also the mixing coefficients that determine the mass eigenstates.

Total Events $=$ 16.41

$S = 1.0\,TeV^{-2}$

$M_\chi = 100\,GeV$

Cut-Off $=$ 10 $mRad$

Samples $=$ 10^9

Events in Double Cone

10^o	40.30%
20^o	64.42%
30^o	77.53%
40^o	85.42%
50^o	90.24%
60^o	93.41%
70^o	95.50%
80^o	96.95%
90^o	97.96%
100^o	98.65%
110^o	99.12%
120^o	99.43%
130^o	99.65%
140^o	99.80%
150^o	99.90%
160^o	99.96%
170^o	99.99%
180^o	100.0%

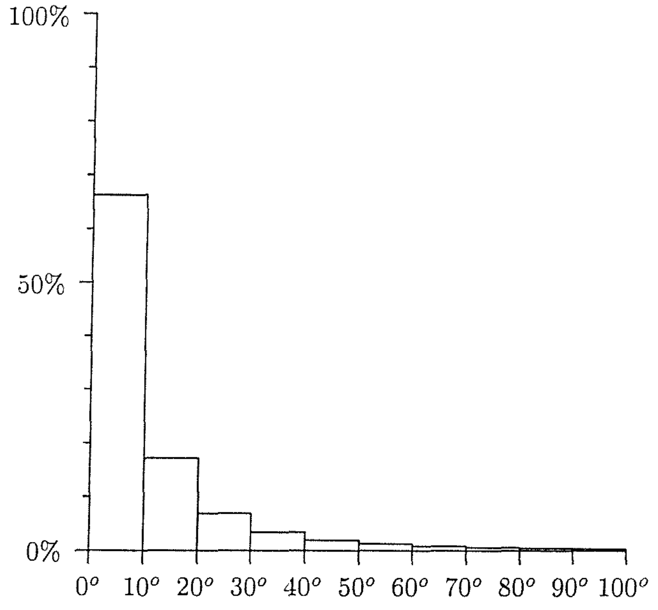

Percentage of Events in θ_1 Bin

Figure 5.4: Monte-Carlo results for Chargino production of Mass $M_\chi = 100\,GeV$.

Total Events $=$ 55.82

$S = 1.0\,TeV^{-2}$

$M_\chi = 65\,GeV$

Cut-Off $= 10\,mRad$

Samples $= 10^9$

Events in Double Cone

10°	49.20%
20°	72.37%
30°	83.88%
40°	89.95%
50°	93.44%
60°	95.67%
70°	97.10%
80°	98.05%
90°	98.67%
100°	99.14%
110°	99.43%
120°	99.64%
130°	99.77%
140°	99.88%
150°	99.94%
160°	99.98%
170°	99.99%
180°	100.0%

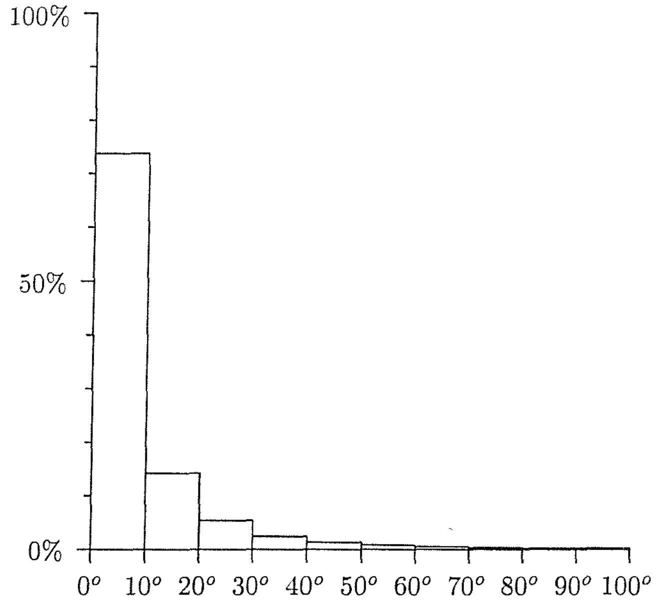

Percentage of Events in θ_1 Bin

Figure 5.5: Monte-Carlo results for Chargino production of Mass $M_\chi = 65\,GeV$.

Chapter 6

Summary

The title of this thesis is 'Signals for Supersymmetry in Photon Photon Scattering'. We have investigated three areas where the effects of supersymmetry might be 'measurable' in a particle accelerator. The type of processes discussed are particularly relevant for the proposed next generation of high energy linear electron positron colliders which should reach centre of mass energies of between $500\,GeV$ and $1.5\,TeV$.

Photon photon scattering is a core process involved in electron positron collisions and results in a measurable quantity called the photon structure function F_2^γ. In the first two Chapters we introduced the theoretical framework for analysing F_2^γ in the arena of supersymmetric effects. In Chapter 3 we showed that there is a significant contribution to F_2^γ due to supersymmetry. The effect is primarily due to the squark as the difference due to changing the gluino mass is negligible. In practise the 'target' photon is not likely to be on-shell and the increased virtuality of this photon diminishes the effect but only modestly. F_2^γ therefore offers a good way of either vindicating supersymmetry or measuring its effects above the SUSY threshold.

In Chapter 4 we calculated the virtual supersymmetric contribution to the evolution of F_2^γ. This would be a useful effect to measure as it would be relevant below the actual SUSY threshold. However this contribution exhibits a negligible effect on the evolution of F_2^γ and is hence of no use as a signal for supersymmetry.

In Chapter 5 we calculated the actual amount of events that one might expect for chargino production in an electron positron collider. There seems to be a significant number of events. However the usefulness of such a signal for supersymmetry depends on many experimental factors. The integrated luminosity, the beam axis angular cut-off and the actual mass of the chargino are all factors in determining how many events one could expect. However if the mass isn't too high and the angular precision of measurement is good enough then detecting charginos offers a good indicator for supersymmetry.

In short we expect accelerators of the requisite energy to be functioning during the next decade. If supersymmetry does indeed exist in nature then much work will definitely go into the measurement of F_2^γ and possibly into detecting charginos also.

Appendix A

C++ Program

A.1 Preamble

In this appendix we give some consideration to the programming procedures and difficulties encountered in the numerical application of the DGLAP equations. The task was to produce a reliable and flexible program that would accept parameterizations of parton distribution functions at some energy and numerically evolve them through various thresholds and finally calculate F_2^γ at some higher energy. The basic program was used extensively in the work discussed in Chapters 3 and 4. The program that was used for the work in Chapter 5 to calculate the total cross section for chargino production involved a Monte Carlo evaluation of the multi-dimensional phase space integral. This was was far less involved and does not merit any detailed explanation in an appendix.

We used C++ rather than Fortran to write the evolution program. This meant that we could use classes to represent objects that appear in the DGLAP framework in a very general way. The initial task of creating these abstract classes was perhaps difficult and time consuming. However once they had been tested it was much easier to generalise the application of the program in the sense of varying parameters, introducing further complexities and generally 'tweaking' the program. Actually most of the code resided in the 'class' section of the program meaning that the 'main' portion of the code which was changed regularly was actually quite small. Having had experience of Fortran we feel that the task of implementing the DGLAP equations accurately and reliably was in the end made very much easier by using C++.

There are two main processes that need to be implemented, the convolution integral and the 'stepped' numerical solution of differential equations. We divide the rest of this appendix accordingly.

A.2 The convolution

The convolution integral is given in Equation (1.23),

$$P_{ij}^{(k)} \otimes F_j \equiv \int_x^1 \frac{dy}{y} P_{ij}^{(k)} \left(\frac{x}{y}\right) F_j(y, Q^2)$$

and is defined between a splitting function $P_{ij}^{(k)}$ and a distribution $F_j(x, Q^2)$.

As we solve the differential equations that form the DGLAP framework, at any particular Q^2 we must perform many convolutions between different splitting functions and different distributions as in Equations (1.24) and (1.25) for instance. The range of the dummy integration variable y in these convolutions is given by,

$$0 < x \leq y \leq 1$$

which means that we must sample all distributions in this range.

We created a class called Xrange which contained all the information about this sampling. Since there were inherent divergences that appear when one moves from an analytical to a numerical framework we could never evaluate integrands at $x = 0$, $y = x$ or $y = 1$. This Xrange class used a lower limit a just above zero, a higher limit b just below 1 and split the range into N steps. All other classes were defined in terms of this class which only had to be fixed once at the beginning of any particular program run.

A general PDF class was created to model parton distribution functions. As a function of x, each PDF would have numerical values at particular values of x determined by the Xrange class, also at a particular Q^2. The object orientated nature of C++ meant that these PDFs were very easy to manipulate. The mathematical operators $+$, $-$, $\times$ and $\div$ were overloaded in the implementation so that operations like addition, scalar multiplication, etc... could be performed very easily on PDFs. The $+$ and $-$ operators were overloaded so that PDFs could be added and subtracted. The $\times$ and $\div$ operators were overloaded so that scalar multiplication and division could be performed with PDFs. If you imagine that each distribution might contain hundreds of discrete values then the operation,

$$T_{35}(x,Q^2) = 2\left[u(x,Q^2)+d(x,Q^2)+s(x,Q^2)+c(x,Q^2)+b(x,Q^2)-5t(x,Q^2)\right]$$

becomes as easy to perform as it is written above. If one was dealing with many arrays and loops as one might be in Fortran the above operation might take a page of code. All the arrays, loops and operations are written down only once, inside the inner workings of the PDF class methods and once they have been tested one can be sure of not making errors by typing out many lines of code.

A general SF class was created to model splitting functions. Splitting functions are essentially analytic but can be subject to the threshold condition in Equation (3.11) for instance. There were many splitting functions involved and we found it useful to write them all out as analytical return functions in a separate file. Once an SF object had been associated with the relevant splitting functions there were two main considerations that the object orientated approach made easier. Firstly, it was possible to overload the $*$ operator so that a convolution could be performed as easily as it could be written out. For example $P_{TT}^{(0)} \otimes T_3(x,Q^2)$ defined by the convolution integral above could be written out in code as $PTT0 * T3$. All the machinery of integration was hidden inside the class methods and again once it had been tested one could be sure of not making mistakes from re-writing many lines of code. Secondly, the operation SF $\otimes$ PDF was aware of the Q^2 dependence of the PDF and how the Xrange class was sampling the integral. This meant that any threshold condition that required a run-time choice of splitting functions could be incorporated into how the integral was performed. In relation to the actual method used to numerically integrate we actually tried several different ways in an effort to reduce the error. In the end a Simpson like method that sampled the range of x in 4-steps with evaluation at 5 separate points was chosen. Some interpolation was needed towards the $x \to 1$ region however the error introduced by this was minimal.

The DGLAP equations can be written out in matrix form. For example Equations (2.6) can be written out as

$$\frac{dF_i}{d\ln Q^2} = \sum_{j=1}^{4} P_{ij} \otimes F_j + K_i \qquad \left\{ \text{for } i = 1 \to 4 \right\}$$

We created a vPDF class that was essentially a vector of PDFs. This would correspond to a column of F_i. Again the $+$, $-$, $\times$ and $\div$ operators were overloaded in order to facilitate addition, subtraction, scalar multiplication and scalar division with these vPDFs. Also we created a vSF class that was essentially a row of splitting functions. This would correspond to a row of P_{ij} for a particular i. This meant that we could overload the $*$ operator so that the operation vSF $\otimes$ vPDF could be performed. At each particular Q^2, if the K_i is turned into a vPDF the whole of the above equation can be coded as $Pij * Fj + Ki$. This again makes the implementation very simple, reliable and free from typing errors.

A.3 Differential Equations

The simplest way to numerically solve ordinary differential equations is by using Euler steps. Thus given Equation (1.24),

$$\frac{dT_l}{d\ln Q^2} = P_{TT} \otimes T_l + K_T$$

the evolution in $\ln Q^2$ is given by

$$T_l(x, \ln Q^2 + \Delta \ln Q^2) = T_l(x, \ln Q^2) + \Delta \ln Q^2 \times \left[P_{TT} \otimes T_l + K_T \right]_{x, \ln Q^2}$$

In order to produce more accuracy we can use Runge-Kutta methods. If we take a generalised DGLAP equation as

$$\frac{dF}{dt} = P \otimes F + K$$

where $t = \ln Q^2$. Then a more accurate evolution is given by

$$F(t + dt) = F(t) + \frac{dt}{6} \times (H_1 + 2H_2 + 2H_3 + H_4)$$

where

$$\begin{aligned} H_1 &= P(t) \otimes F + K(t) \\ H_2 &= P(t + dt/2) \otimes (F + H_1/2) + K(t + dt/2) \\ H_3 &= P(t + dt/2) \otimes (F + H_2/2) + K(t + dt/2) \\ H_4 &= P(t + dt) \otimes (F + H_3) + K(t + dt) \end{aligned}$$

where we must remember that each P and K is actually an expansion of individual splitting functions in the strong coupling as given in Equations

(1.21) and (1.22). In the above for example P(t+dt/2) actually means

$$P(t+dt/2) = \left(\frac{\alpha_s(t+dt/2)}{2\pi}\right)P^{(0)} + \left(\frac{\alpha_s(t+dt/2)}{2\pi}\right)^2 P^{(1)}$$

so that the coupling, which is analytic, is evaluated at three values of Q^2 corresponding to t, $t+dt/2$ and $t+dt$.

Also we must remember that the DGLAP equations are actually generalised $n \times n$ matrix equations. This means that the expressions H_1, H_2, H_3 and H_4 above give rise to up to four matrix convolutions that have to be evaluated at any particular Q^2. The algebra involved in calculating the H_i above was handled with the algebraic manipulation program FORM. The full expression involves sixty multiple convolutions that have to be evaluated in matrix form. An example is,

$$P_{ij}^{(0)} \otimes P_{jk}^{(0)} \otimes P_{kl}^{(1)} \otimes P_{lm}^{(0)} \otimes F_m$$

where the $P_{ij}^{(k)}$ are vSF splitting function rows and the F_i are vPDF parton distribution function columns.

A class called AP was designed to incorporate all these ideas. Each AP object was designed to run the distributions in a particular range, for instance from the t-quark threshold to the SUSY threshold. It would contain the relevant vPDFs, vSFs, the correct couplings and again was dependent on the Xrange class in order to determine the amount of x values that were sampled. Both the Euler method and the more involved Runge-Kutta method for numerically running the distributions was incorporated. It was a general class in the sense that it was designed to take an $n \times n$ set of DGLAP equations. Basically the distributions were evolved within the AP class and could be projected out at any desired Q^2 so that F_2^γ could be calculated from the distributions.

It turned out that using the full Runge-Kutta machinery was an 'overkill' in the sense that the evolution would take much more computer time and the end results were negligibly different from using the Euler step method. In the end we just decreased the $t = \ln Q^2$ steps and used the Euler method.

Appendix B

(NLO) Splitting Functions

In this appendix we give the (NLO) splitting functions that are used in Equations (1.24) and (1.25). The $P_{ij}^{(1)}$ were obtained from [15]. The $K_i^{(1)}$ were obtained from [12] and [13].

Given that

$$S_2(x) \;=\; -2\,\mathrm{Li}_2(-x) + \frac{1}{2}\ln^2 x - 2\ln x \ln(1+x) - \frac{\pi^2}{6} \tag{B.1}$$

where $\mathrm{Li}_2(x)$ is the dilog function

$$\mathrm{Li}_2(x) \;=\; \sum_{i=1}^{\infty} \frac{x^n}{n^2} \tag{B.2}$$

that $\zeta(n)$ is the Riemann zeta function,

$$\zeta(n) = \sum_{i=1}^{\infty} \frac{1}{i^n} \tag{B.3}$$

and that the 'plus' prescription, $(1-x)_+$, is understood as,

$$\int_0^1 dx \, \frac{f(x)}{(1-x)_+} = \int_0^1 dx \, \frac{f(x)-f(1)}{1-x}$$

the (NLO) splitting functions are,

$$\begin{aligned}
P_{TT}^{(1)}(x) = C_F^2 \Bigg\{ & - \left[2\ln x \ln(1-x) + \frac{3}{2}\ln x \right] \left(\frac{2}{(1-x)_+} - 1 - x \right) \\
& - \left(\frac{3}{2} + \frac{7}{2}x \right) \ln x - \frac{1}{2}(1+x)\ln^2 x - 5(1-x) \Bigg\} \\
+ C_F C_A \Bigg\{ & \left[\frac{1}{2}\ln^2 x + \frac{11}{6}\ln x + \frac{67}{18} - \frac{\pi^2}{6} \right] \left(\frac{2}{(1-x)_+} - 1 - x \right) \\
& + (1+x)\ln x + \frac{20}{3}(1-x) \Bigg\} \\
+ C_F T_f \Bigg\{ & - \left[\frac{2}{3}\ln x + \frac{10}{9} \right] \left(\frac{2}{(1-x)_+} - 1 - x \right) - \frac{4}{3}(1-x) \Bigg\}
\end{aligned}$$

$$+C_F\left(C_F-\frac{C_A}{2}\right)\left\{2\left(\frac{2}{1+x}-1+x\right)S_2(x)\right.$$

$$\left.+2(1+x)\ln x+4(1-x)\right\}$$

$$+\left[C_F^2\left\{\frac{3}{8}-\frac{\pi^2}{2}+6\,\zeta(3)\right\}\right.$$

$$+C_FC_A\left\{\frac{17}{24}+\frac{11\pi^2}{18}-3\,\zeta(3)\right\}$$

$$\left.-C_FT_F\left\{\frac{1}{6}+\frac{2\pi^2}{9}\right\}\right]\delta(1-x) \tag{B.4}$$

$$P^{(1)}_{\Sigma\Sigma}(x) = C_F^2\left\{-1+x+\left(\frac{1}{2}-\frac{3}{2}x\right)\ln x-\frac{1}{2}(1+x)\ln^2 x\right.$$

$$\left.-\left[\frac{3}{2}\ln x+2\ln x\ln(1-x)\right]\left(\frac{2}{(1-x)_+}-1-x\right)+2\left(\frac{2}{1+x}-1+x\right)S_2(x)\right\}$$

$$+C_FC_A\left\{\frac{14}{3}(1-x)+\left[\frac{11}{6}\ln x+\frac{1}{2}\ln^2 x+\frac{67}{18}-\frac{\pi^2}{6}\right]\left(\frac{2}{(1-x)_+}-1-x\right)\right.$$

$$
\begin{aligned}
&-\left(\frac{2}{1+x}-1+x\right)S_2(x)\Bigg\} \\
&+C_F T_f\Bigg\{-\frac{16}{3}+\frac{40}{3}x+\left(10x+\frac{16}{3}x^2+2\right)\ln x \\
&-\frac{112}{9}x^2+\frac{40}{9x}-2(1+x)\ln^2 x-\left[\frac{10}{9}+\frac{2}{3}\ln x\right]\left(\frac{2}{(1-x)_+}-1-x\right)\Bigg\} \\
&+\Bigg[C_F^2\left\{\frac{3}{8}-\frac{\pi^2}{2}+6\,\zeta(3)\right\} \\
&+C_F C_A\left\{\frac{17}{24}+\frac{11\pi^2}{18}-3\,\zeta(3)\right\} \\
&-C_F T_F\left\{\frac{1}{6}+\frac{2\pi^2}{9}\right\}\Bigg]\,\delta(1-x) \qquad \text{(B.5)}
\end{aligned}
$$

$$
\begin{aligned}
P^{(1)}_{\Sigma G}(x) \;=\; & 2fC_F T_f\Bigg\{4-9x-(1-4x)\ln x-(1-2x)\ln^2 x+4\ln(1-x) \\
&+\left[2\ln^2\left(\frac{1-x}{x}\right)-4\ln\left(\frac{1-x}{x}\right)-\frac{2}{3}\pi^2+10\right]\left(\frac{2}{(1-x)_+}-1-x\right)\Bigg\}
\end{aligned}
$$

$$+C_A T_f \left\{ \frac{182}{9} + \frac{14}{9} x + \frac{40}{9x} + \left(\frac{136}{3} x - \frac{38}{3} \right) \ln x \right.$$

$$-4 \ln(1-x) - (2+8x) \ln^2 x + 2 \left(x^2 + (1+x)^2 \right) S_2(x)$$

$$\left[- \ln^2 x + \frac{44}{3} \ln x - 2 \ln^2(1-x) + 4 \ln(1-x) \right.$$

$$\left. \left. + \frac{\pi^2}{3} - \frac{218}{9} \right] \left(x^2 + (1-x)^2 \right) \right\} \tag{B.6}$$

$$P^{(1)}_{G\Sigma}(x) \;=\; C_F^2 \left\{ -\frac{5}{2} - \frac{7x}{2} + \left(2 + \frac{7}{2} x \right) \ln x - \left(1 - \frac{1}{2} x \right) \ln^2 x \right.$$

$$\left. -2x \ln(1-x) - \left[3 \ln(1-x) + \ln^2(1-x) \right] \left(\frac{1 + (1-x)^2}{x} \right) \right\}$$

$$+ C_F C_A \left\{ \frac{28}{9} + \frac{65}{18} x + \frac{44}{9} x^2 - \left(12 + 5x + \frac{8}{3} x^2 \right) \ln x \right.$$

$$+ (4+x) \ln^2 x + 2x \ln(1-x) + S_2(x) \left(-\frac{1 + (1+x)^2}{x} \right)$$

$$+\left[\frac{1}{2}-2\ln x\ln(1-x)+\frac{1}{2}\ln^2 x+\frac{11}{3}\ln(1-x)\right.$$

$$\left.+\ln^2(1-x)-\frac{\pi^2}{6}\right]\left(\frac{1+(1-x)^2}{x}\right)\Bigg\}$$

$$+C_F T_f\left\{-\frac{4}{3}x-\left[\frac{20}{9}+\frac{4}{3}\ln(1-x)\right]\left(\frac{1+(1-x)^2}{x}\right)\right\} \qquad \text{(B.7)}$$

$$P^{(1)}_{GG}(x) \;=\; C_F T_f\Bigg\{-16+8x+\frac{20}{3}x^2+\frac{4}{3x}$$

$$-(6+10x)\ln x-(2+2x)\ln^2 x\Bigg\}$$

$$+C_F T_f\left\{2-2x+\frac{26}{9}\left(x^2-\frac{1}{x}\right)-\frac{4}{3}(1+x)\ln x-\frac{20}{9}\left(\frac{1}{(1-x)_+}+\frac{1}{x}-2+x(1-x)\right)\right\}$$

$$+C_A^2\Bigg\{\frac{27}{2}(1-x)+\frac{67}{9}\left(x^2-\frac{1}{x}\right)-\left(\frac{25}{3}-\frac{11}{3}x+\frac{44}{3}x^2\right)\ln x$$

$$+4(1+x)\ln^2 x+2\left(\frac{1}{1+x}-\frac{1}{x}-2-x(1+x)\right)S_2(x)$$

$$+\left[\frac{67}{9} - 4\ln x\ln(1-x) + \ln^2 x - \frac{\pi^2}{3}\right]\left(\frac{1}{(1-x)_+} + \frac{1}{x} - 2 + x(1-x)\right)\Bigg\}$$

$$\left[C_A^2\left\{\frac{8}{3} + 3\zeta(3)\right\} - C_F T_f - \frac{4}{3}C_A T_f\right]\delta(1-x) \tag{B.8}$$

$$K_T^{(1)}(x) \;=\; 3f\left(\langle e^4\rangle - \langle e^2\rangle^2\right)\left[k_1(x) - \frac{1}{2}k_2(x)\right] \tag{B.9}$$

$$K_\Sigma^{(1)}(x) \;=\; 3f\langle e^2\rangle\left[k_1(x) + \frac{1}{2}k_2(x)\right] \tag{B.10}$$

where

$$\begin{aligned}
k_1(x) \;=\; C_F\Bigg\{ & 4 - 9x - (1-4x)\ln x - (1-2x)\ln^2 x + 4\ln(1-x) \\
& + \Bigg[4\ln x - 4\ln x\ln(1-x) + 2\ln^2 x - 4\ln(1-x) \\
& + 2\ln^2(1-x) - \frac{2}{3}\pi^2 + 10\Bigg]\left[x + (1-x)^2\right]\Bigg\}
\end{aligned}$$

and

$$
\begin{aligned}
k_2(x) \;&=\; 2C_F\Big\{7 - 10x - \frac{\pi^2}{6}(6 - 12x + 16x^2) + (1 - 16x + 32x^2)\ln x \\
&\quad + (1 - 2x + 4x^2)\ln^2 x - (5 - 36x + 32x^2)\ln(1-x) \\
&\quad + (4 - 8x + 8x^2)\left[\ln^2(1-x) - \ln x \ln(1-x)\right] + (2 - 4x + x^2)\mathrm{Li}_2(x)\Big\}
\end{aligned}
$$

$$
\begin{aligned}
K_G^{(1)}(x) \;&=\; 3f\langle e^2\rangle 2C_F\Big\{\left[-8 + 4x + \frac{10}{3}x^2 + \frac{2}{3x} - (3+5x)\ln x - (1+x)\ln^2 x\right] \\
&\quad + \frac{2}{3x} - \frac{20}{3} + \frac{2}{3}x + \frac{16}{3}x^2 - \left(1 + 5x - \frac{4}{3}x^2\right)\ln x - (1+x)\ln^2 x \\
&\quad + \left[\frac{4}{3x} + 1 - x - \frac{4}{3}x^2\right]\ln(1-x) - 2(1+x)\left[\mathrm{Li}_2(x) - \frac{\pi^2}{6}\right]\Big\}
\end{aligned}
\tag{B.11}
$$

Appendix C

Scalar Box Calculation

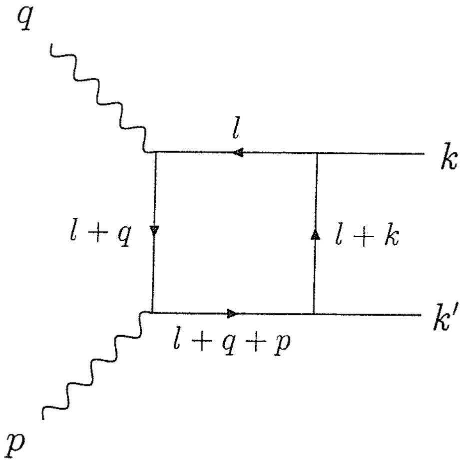

Figure C.1: Scalar Box Feynman Diagram.

The diagram shown in Figure C.1 gives rise to the following integral.

$$\int \frac{d^4l}{(2\pi)^4} \frac{1}{(l^2-m^2)((l+q)^2-m^2)((l+q+p)^2-m^2)((l+k)^2-m^2)} \tag{C.1}$$

As explained in Chapter 4 we wish to extract the part of the calculation for virtual supersymmetric corrections that is proportional to $1/\epsilon$. This corresponds to taking $t = (q-k)^2 = -Q^2/x$ whenever we need to evaluate this scalar box integral. Using Feynman parameters we can write this integral as,

$$\begin{aligned} \tilde{I} &= \frac{i}{16\pi^2} I \\ I &= \int d\alpha\, d\beta\, d\gamma\; \theta(1-\alpha-\beta-\gamma) \frac{1}{D^2} \end{aligned} \tag{C.2}$$

where,

$$D = (\beta+\gamma)^2 Q^2 - (\beta+\gamma)\gamma(S+Q^2) + S\gamma - Q^2\beta - m^2 - S(\beta+\gamma)(1-\alpha-\beta-\gamma)$$

given that,

$$\begin{aligned} Q^2 &= -q\cdot q \\ S &= (p+q)^2 \end{aligned}$$

and m is the squark mass.

D is linear in α for which we may solve.

We can then make the substitution,

$$\gamma = \rho\omega$$

$$\beta = \rho(1-\omega)$$

and solve for ω giving,

$$I = \frac{1}{S(S+Q^2)}\{J(-\Upsilon) - J(-\Psi) - J(\Phi)\} \tag{C.3}$$

where,

$$J(x) = \int_0^1 d\rho\,\frac{\ln\{1 - x\rho(1-\rho)\}}{\rho(1-\rho)} \tag{C.4}$$

and

$$\begin{aligned}\Upsilon &= Q^2/m^2\\ \Psi &= (S+Q^2)/m^2\\ \Phi &= S/m^2\end{aligned}$$

The solution for $J(x)$ depends on the range of x,

$$\begin{aligned} x &\leq -4\\ -4 < x &< 4\\ 4 \leq x& \end{aligned}$$

if $|x| < 4$

$$J(x) = -\sum_{n=1}^{\infty} \frac{x^n}{n} \frac{[(n-1)!]^2}{(2n-1)!} \tag{C.5}$$

if $x \leq -4$

$$J(x) = 2\left\{ -Li_2(1/\rho_0) + Li_2(1-\rho_0) - 2Li_2(-1) + \frac{1}{2}\ln^2(\rho_0 - 1)\right\} \tag{C.6}$$

and if $x \geq 4$

$$\begin{aligned} J(x) = & \left\{ -\frac{4}{3}\pi^2 + \ln^2\rho_0 + \ln^2(1-\rho_0) + 2Li_2(\rho_0) \right. \\ & \left. + 2Li_2(1-\rho_0) - 2i\pi\ln[\rho_0(1-\rho_0)] \right\} \end{aligned} \tag{C.7}$$

where

$$\rho_0 = \frac{1+\sqrt{1-4/x}}{2}$$

and $Li_2(x)$ is given in Equation (B.2).

The solution for I may be imaginary if $x \geq 4$. However as is made clear in Equations (4.2) and (4.3) we only need the real part of the two matrix elements that are multiplied together. This always corresponds to taking the real part of I in Equation (C.2).

Appendix D

$F_{2,VS}^{\gamma}$ for Quark Production

D.1 Explicit form for $F_{2,VS}^{\gamma}$

$$
\begin{aligned}
F_{2,VS}^{\gamma} &= \frac{8C_f\alpha_s(Q^2)}{2\pi x} \\
&\times \ \mathit{Real}\left\{A(Q^2,x,M^2)+B(Q^2,x,M^2)+C(Q^2,x,M^2)+D(Q^2,x,M^2)\right\}
\end{aligned}
$$

where $C_f = 4/3$, the squark mass is M_s and $A(Q^2,x,M^2)$, $B(Q^2,x,M^2)$, $C(Q^2,x,M^2)$ and $D(Q^2,x,M^2)$ are defined below.

In the following m^2 is the quark mass which is taken to zero or as close to zero as the Veltman-Passarino routines will allow,

$$S = Q^2(1-x)/x$$

and D_0 is given by I in Appendix C. It is the scalar box integral.

In actual fact the functions $A(Q^2, x, M^2)$, $B(Q^2, x, M^2)$, $C(Q^2, x, M^2)$ and $D(Q^2, x, M^2)$ above are the contributions arising from diagrams (c), (d), (e) and (f) of Figure 4.2 respectively. These contributions allow for crossed incoming photon lines and both left and right handed squarks.

The Veltman-Passarino functions B_i and C_{ij} are standard functions which may be found in [23].

$$A(Q^2, x, M^2) = \frac{1}{4} x^2 (x-1) \left[Z_1 - Z_2 + Z_3 - Z_4 \right]$$

$$\begin{aligned} Z_1 &= B_0(0, M^2, M^2) \\ Z_2 &= B_0(-Q^2/x, M^2, M^2) \\ Z_3 &= B_1(0, M^2, M^2) \\ Z_4 &= B_1(-Q^2/x, M^2, M^2) \end{aligned}$$

$$B(Q^2, x, M^2) = \frac{1}{2} \left\{ (2x^3 - 2x^2 + x) Z_1 + (-x^3 + x^2 - x) Z_2 + (-x^3 + x^2) Z_3 \right\}$$

$$
\begin{aligned}
Z_1 &= C_{24}(m^2, 0, 0, M^2, M^2, M^2) \\
Z_2 &= C_{24}(0, 0, -Q^2, M^2, M^2, M^2) \\
Z_3 &= C_{24}(0, -Q^2/x, -Q^2, M^2, M^2, M^2)
\end{aligned}
$$

$$
C(Q^2, x, M^2) = \frac{Q^2 x(x-1)}{4}\,(Z_2 - Z_1) + \frac{x^2(x-1)}{2}\,(Z_3 - Z_4)
$$

$$
\begin{aligned}
Z_1 &= C_{22}(0, -Q^2/x, 0, M^2, M^2, M^2) \\
Z_2 &= C_{23}(0, -Q^2/x, 0, M^2, M^2, M^2) \\
Z_3 &= C_{24}(0, -Q^2/x, 0, M^2, M^2, M^2) \\
Z_4 &= C_{24}(m^2, 0, 0, M^2, M^2, M^2)
\end{aligned}
$$

$$
D(Q^2, x, M^2) = \frac{1}{8}\Big\{ (6x^2M^2/Q^2 - 6x^2 - 2x)Z_1 + (-6x^3 + 10x^2 - 4x)Z_2
$$

$$
+ (-9x^3 + 10x^2 - 2x)Z_3 + (6x^3 - 18x^2 + 4x)Z_4 + (9x^3 - 6x^2M^2/Q^2 - 8x^2)Z_5 + (-2x)Z_6
$$

$$+ (12x^3 - 8x^2 - 4x)Z_7 + (-2x^2)Z_8 \; + \; (-12x^3 - 12x^2 + 2x)Z_9 \; + \; (6x^2 - 6x)Z_{10}$$

$$+ (-4x^2+4x-2)Q^2 Z_{11} + (6x^2 Q^2)Z_{12} + (-6x^2+6x)Q^2 Z_{13} + (-2x+2)Q^2 Z_{14}$$

$$+ (-2Q^2)Z_{15} + (-2x+2)Q^2 Z_{16} + (4xQ^2)Z_{17} + (-6x^2+6x)Q^2 Z_{18} + (4x^2-4x)Z_{19}$$

$$+ (12x^2)Z_{20} \; + \; (2xM^2 - Q^2)Z_{21} \; + \; (-6x^2 + 13x - 5)Q^2 Z_{22} \; + \; (9x^2 Q^2)Z_{23}$$

$$+ (6x^3-12x^2+7x-1)Q^2 Z_{24} + (6x^3-15x^2+9x)Q^2 Z_{25} + (-3x^2Q^2+2xQ^2+2xM^2)Z_{26}$$

$$- \; (x+1)Q^2 Z_{27} \; + \; (-6x^3 + 12x^2 - 7x + 1)Q^2 Z_{28} \; + \; (3x^2 - 3x)Q^2 Z_{29}$$

$$+ (3x^2Q^2-2x^2M^2-4xQ^2+3xM^2)Z_{30} + (-8x^2Q^2+4x^2M^2+12xQ^2-2xM^2-4Q^2)Z_{31}$$

$$+ (3x^2Q^2 - x^2M^2)Z_{32} \; + \; (-3x^3Q^2 + 7x^2Q^2 - x^2M^2 - 5xQ^2 + xM^2 + Q^2)Z_{33}$$

$$+ \; (9x^3 - 16x^2 + 8x - 1)Q^2 Z_{34}$$

$$+ (3x^2Q^4-2x^2Q^2M^2-7xQ^4+3xQ^2M^2-Q^4/x+5Q^4-Q^2M^2)D_0(Q^2,x,M^2)\Big\}$$

$$
\begin{aligned}
Z_1 &= B_0(0,M^2,M^2)\\
Z_2 &= B_0(S,M^2,M^2)\\
Z_3 &= B_0(-Q^2/x,M^2,M^2)\\
Z_4 &= B_0(-Q^2,M^2,M^2)\\
Z_5 &= B_0(0,M^2,M^2)\\
Z_6 &= B_1(0,M^2,M^2)\\
Z_7 &= B_1(S,M^2,M^2)\\
Z_8 &= B_1(-Q^2/x,M^2,M^2)\\
Z_9 &= B_1(-Q^2,M^2,M^2)\\
Z_{10} &= B_1(0,M^2,M^2)\\
Z_{11} &= C_{21}(-Q^2,0,S,M^2,M^2,M^2)\\
Z_{12} &= C_{21}(-Q^2,0,0,M^2,M^2,M^2)\\
Z_{13} &= C_{21}(0,0,S,M^2,M^2,M^2)\\
Z_{14} &= C_{22}(0,0,-Q^2/x,M^2,M^2,M^2)\\
Z_{15} &= C_{22}(-Q^2,0,S,M^2,M^2,M^2)\\
Z_{16} &= C_{23}(0,0,-Q^2/x,M^2,M^2,M^2)\\
Z_{17} &= C_{23}(-Q^2,0,S,M^2,M^2,M^2)\\
Z_{18} &= C_{23}(0,0,S,M^2,M^2,M^2)
\end{aligned}
$$

$$
\begin{aligned}
Z_{19} &= C_{24}(0,0,-Q^2/x, M^2, M^2, M^2) \\
Z_{20} &= C_{24}(0,0,S, M^2, M^2, M^2) \\
Z_{21} &= C_{11}(0,0,-Q^2/x, M^2, M^2, M^2) \\
Z_{22} &= C_{11}(-Q^2, 0, S, M^2, M^2, M^2) \\
Z_{23} &= C_{11}(-Q^2, 0, 0, M^2, M^2, M^2) \\
Z_{24} &= C_{11}(-Q^2, -Q^2/x, 0, M^2, M^2, M^2) \\
Z_{25} &= C_{11}(0,0,S, M^2, M^2, M^2) \\
Z_{26} &= C_{12}(0,0,-Q^2/x, M^2, M^2, M^2) \\
Z_{27} &= C_{11}(-Q^2, 0, S, M^2, M^2, M^2) \\
Z_{28} &= C_{12}(-Q^2, -Q^2/x, 0, M^2, M^2, M^2) \\
Z_{29} &= C_{12}(d2, 0, 0, S, M^2, M^2, M^2) \\
Z_{30} &= C_0(0,0,-Q^2/x, M^2, M^2, M^2) \\
Z_{31} &= C_0(-Q^2, 0, S, M^2, M^2, M^2) \\
Z_{32} &= C_0(-Q^2, 0, 0, M^2, M^2, M^2) \\
Z_{33} &= C_0(-Q^2, -Q^2/x, 0, M^2, M^2, M^2) \\
Z_{34} &= C_0(0,0,S, M^2, M^2, M^2)
\end{aligned}
$$

D.2 Absence of Structure

As was mentioned in Chapter 4, it was thought that the virtual supersymmetric corrections would exhibit some structure around the squark threshold. In fact the contribution produces a smooth curve. The purpose of this section is to show how individual terms can show structure around the threshold but that the total contribution is in fact smooth.

In order to do this we utilize the contribution $D(Q^2, x, M^2)$ from the previous section. This is made up from a $D_0(Q^2, x, M^2)$ term and 34 other terms all with coefficient terms in Q^2, M^2 and x. In Figures D.1, D.2 and D.3 we have separated out the $D(Q^2, x, M^2)$ contribution to $R_{F_2^\gamma}$ given in Equation (4.9). This is a purely arbitrary choice the important point being the ability to show the functional dependence around the squark threshold. We have taken Bjorken $x = 0.5$ and a squark mass $M = 300\, GeV$.

Figure D.1 shows the contribution due to $D_0(Q^2, x, M^2)$ and its accompanying coefficient terms. There is clearly a positive peak at $\sqrt{Q^2} = 600\, GeV$ which corresponds to the squark threshold given by Equation (4.10). Figure D.2 shows the contribution due to the remaining 34 terms $Z_1 \to Z_{34}$ and their accompanying coefficient terms. There is clearly a negative peak at $\sqrt{Q^2} = 600\, GeV$. These two contributions very neatly cancel each other out to give the smooth curve given in Figure D.3. Thus we have shown that the total contribution due to diagram (f) of Figure 4.2 is in fact smooth with no structure around the squark threshold. The same is true of diagrams (c), (d), and (e) of Figure 4.2 leading to an overall smooth contribution to F_2^γ.

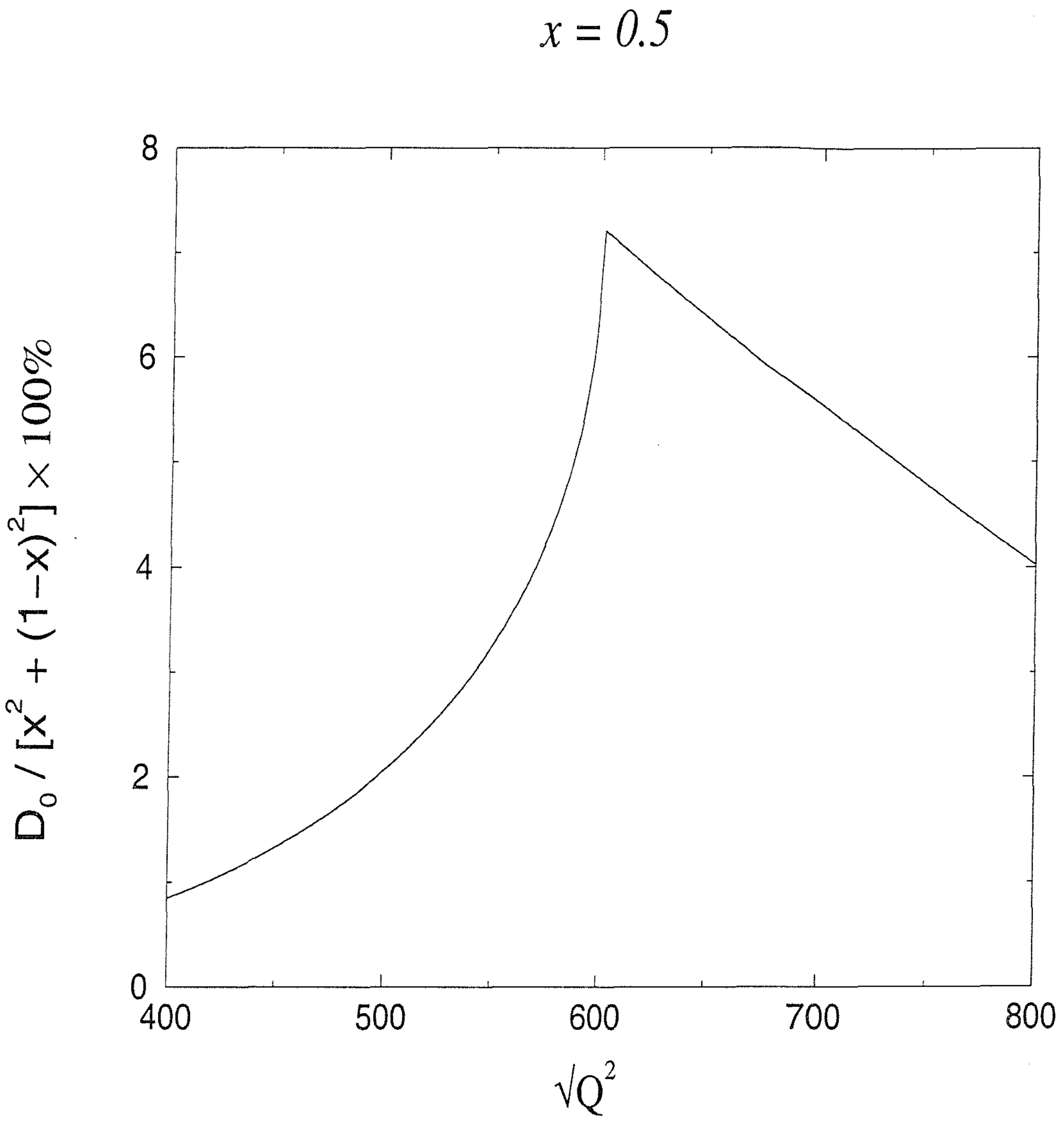

Figure D.1: D_0 contribution to $R_{F_2^\gamma}$ for Bjorken $x = 0.5$ and squark mass $M = 300\,GeV$.

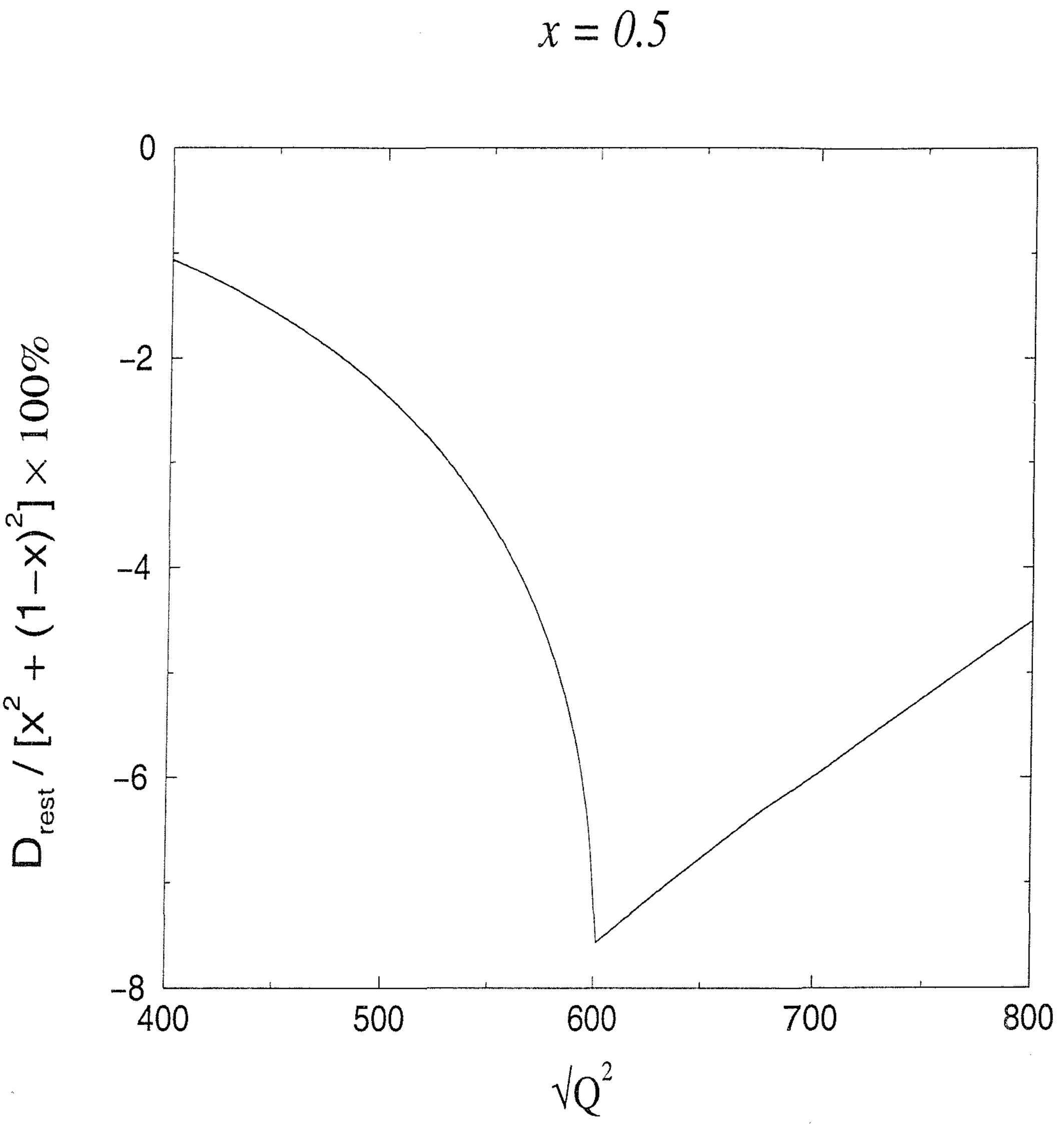

Figure D.2: D_{rest} contribution to $R_{F_2^\gamma}$ for Bjorken $x = 0.5$ and squark mass $M = 300\,GeV$.

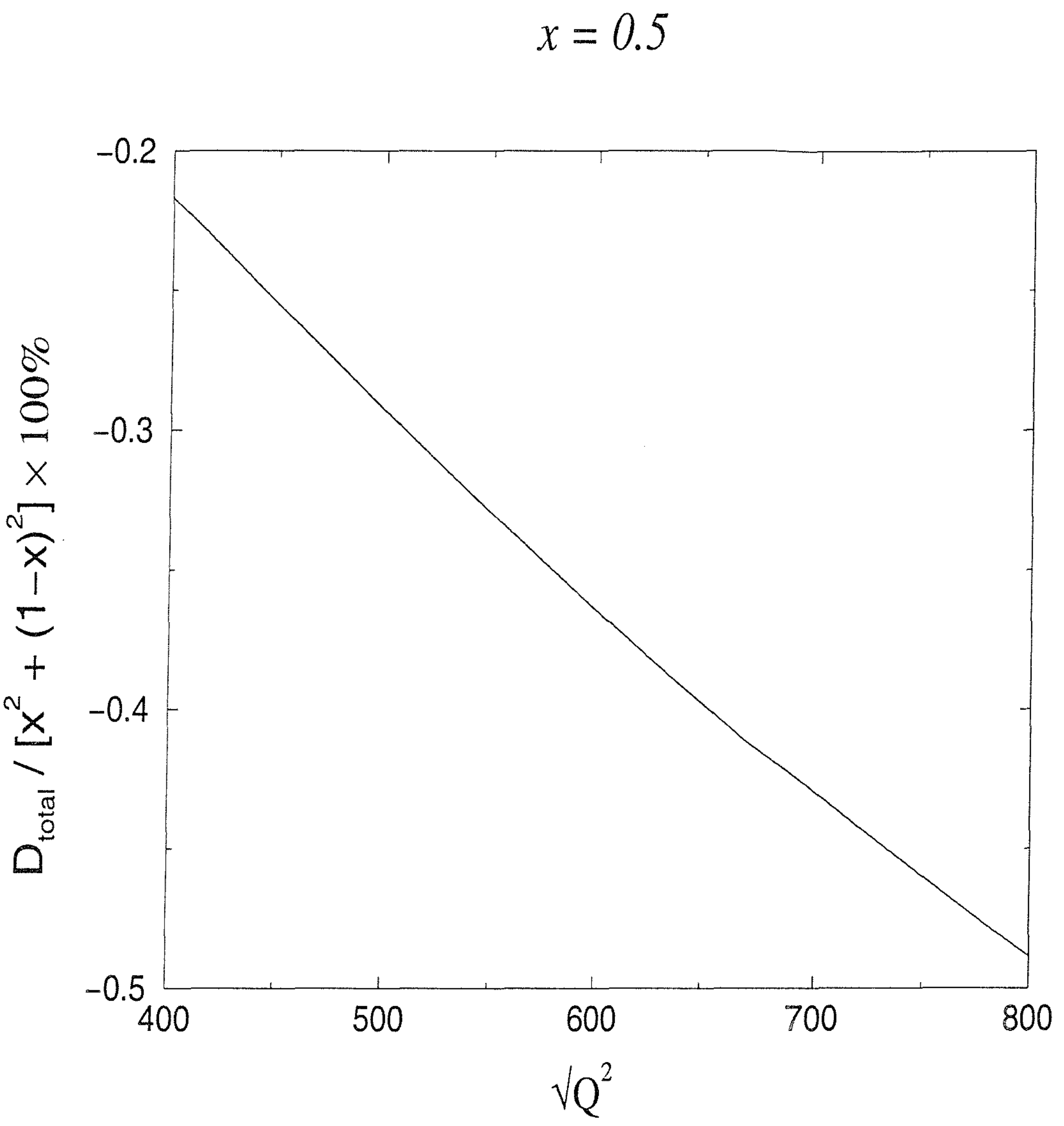

Figure D.3: D_{total} contribution to $R_{F_2^\gamma}$ for Bjorken $x = 0.5$ and squark mass $M = 300\,GeV$.

Appendix E

F_j^i for Chargino Production

In this appendix the four structure functions F_j^i defined by Equation (5.3) are given explicitly. The following variables are used to show them,

$$B = \sqrt{1 - \frac{4m^2 x}{Q^2(1 - x - rx)}}$$

$$a = rx \ , \quad b = 1 - 2rx$$

$$\eta = \frac{B}{b} \sqrt{1 - 4rx^2}$$

$$F = 2a + b(1 + \eta)$$

$$G = 2a + b(1 - \eta)$$

Bjorken x and r are given in Equations (1.5) and (1.7) respectively. The chargino mass is given by m.

$$F_1^1 = \left(\frac{e^4 B}{\pi F G}\right)\left\{ \frac{8x^6r^4}{[1-4rx^2]^2} - \frac{8x^6r^2}{[1-4rx^2]^2} - \frac{16x^5r^3}{[1-4rx^2]^2} - \frac{4x^4r^3}{[1-4rx^2]} \right.$$

$$+ \frac{8x^4r^2}{[1-4rx^2]} + \frac{8x^4r^2}{[1-4rx^2]^2} - \frac{16x^4r}{[1-4rx^2]}\left(\frac{m^2}{Q^2}\right) + \frac{4x^4r}{[1-4rx^2]} + \frac{4x^3r^2}{[1-4rx^2]} - \frac{4x^3r}{[1-4rx^2]}$$

$$\left. + 4x^2r\left(\frac{m^2}{Q^2}\right) - 2x^2r - 8x^2\left(\frac{m^2}{Q^2}\right)^2 + 4x^2\left(\frac{m^2}{Q^2}\right)\right\}$$

$$+ \left(\frac{e^4 B}{\pi}\right)\left\{ -\frac{1}{2} + \frac{4x^4r^3}{[1-4rx^2]^2} + \frac{8x^4r^2}{[1-4rx^2]^2} + \frac{4x^4r}{[1-4rx^2]^2} - \frac{8x^3r^2}{[1-4rx^2]^2} - \frac{8x^3r}{[1-4rx^2]^2} \right.$$

$$\left. + \frac{x^2r^2}{[1-4rx^2]} + \frac{2x^2r}{[1-4rx^2]} + \frac{4x^2r}{[1-4rx^2]^2} - \frac{x^2}{[1-4rx^2]} - \frac{xr}{[1-4rx^2]} + \frac{x}{[1-4rx^2]}\right\}$$

$$+ \left(\frac{e^4 B}{\pi\eta}\right)\ln\left(\frac{F}{G}\right)\left\{\frac{3}{2} + \frac{4x^6r^4}{b[1-4rx^2]^2} + \frac{8x^6r^3}{b[1-4rx^2]^2} + \frac{4x^6r^2}{b[1-4rx^2]^2} - \frac{4x^5r^4}{b[1-4rx^2]^2}\right.$$

$$+\frac{4x^5r^3}{[1-4rx^2]^2}-\frac{12x^5r^2}{b[1-4rx^2]^2}+\frac{4x^5r^2}{[1-4rx^2]^2}+\frac{4x^4r^4}{b[1-4rx^2]}+\frac{8x^4r^3}{b[1-4rx^2]}\left(\frac{m^2}{Q^2}\right)$$

$$+\frac{4x^4r^3}{b[1-4rx^2]}+\frac{4x^4r^3}{b[1-4rx^2]^2}-\frac{2x^4r^3}{[1-4rx^2]^2}-\frac{4x^4r^2}{b[1-4rx^2]}+\frac{2x^4r^2}{b[1-4rx^2]^2}-\frac{2x^4r^2}{[1-4rx^2]^2}$$

$$-\frac{4x^4r}{b[1-4rx^2]}+\frac{2x^4r}{b[1-4rx^2]^2}-\frac{4x^4r}{[1-4rx^2]^2}-\frac{14x^3r^3}{b[1-4rx^2]}+\frac{2x^3r^3}{[1-4rx^2]}$$

$$-\frac{8x^3r^2}{b[1-4rx^2]}\left(\frac{m^2}{Q^2}\right)-\frac{6x^3r^2}{b[1-4rx^2]}+\frac{2x^3r^2}{b[1-4rx^2]^2}+\frac{4x^3r^2}{[1-4rx^2]}\left(\frac{m^2}{Q^2}\right)$$

$$+\frac{2x^3r^2}{[1-4rx^2]}+\frac{2x^3r^2}{[1-4rx^2]^2}-\frac{8x^3r}{b[1-4rx^2]}\left(\frac{m^2}{Q^2}\right)+\frac{4x^3r}{b[1-4rx^2]}+\frac{4x^3r}{[1-4rx^2]}\left(\frac{m^2}{Q^2}\right)$$

$$+\frac{4x^3r}{[1-4rx^2]^2}+\frac{10x^2r^2}{b[1-4rx^2]}-\frac{x^2r^2}{b}-\frac{6x^2r^2}{[1-4rx^2]}+\frac{4x^2r}{b[1-4rx^2]}\left(\frac{m^2}{Q^2}\right)-\frac{2x^2r}{b[1-4rx^2]^2}$$

$$-\frac{2x^2r}{b}\left(\frac{m^2}{Q^2}\right)-\frac{2x^2r}{[1-4rx^2]}\left(\frac{m^2}{Q^2}\right)-\frac{2x^2r}{[1-4rx^2]}-\frac{4x^2}{b}\left(\frac{m^2}{Q^2}\right)^2+\frac{x^2}{b}-\frac{2x^2}{[1-4rx^2]}\left(\frac{m^2}{Q^2}\right)$$

$$-\frac{2xr}{b[1-4rx^2]}+\frac{3xr}{b}+\frac{2xr}{[1-4rx^2]}-xr+\frac{3x}{b}\left(\frac{m^2}{Q^2}\right)-x\left(\frac{m^2}{Q^2}\right)-x-\frac{1}{b}\Bigg\}$$

$$F_1^2 = \left(\frac{e^4B}{\pi FG}\right)\left\{-\frac{48x^7r^5}{[1-4rx^2]^3}+\frac{48x^7r^3}{[1-4rx^2]^3}+\frac{96x^6r^4}{[1-4rx^2]^3}-\frac{8x^5r^4}{[1-4rx^2]^2}\right.$$

$$+\frac{64x^5r^3}{[1-4rx^2]^2}\left(\frac{m^2}{Q^2}\right)-\frac{16x^5r^3}{[1-4rx^2]^2}-\frac{48x^5r^3}{[1-4rx^2]^3}+\frac{32x^5r^2}{[1-4rx^2]^2}\left(\frac{m^2}{Q^2}\right)-\frac{24x^5r^2}{[1-4rx^2]^2}$$

$$+\frac{8x^4r^3}{[1-4rx^2]^2}-\frac{64x^4r^2}{[1-4rx^2]^2}\left(\frac{m^2}{Q^2}\right)+\frac{24x^4r^2}{[1-4rx^2]^2}+\frac{8x^3r^2}{[1-4rx^2]}\left(\frac{m^2}{Q^2}\right)-\frac{4x^3r^2}{[1-4rx^2]}$$

$$\left.-\frac{16x^3r}{[1-4rx^2]}\left(\frac{m^2}{Q^2}\right)^2+\frac{8x^3r}{[1-4rx^2]}\left(\frac{m^2}{Q^2}\right)\right\}$$

$$+\left(\frac{e^4B}{\pi}\right)\left\{-\frac{24x^5r^4}{[1-4rx^2]^3}-\frac{48x^5r^3}{[1-4rx^2]^3}-\frac{24x^5r^2}{[1-4rx^2]^3}+\frac{48x^4r^3}{[1-4rx^2]^3}+\frac{48x^4r^2}{[1-4rx^2]^3}\right.$$

$$-\frac{6x^3r^3}{[1-4rx^2]^2}-\frac{4x^3r^2}{[1-4rx^2]^2}-\frac{24x^3r^2}{[1-4rx^2]^3}-\frac{2x^3r}{[1-4rx^2]^2}$$

$$\left.+\frac{6x^2r^2}{[1-4rx^2]^2}+\frac{2x^2r}{[1-4rx^2]^2}-\frac{xr}{[1-4rx^2]}\right\}$$

$$+\left(\frac{e^4B}{\pi\eta}\right)\ln\left(\frac{F}{G}\right)\left\{-\frac{24x^7r^5}{b[1-4rx^2]^3}-\frac{48x^7r^4}{b[1-4rx^2]^3}-\frac{24x^7r^3}{b[1-4rx^2]^3}+\frac{24x^6r^5}{b[1-4rx^2]^3}\right.$$

$$- \frac{24x^6r^4}{[1-4rx^2]^3} + \frac{72x^6r^3}{b[1-4rx^2]^3} - \frac{24x^6r^3}{[1-4rx^2]^3} - \frac{24x^5r^5}{b[1-4rx^2]^2} - \frac{48x^5r^4}{b[1-4rx^2]^2}\left(\frac{m^2}{Q^2}\right)$$

$$- \frac{40x^5r^4}{b[1-4rx^2]^2} - \frac{24x^5r^4}{b[1-4rx^2]^3} + \frac{12x^5r^4}{[1-4rx^2]^3} - \frac{32x^5r^3}{b[1-4rx^2]^2}\left(\frac{m^2}{Q^2}\right) - \frac{8x^5r^3}{b[1-4rx^2]^2}$$

$$- \frac{12x^5r^3}{b[1-4rx^2]^3} + \frac{12x^5r^3}{[1-4rx^2]^3} - \frac{32x^5r^2}{b[1-4rx^2]^2}\left(\frac{m^2}{Q^2}\right) + \frac{8x^5r^2}{b[1-4rx^2]^2} - \frac{12x^5r^2}{b[1-4rx^2]^3}$$

$$+ \frac{24x^5r^2}{[1-4rx^2]^3} + \frac{84x^4r^4}{b[1-4rx^2]^2} - \frac{12x^4r^4}{[1-4rx^2]^2} + \frac{48x^4r^3}{b[1-4rx^2]^2}\left(\frac{m^2}{Q^2}\right) + \frac{68x^4r^3}{b[1-4rx^2]^2}$$

$$- \frac{12x^4r^3}{b[1-4rx^2]^3} - \frac{24x^4r^3}{[1-4rx^2]^2}\left(\frac{m^2}{Q^2}\right) - \frac{28x^4r^3}{[1-4rx^2]^2} - \frac{12x^4r^3}{[1-4rx^2]^3} + \frac{48x^4r^2}{b[1-4rx^2]^2}\left(\frac{m^2}{Q^2}\right)$$

$$+ \frac{8x^4r^2}{b[1-4rx^2]^2} - \frac{24x^4r^2}{[1-4rx^2]^2}\left(\frac{m^2}{Q^2}\right) - \frac{16x^4r^2}{[1-4rx^2]^2} - \frac{24x^4r^2}{[1-4rx^2]^3} - \frac{2x^3r^3}{b[1-4rx^2]}$$

$$- \frac{60x^3r^3}{b[1-4rx^2]^2} + \frac{36x^3r^3}{[1-4rx^2]^2} - \frac{4x^3r^2}{b[1-4rx^2]}\left(\frac{m^2}{Q^2}\right) - \frac{24x^3r^2}{b[1-4rx^2]^2}\left(\frac{m^2}{Q^2}\right)$$

$$- \frac{32x^3r^2}{b[1-4rx^2]^2} + \frac{12x^3r^2}{b[1-4rx^2]^3} + \frac{12x^3r^2}{[1-4rx^2]^2}\left(\frac{m^2}{Q^2}\right) + \frac{28x^3r^2}{[1-4rx^2]^2} - \frac{8x^3r}{b[1-4rx^2]}\left(\frac{m^2}{Q^2}\right)^2$$

$$+\frac{2x^3r}{b[1-4rx^2]}-\frac{4x^3r}{[1-4rx^2]^2}\left(\frac{m^2}{Q^2}\right)+\frac{6x^2r^2}{b[1-4rx^2]}+\frac{12x^2r^2}{b[1-4rx^2]^2}-\frac{2x^2r^2}{[1-4rx^2]}$$

$$-\frac{12x^2r^2}{[1-4rx^2]^2}+\frac{6x^2r}{b[1-4rx^2]}\left(\frac{m^2}{Q^2}\right)-\frac{2x^2r}{[1-4rx^2]}\left(\frac{m^2}{Q^2}\right)-\frac{2x^2r}{[1-4rx^2]}$$

$$\left.-\frac{2xr}{b[1-4rx^2]}+\frac{3xr}{[1-4rx^2]}\right\}$$

$$F_2^1=\left(\frac{e^4B}{\pi FG}\right)\left\{-\frac{48x^7r^4}{[1-4rx^2]^3}+\frac{48x^7r^2}{[1-4rx^2]^3}+\frac{96x^6r^3}{[1-4rx^2]^3}-\frac{24x^5r^3}{[1-4rx^2]^2}\right.$$

$$+\frac{64x^5r^2}{[1-4rx^2]^2}\left(\frac{m^2}{Q^2}\right)+\frac{16x^5r^2}{[1-4rx^2]^2}-\frac{48x^5r^2}{[1-4rx^2]^3}-\frac{32x^5r}{[1-4rx^2]^2}\left(\frac{m^2}{Q^2}\right)$$

$$-\frac{8x^5r}{[1-4rx^2]^2}+\frac{24x^4r^2}{[1-4rx^2]^2}-\frac{64x^4r}{[1-4rx^2]^2}\left(\frac{m^2}{Q^2}\right)+\frac{8x^4r}{[1-4rx^2]^2}+\frac{8x^3r}{[1-4rx^2]}\left(\frac{m^2}{Q^2}\right)$$

$$\left.-\frac{4x^3r}{[1-4rx^2]}-\frac{16x^3}{[1-4rx^2]}\left(\frac{m^2}{Q^2}\right)^2+\frac{8x^3}{[1-4rx^2]}\left(\frac{m^2}{Q^2}\right)\right\}$$

$$+\left(\frac{e^4B}{\pi}\right)\left\{-\frac{24x^5r^3}{[1-4rx^2]^3}-\frac{48x^5r^2}{[1-4rx^2]^3}-\frac{24x^5r}{[1-4rx^2]^3}+\frac{48x^4r^2}{[1-4rx^2]^3}+\frac{48x^4r}{[1-4rx^2]^3}\right.$$

$$- \frac{2x^3r^2}{[1-4rx^2]^2} + \frac{4x^3r}{[1-4rx^2]^2} - \frac{24x^3r}{[1-4rx^2]^3} - \frac{6x^3}{[1-4rx^2]^2} + \frac{2x^2r}{[1-4rx^2]^2}$$

$$+ \frac{6x^2}{[1-4rx^2]^2} - \frac{x}{[1-4rx^2]} \Bigg\}$$

$$+ \left(\frac{e^4B}{\pi\eta}\right) \ln\left(\frac{F}{G}\right) \Bigg\{ - \frac{24x^7r^4}{b[1-4rx^2]^3} - \frac{48x^7r^3}{b[1-4rx^2]^3} - \frac{24x^7r^2}{b[1-4rx^2]^3} + \frac{24x^6r^4}{b[1-4rx^2]^3}$$

$$- \frac{24x^6r^3}{[1-4rx^2]^3} + \frac{72x^6r^2}{b[1-4rx^2]^3} - \frac{24x^6r^2}{[1-4rx^2]^3} - \frac{8x^5r^4}{b[1-4rx^2]^2} - \frac{16x^5r^3}{b[1-4rx^2]^2} \left(\frac{m^2}{Q^2}\right)$$

$$- \frac{24x^5r^3}{b[1-4rx^2]^2} - \frac{24x^5r^3}{b[1-4rx^2]^3} + \frac{12x^5r^3}{[1-4rx^2]^3} - \frac{32x^5r^2}{b[1-4rx^2]^2} \left(\frac{m^2}{Q^2}\right) - \frac{24x^5r^2}{b[1-4rx^2]^2}$$

$$- \frac{12x^5r^2}{b[1-4rx^2]^3} + \frac{12x^5r^2}{[1-4rx^2]^3} - \frac{32x^5r}{b[1-4rx^2]^2} \left(\frac{m^2}{Q^2}\right) - \frac{8x^5r}{b[1-4rx^2]^2} - \frac{12x^5r}{b[1-4rx^2]^3}$$

$$+ \frac{24x^5r}{[1-4rx^2]^3} + \frac{28x^4r^3}{b[1-4rx^2]^2} - \frac{4x^4r^3}{[1-4rx^2]^2} + \frac{16x^4r^2}{b[1-4rx^2]^2} \left(\frac{m^2}{Q^2}\right) + \frac{44x^4r^2}{b[1-4rx^2]^2}$$

$$- \frac{12x^4r^2}{b[1-4rx^2]^3} - \frac{8x^4r^2}{[1-4rx^2]^2} \left(\frac{m^2}{Q^2}\right) - \frac{20x^4r^2}{[1-4rx^2]^2} - \frac{12x^4r^2}{[1-4rx^2]^3} + \frac{16x^4r}{b[1-4rx^2]^2} \left(\frac{m^2}{Q^2}\right)$$

$$+\frac{24x^4r}{b[1-4rx^2]^2}-\frac{8x^4r}{[1-4rx^2]^2}\left(\frac{m^2}{Q^2}\right)-\frac{16x^4r}{[1-4rx^2]^2}-\frac{24x^4r}{[1-4rx^2]^3}-\frac{2x^3r^2}{b[1-4rx^2]}$$

$$-\frac{20x^3r^2}{b[1-4rx^2]^2}+\frac{12x^3r^2}{[1-4rx^2]^2}-\frac{4x^3r}{b[1-4rx^2]}\left(\frac{m^2}{Q^2}\right)-\frac{8x^3r}{b[1-4rx^2]^2}\left(\frac{m^2}{Q^2}\right)-\frac{32x^3r}{b[1-4rx^2]^2}$$

$$+\frac{12x^3r}{b[1-4rx^2]^3}+\frac{4x^3r}{[1-4rx^2]^2}\left(\frac{m^2}{Q^2}\right)+\frac{20x^3r}{[1-4rx^2]^2}-\frac{8x^3}{b[1-4rx^2]}\left(\frac{m^2}{Q^2}\right)^2+\frac{2x^3}{b[1-4rx^2]}$$

$$-\frac{12x^3}{[1-4rx^2]^2}\left(\frac{m^2}{Q^2}\right)+\frac{6x^2r}{b[1-4rx^2]}+\frac{4x^2r}{b[1-4rx^2]^2}-\frac{2x^2r}{[1-4rx^2]}-\frac{4x^2r}{[1-4rx^2]^2}$$

$$+\frac{6x^2}{b[1-4rx^2]}\left(\frac{m^2}{Q^2}\right)-\frac{2x^2}{[1-4rx^2]}\left(\frac{m^2}{Q^2}\right)-\frac{2x^2}{[1-4rx^2]}-\frac{2x}{b[1-4rx^2]}+\frac{3x}{[1-4rx^2]}\Bigg\}$$

$$F_2^2 = \left(\frac{e^4B}{\pi FG}\right)\Bigg\{-\frac{288x^8r^5}{[1-4rx^2]^4}+\frac{288x^8r^3}{[1-4rx^2]^4}+\frac{576x^7r^4}{[1-4rx^2]^4}-\frac{48x^6r^4}{[1-4rx^2]^3}$$

$$+\frac{192x^6r^3}{[1-4rx^2]^3}\left(\frac{m^2}{Q^2}\right)-\frac{288x^6r^3}{[1-4rx^2]^4}-\frac{48x^6r^2}{[1-4rx^2]^3}+\frac{48x^5r^3}{[1-4rx^2]^3}$$

$$-\frac{192x^5r^2}{[1-4rx^2]^3}\left(\frac{m^2}{Q^2}\right)+\frac{48x^5r^2}{[1-4rx^2]^3}+\frac{16x^4r^2}{[1-4rx^2]^2}\left(\frac{m^2}{Q^2}\right)-\frac{8x^4r^2}{[1-4rx^2]^2}$$

$$- \frac{32x^4r}{[1-4rx^2]^2}\left(\frac{m^2}{Q^2}\right)^2 + \frac{16x^4r}{[1-4rx^2]^2}\left(\frac{m^2}{Q^2}\right)\Bigg\}$$

$$+ \left(\frac{e^4B}{\pi}\right)\Bigg\{ -\frac{144x^6r^4}{[1-4rx^2]^4} - \frac{288x^6r^3}{[1-4rx^2]^4} - \frac{144x^6r^2}{[1-4rx^2]^4} + \frac{288x^5r^3}{[1-4rx^2]^4} + \frac{288x^5r^2}{[1-4rx^2]^4}$$

$$- \frac{12x^4r^3}{[1-4rx^2]^3} - \frac{144x^4r^2}{[1-4rx^2]^4} - \frac{12x^4r}{[1-4rx^2]^3} + \frac{12x^3r^2}{[1-4rx^2]^3} + \frac{12x^3r}{[1-4rx^2]^3} - \frac{2x^2r}{[1-4rx^2]^2}\Bigg\}$$

$$+ \left(\frac{e^4B}{\pi\eta}\right)\ln\left(\frac{F}{G}\right)\Bigg\{ - \frac{144x^8r^5}{b[1-4rx^2]^4} - \frac{288x^8r^4}{b[1-4rx^2]^4} - \frac{144x^8r^3}{b[1-4rx^2]^4} + \frac{144x^7r^5}{b[1-4rx^2]^4}$$

$$- \frac{144x^7r^4}{[1-4rx^2]^4} + \frac{432x^7r^3}{b[1-4rx^2]^4} - \frac{144x^7r^3}{[1-4rx^2]^4} - \frac{48x^6r^5}{b[1-4rx^2]^3} - \frac{96x^6r^4}{b[1-4rx^2]^3}\left(\frac{m^2}{Q^2}\right)$$

$$- \frac{96x^6r^4}{b[1-4rx^2]^3} - \frac{144x^6r^4}{b[1-4rx^2]^4} + \frac{72x^6r^4}{[1-4rx^2]^4} - \frac{96x^6r^3}{b[1-4rx^2]^3}\left(\frac{m^2}{Q^2}\right) - \frac{48x^6r^3}{b[1-4rx^2]^3}$$

$$- \frac{72x^6r^3}{b[1-4rx^2]^4} + \frac{72x^6r^3}{[1-4rx^2]^4} - \frac{96x^6r^2}{b[1-4rx^2]^3}\left(\frac{m^2}{Q^2}\right) - \frac{72x^6r^2}{b[1-4rx^2]^4} + \frac{144x^6r^2}{[1-4rx^2]^4}$$

$$+ \frac{168x^5r^4}{b[1-4rx^2]^3} - \frac{24x^5r^4}{[1-4rx^2]^3} + \frac{96x^5r^3}{b[1-4rx^2]^3}\left(\frac{m^2}{Q^2}\right) + \frac{168x^5r^3}{b[1-4rx^2]^3} - \frac{72x^5r^3}{b[1-4rx^2]^4}$$

$$
-\frac{48x^5r^3}{[1-4rx^2]^3}\left(\frac{m^2}{Q^2}\right)-\frac{72x^5r^3}{[1-4rx^2]^3}-\frac{72x^5r^3}{[1-4rx^2]^4}+\frac{96x^5r^2}{b[1-4rx^2]^3}\left(\frac{m^2}{Q^2}\right)+\frac{48x^5r^2}{b[1-4rx^2]^3}
$$

$$
-\frac{48x^5r^2}{[1-4rx^2]^3}\left(\frac{m^2}{Q^2}\right)-\frac{48x^5r^2}{[1-4rx^2]^3}-\frac{144x^5r^2}{[1-4rx^2]^4}-\frac{4x^4r^3}{b[1-4rx^2]^2}-\frac{120x^4r^3}{b[1-4rx^2]^3}
$$

$$
+\frac{72x^4r^3}{[1-4rx^2]^3}-\frac{8x^4r^2}{b[1-4rx^2]^2}\left(\frac{m^2}{Q^2}\right)-\frac{48x^4r^2}{b[1-4rx^2]^3}\left(\frac{m^2}{Q^2}\right)-\frac{96x^4r^2}{b[1-4rx^2]^3}+\frac{72x^4r^2}{b[1-4rx^2]^4}
$$

$$
+\frac{24x^4r^2}{[1-4rx^2]^3}\left(\frac{m^2}{Q^2}\right)+\frac{72x^4r^2}{[1-4rx^2]^3}-\frac{16x^4r}{b[1-4rx^2]^2}\left(\frac{m^2}{Q^2}\right)^2+\frac{4x^4r}{b[1-4rx^2]^2}
$$

$$
-\frac{24x^4r}{[1-4rx^2]^3}\left(\frac{m^2}{Q^2}\right)+\frac{12yx^3r^2}{b[1-4rx^2]^2}+\frac{24x^3r^2}{b[1-4rx^2]^3}-\frac{4x^3r^2}{[1-4rx^2]^2}-\frac{24x^3r^2}{[1-4rx^2]^3}
$$

$$
+\frac{12x^3r}{b[1-4rx^2]^2}\left(\frac{m^2}{Q^2}\right)-\frac{4x^3r}{[1-4rx^2]^2}\left(\frac{m^2}{Q^2}\right)-\frac{4x^3r}{[1-4rx^2]^2}-\frac{4x^2r}{b[1-4rx^2]^2}+\frac{6x^2r}{[1-4rx^2]^2}\Bigg\}
$$

Bibliography

[1] V. Budnev, I. Ginzburg, G. Meledin and V. Serbo, *Phys. Rep.* **15**, 181 (1975)

[2] C. Berger and W. Wagner, *Phys. Rep.* **146**, 1 (1987)

[3] R. Bhattacharya, G. Grammar Jr., and J. Smith, *Phys. Rev.* **D15**, 3267 (1977)

[4] R. Nisius, *Phys. Rept.* **332**, 165 (2000)

[5] S. Maxfield, *Ph.D Thesis* **MdDP-PP-85-147** (1984)

[6] H. Abramowicz, K. Charchula, M. Krawczyk, A. Levy and U. Maor, *Int. J. Mod. Phys.* **A8**, 1005 (1993)

[7] R. Godbole, *hep-ph* **9602428** (1996)

[8] M. Krawczyk, *Acta. Phys. Polon.* **B28**, 2659 (1997)

[9] S. Brodsky, F. Close and J. Gunion, *Phys. Rev.* **D6**, 177 (1972)
J. Da Luz Vieira and J. Storrow, *Phys. Lett* **B205**, 367 (1988)

[10] E. Witten, *Nucl. Phys.* **B120**, 189 (1977)

[11] D. Gross and F. Wilczek, *Phys. Rev.* **D8**, 3633 (1974)
D. Gross and F. Wilczek, *Phys. Rev.* **D9**, 980 (1974)

[12] M. Glück and E. Reya, *Phys. Rev.* **D28**, 2749 (1983)

[13] M. Glück, E. Reya and A. Vogt, *Phys. Rev.* **D45**, 3986 (1991)

[14] M. Glück, E. Reya and M. Stratmann, *Phys. Rev.* **D54**, 5515 (1996)

[15] R. Ellis, W. Stirling and B. Webber,
QCD and Collider Physics. pg 109-113
Cambridge University Press, 1996

[16] C. Kounnas and D. Ross, *Nucl. Phys.* **B214**, 317 (1983)

[17] J. Wess and J. Bagger, *Supersymmetry and Supergravity.*
Princeton University Press, 1991
J. Gunion, *A Simplified Summary of Supersymmetry.*
ITP Conference on Future High Energy Colliders, Santa Barbara (1996)
H. Haber, *The Supersymmetric Top-Ten Lists.*
Woodlands Superworld 1993:0027-51 (QCD161:I966:1993)
M. Drees, *An Introduction to Supersymmetry.*
hep-ph/9611409 (1996)
H. Haber and G. Kane, *Phys. Rept.* **117**, 75 (1985)

[18] S. Jones and C. Llewellyn-Smith, *Nucl. Phys* **B217**, 145 (1983)

[19] E. Reya, *Phys. Lett.* **B124**, 424 (1983)

[20] R. Demina et al., **hep-ph/0005112** (2000)

[21] M. Buza et al., *Nucl. Phys.* **B472**, 611 (1996)
M. Buza, V. Matiouine, J. Smith and W. van Neervan,
Eur. Phys. **C1**, 301 (1998)
R. Thorne and R. Roberts, *Phys. Rev.* **D57**, 6781 (1998)
R. Thorne and R. Roberts, *Phys. Lett.* **B421**, 303 (1998)
A. Martin, R. Roberts, W. Stirling and R. Thorne,
Eur. Phys. J. **C4**, 463 (1998)

[22] J. Ellis and D. Ross, *Eur. Phys. J.* **C4** 339, (1998)

[23] G. Passarino and M. Veltman, *Nucl. Phys.* **B160**, 151 (1979)

[24] H. Haber, **(University of California, Santa Cruz)**
Fortran Source Code, *haber@scipp.ucsc.edu*

[25] D. Ross and L. Weston, *Eur. Phys. J.* **C18** 593, (2001)

[26] D. Groom et al. (Particle Data Group), *Eur. Phys. J.* **C15** 1, (2000)